A Study of Short-Spacing Correction for Galactic and Extragalactic Objects

Dissertation

zur

Erlangung des Doktorgrades (Dr. rer. nat.)

der

Mathematisch-Naturwissenschaftlichen Fakultät

der

Rheinischen Friedrich-Wilhelms-Universität Bonn

von

Shahram Faridani

aus

Teheran

Bonn, September 2014

Contents

Abstract

Radio telescopes can be divided into single-dish instruments and interferometer arrays. Their respective observational approaches are fundamentally different. Single dishes can make an accurate measurement of flux. However, due to practical limits in the size of the dish which can be constructed, they have correspondingly limited resolution. On the other hand, interferometric arrays can be as large as the earth, with corresponding resolution, yet cannot accurately measure the total flux, or resolve extended objects. This is because they are not able to measure zero- and short-spacings.

The technique of short-spacing correction (SSC) bridges the gap between the single-dish and array approaches. It combines the high angular resolution from interferometric observations with the total flux measurement from single-dish observations. Hence, the final data product combines the best of both worlds. The correction is of great importance for the Galactic objects as well as a number of nearby galaxies with considerable amount of diffuse and extended structure.

For neutral atomic hydrogen (H I) observations, each of these instruments provides different information regarding different gas phases present in the interstellar medium (ISM). The single-dish instrument provides information regarding the large angular scale structures, whereas the interferometric array provides information about the small angular scale structures. Only after combining the two data sets is it possible to study all gas phases in detail.

In the near future, several large interferometer instruments will become available. The new instruments provide large amounts of data (for instance, in the case of the Australia's Square Kilometer Array Pathfinder (ASKAP, Duffy et al. 2012), the expected data rate is about 2.8 GB/s). Considering the large amount of data, it is very difficult to store the raw data indefinitely. SSC will continue to be a desirable technique, and any viable SSC algorithm needs to be designed to cope with the anticipated features and problems of the new instruments. An important requirement for a future-oriented SSC algorithm is therefore that it operates on science-ready images, not requiring any raw data input.

The present dissertation presents an automated pipeline which is able to perform the SSC in the image domain. The algorithm takes the peculiarities of future instruments into account, namely, large amounts of data and restricted access to raw data. It operates on cleaned and calibrated interferometric data in combination with single-dish observations. The impacts on the algorithm of weighting schemes and pixel size in combination with different deconvolution procedures have also been studied. The latter parameters were found to affect the result of the combination significantly.

The pipeline has been evaluated with both Galactic and extragalactic spectral line data sets obtained from different instruments. In all the cases, the combination fulfills the expectations, i.e., the measured total flux in the combined data set is in good agreement with the measured value in the single-dish data, while the interferometric resolution is preserved in the combination. The study underlines the importance of SSC for a detailed study of different gas phases.

Kurzfassung

Radioteleskope werden in Einzelteleskope und Interferometer aufgeteilt. Der Aufbau dieser Instrumente sowie deren Beobachtungstechnik ist sehr unterschiedlich. Einzelteleskope erreichen im Vergleich zu Interferometern eine geringere Auflösung. Dafür ist das Bild eines Interferometers ein unvollständiges Modell der wahren Helligkeitsverteilung des beobachteten Objekts. Der Grad der Unvollständigkeit des Modells hängt unmittelbar von dem Objekt selbst sowie von dessen Entfernung ab.

Die Unvollständigkeit ist signifikant für galaktische sowie naheliegende Objekte, die über beachtliche Mengen diffusen Gases (groß-skalige Strukturen) verfügen. Für diese Objekte ist die gemessene Gesamtintensität von einem Interferometer geringer als mit einem Einzelteleskop. Durch die Kombination der Daten eines Interferometers und eines Einzelteleskops kann dies kompensiert werden, man spricht von der *short-spacing correction (SSC)*. Die SSC erzielt ein besseres Gesamtergebnis aus den beiden Methoden, indem die Auflösung eines Interferometers und die Gesamtintensität eines Einzelteleskops kombiniert werden.

Die Zukunft der Radioastronomie wird sehr stark von modernen Interferometern geprägt. Aus dem Grund wird auch die SSC ein erstrebenswerter Ansatz sein. Die größte Herausforderung der zukünftigen Instrumente wird jedoch die Bewältigung der enormen Datenmengen sein. Auf Grund der großen Datenmenge wird die Speicherung der Rohdaten nahezu unmöglich. Deshalb besteht ein wichtiger Schritt darin, die gewonnenen Erfahrungen und Fachkenntnisse der aktuellen Systeme unter Berücksichtigung ihrer Beschränkungen auf die zukünftigen Systeme zu übertragen.

Im Rahmen der vorliegenden Dissertation wurde eine automatisierte Pipeline entwickelt, die in der Lage ist, die Kombination für die reduzierten Daten durchzuführen. Die Studie betont vor allem die Wichtigkeit der SSC für eine detaillierte Analyse verschiedener Gas-Phasen im interstellaren Medium (ISM). Des Weiteren wurde eine systematische Studie der Kombinationsmethode mit Hilfe von Beobachtungen von galaktischen und extragalaktischen Objekten genutzt durchgeführt. Die Ergebnisse zeigen, dass die vorgestellte Methode die Erwartungen erfüllt. Die Methode hat damit aufgrund ihres Aufbaus das Potential, im Rahmen der SSC mit zukünftigen Interferometern als erfolgsversprechender Ansatz verwendet zu werden.

Introduction

> The third group [of radio static] is composed of a very steady hiss type static the origin of which is not yet known...[however] the direction of arrival changes gradually throughout the day going almost completely around the compass in 24 hours.
>
> *(Karl Jansky, 1932)*

Hydrogen is the most abundant element in the universe. Thus, neutral atomic hydrogen (H I) observations play a major role in understanding of the evolution of various cosmic objects as well as their dynamics. The presence of H I is an essential factor for an ongoing star formation, whereas its absence suggests an aging population. Ewen & Purcell (1951) detected emission of the H I transition originating from the Milky Way in the early 50s. Within a short time, Kerr & Hindman (1953) detected H I emission from the Magellanic clouds. These observations confirmed the prediction by Van de Hulst (van Woerden & Strom 2006) regarding the possible observation of the 21 cm line hyperfine transition. Ever since, a huge number of both Galactic and extragalactic objects have been observed with the 21 cm line. The ease of detection (simple hardware for observation at 1.4 GHz, and optically thin targets in huge numbers, which are distributed all over the sky) as well as the relative reliability of physical parameters derived from 21 cm line observations make it a powerful tool in radio astronomy (Giovanelli & Haynes 1988). Originally, the majority of H I observations were conducted with large single-dish instruments. In the seventies, the technique of aperture synthesis became a standard approach for H I spectral observations. With aperture synthesis, much higher angular resolutions were achievable. However, the single-dish instruments still played a significant role in H I astronomy, especially for wide-field survey projects (Giovanelli & Haynes 1988).

In the last decade, a number of new and modern Galactic and extragalactic H I surveys have been conducted. These surveys opened many new windows for studying different scientific aspects of galaxy dynamics and evolution using the interstellar medium (ISM). The H I Parkes All-Sky Survey (HIPASS, Barnes et al. 2001) was the first large-area survey of the extragalactic H I. With the Galactic All-Sky Survey (GASS, McClure-Griffiths et al. 2009; Kalberla et al. 2010) and the Effelsberg-Bonn H I Survey (EBHIS, Kerp et al. 2011), two modern surveys became available for both Galactic and, in the

case of EBHIS, also extragalactic objects. The aforementioned surveys also serve as finders, where interferometric follow-up observations provide additional information. In recent years, targeted deep interferometric surveys such as The H i Nearby Galaxy Survey (THINGS, Walter et al. 2008) and the Hydrogen Accretion in LOcal GAlaxieS (HALOGAS, Heald et al. 2011) have been conducted.

The existing large-area surveys have been performed using single-dish instruments. In the future, modern interferometers will be the dominant instruments in radio astronomy. New instruments, e.g., APERTIF (Oosterloo et al. 2009) will be able to conduct surveys with much higher angular resolutions than is achievable with a single dish. The upcoming H i 21 cm line surveys conducted with Australia's Square Kilometer Array Pathfinder (ASKAP, Duffy et al. 2012) and the South African MeerKAT radio telescope (de Blok et al. 2009) will cover the entire sky out to redshift of order 1. With these sky coverages, it will not only be possible to explore the gas distribution of the Milky Way and its surrounding structures at arc second resolution (Dickey et al. 2013), but also to investigate the H i content and dynamics of the galaxies in the local volume (Oosterloo et al. 2010; Duffy et al. 2012).

In the new era of interferometers, single-dish instruments will still play a major role. This is due to the different observational approaches of single dish and interferometers. A single dish measures the intensity distribution of an object, whereas an interferometer is not able to measure the intensity in the first instance, instead it measures the correlation of different baselines in an array. Each baseline component corresponds to the geometrical separation of two adjacent antennas in the array, where the highest resolution for an interferometer is set by the maximum separation of an antenna pair. At any time instant the cross corellation between the two antennas of a baseline (known as a visibility) corresponds to a point sample of the Fourier transform of the image.

The transform plane ((u, v) plane) cannot be infinitely sampled. In particular the central region of it is never sampled as a result of physical size of two antennas. The incompleteness of the central region results in insensitivity of the synthesized array towards extended structures. This phenomenon is known as the missing-spacing problem (MSP). Short-spacing correction (SSC), the topic of this thesis, is the solution to the MSP, where the single-dish instrument performs a complementary role and provides the missing spacings to the interferometric observation. For future Galactic and nearby galaxy surveys, e.g., the Galactic Australian Square Kilometer Array Pathfinder (GASKAP, Dickey et al. 2013), performed with ASKAP, missing spacings will be still an issue. Therefore, the SSC can make an important contribution in obtaining an exact image of all the components present in the ISM for the latter surveys.

For the future instruments, one of the important tasks is transferring the knowledge from the existing instruments to the future ones considering their features and anticipated problems. In particular, data handling for the new algorithms requires careful consideration, since the new instruments measure a very large amount of raw data (Alexander et al. 2009). Hence, long-term storage of raw data will not be possible ad infinitum. Any new algorithm needs to consider this fact.

The number of existing publications in the literature does not reflect the importance of SSC. In the majority of cases, the combined data are the result of a third-party software, where the constitution of the approach is not fully transparent. This makes the analysis of the properties of the data very difficult.

The present work demonstrates the necessity of SSC for a detailed understanding of the ISM for Galactic and nearby extragalactic objects. The goal is to develop an algorithm that operates on the science-ready data of single-dish and cleaned interferometric data without any additional information such as the beam, the dirty image, and the visibilities. A linear approach is introduced for merging the science-ready interferometric and single-dish data in the image domain. A fully automated pipeline has been implemented. It is attempted to show qualitative differences between various interferometric images and how they affect the result of the combination. The present study addresses two major questions. First, is it feasible to perform the combination for any data set? Second, how significant are the impacts of different imaging parameters on both interferometric and combined data sets?

The combination pipeline is evaluated for both Galactic and extragalactic objects. For the Galactic part, the results of the combination for the Small Magellanic Cloud (SMC) and three compact high-velocity clouds (CHVCs) in the halo of Milky Way have been analyzed. The single-dish, interferometric, and combined data sets of these objects have been used to study the morphological and physical properties of the objects. For the extragalactic part, a sample of three nearby galaxies has been studied. The three galaxies differ in their morphologies and physical properties. The study demonstrates the result of SSC in the case of nearby galaxies using different THINGS observations. For these galaxies, the impacts of the interferometric imaging parameters; weighting scheme and pixel size on the resulting image are investigated. Additionally, the study demonstrates the SSC for galaxies at different distances and with different H I contents.

In the following, the outlines of this thesis are presented.

Outline of this dissertation

- Chapter 2 is devoted to technical aspects of H I astronomy. In particular, two common imaging techniques for both single-dish and interferometric instruments are discussed. A detailed understanding of each approach is essential for the combination. Chapter 2 highlights the most important aspects of each approach, since the nature of the approaches as well as the final results of the imaging are very different. A number of H I surveys is also introduced. For the research presented here, a large number of data sets from different objects with various physical and morphological properties is required.

- Chapter 3 deals with the concept of the SSC. A number of existing approaches are discussed. A brief overview of the advantages and disadvantages of each method are provided. As reported in the present thesis, a new combination pipeline has been developed which introduces a new algorithm. This algorithm has been developed considering the possible limitations that radio astronomers are going to face in regard to the large amount of data coming from the new generation of radio astronomy instruments which will go online in the near future. For the purpose of evaluation, the result of combination for both Galactic and extra-galactic data have been studied. A comparison between the results of the combination using the introduced algorithm in this work and the result of the combination from previous approaches using the SMC data rounds up the chapter.

- Chapter 4 introduces a sample of three nearby galaxies. The focus is mainly on the effect of two imaging parameters. The two parameters, in combination with a different deconvolution approach, could have strong impacts on the final result of the imaging for the interferometric data, which affects the result of combination significantly. A special case is also described in this chapter, in which the galaxy is embedded in strong Milky Way emission. The strong Galactic emission affects the result of the combination both in regard to measured flux density as well as kinematical properties.

- Chapter 5[1] presents a study of the combination for three CHVCs in the halo of the Milky Way. An overview of the physical and morphological properties of the three HVCs is first provided. The results of the SSC for these clouds are presented. The combined data sets are used to study further morphological and physical properties of these clouds.

---

[1] Based on a publication by Astronomy & Astrophysics (A& A) journal entitled: H I observations of three compact high-velocity clouds around the Milky Way.

- Chapter 6 presents the conclusions. An overview of future work is given. Finally, a number of projects and ideas are listed, which are directly related to the current study.

The modern H I sky

Astronomers receive the majority of information from celestial objects via electromagnetic radiation. The origin of this signal amongst others is in atomic or molecular transitions or in continuous radiation processes resulting from accelerated charges. The radiation emitted from astronomical objects is categorized according to their frequencies (wavelengths).

Radio astronomy, compared to the optical astronomy, is a rather young discipline. It was in 1931 when Karl Guthe Jansky detected the emitted radiation at a wavelength of 14.6 m from an extraterrestrial source. However, it took more than a decade for radio astronomy to take a step forward. Ever since, new instruments and techniques have revolutionized radio astronomy and have opened new windows to the universe.

Since its detection by Ewen & Purcell (1951) and Muller & Oort (1951), the 21-cm line of neutral atomic hydrogen (H I) with the corresponding frequency of 1.42 GHz has been one of the most important spectral lines in the radio regime. It is a powerful instrument for studying the interstellar gas.

The 21-cm line is a highly forbidden transition; its transition rate is very small ($\approx 3 \times 10^{-15}\,\mathrm{s}^{-1}$) resulting in a long lifetime of $\approx 10^7$ a. Nevertheless, it is detectable since hydrogen is the most abundant element in the universe (Draine 2011). Detection of H I is important for studying various properties of gas such as temperature, velocity distribution, and kinematics for both Galactic and extragalactic objects.

The current chapter describes the tools and techniques used in radio astronomy. It provides an overview of the two commonly used observing techniques: single dish and interferometry. The two approaches are significantly different, particularly in the way each method produces the final image. Furthermore, the spatial frequency response of each instrument is different (Emerson 2002). Both single-dish and interferometer instruments are complementary.

2.1 Imaging in radio astronomy

Radio telescopes are divided into two categories: single-dish telescopes and interferometer arrays. The physical principles regarding both instruments are completely different. Therefore, the imaging techniques differ significantly. In the following, two of the most important properties of radio telescopes, i.e., angular resolution and antenna pattern are defined. Furthermore, the common imaging techniques for both observations are explained.

The highest angular resolution a radio telescope can achieve is limited by diffraction and is given by

the Rayleigh criterion:

$$\theta = 1.22 \frac{\lambda}{D}, \tag{2.1}$$

where λ is the wavelength and D the diameter of the telescope. θ is the angular resolution in radians. In order to improve the angular resolution at a given wavelength, one needs to increase the size of the telescope, which of course faces physical and financial limitations. The need to achieve higher angular resolution has led to the technique of aperture synthesis (Thompson 1999). Aperture synthesis is directly inspired by the Michelson interferometer for visible light. The aim of synthesis imaging is to combine signals from a larger number of telescopes to produce images that have the same angular resolution as the ones by instruments of the size of an entire array.
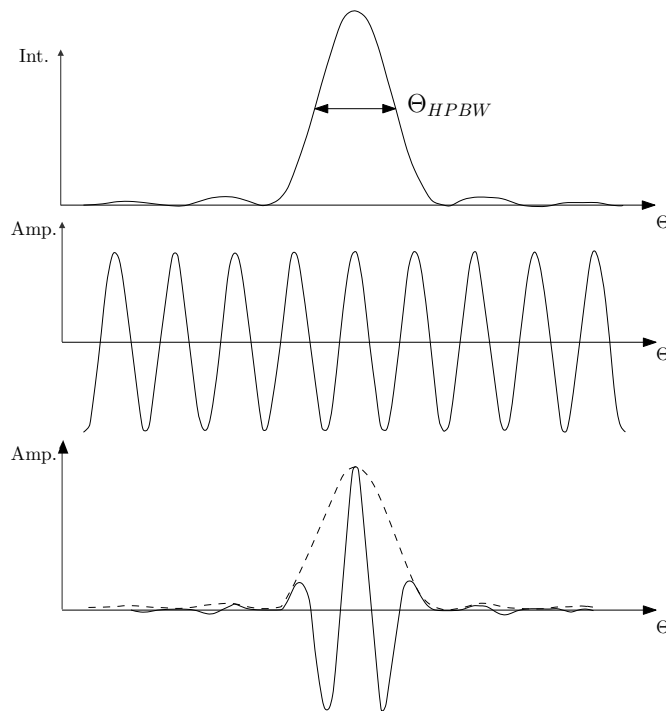
Figure 2.1: *The top panel*: the antenna pattern of a single-dish telescope. With a main lobe and decreasing side lobes. *The middle panel:* the antenna pattern of a two-element interferometer without any main lobe nor decreasing side lobes. *The bottom panel:* the antenna pattern of an interferometer considering the pattern of a single-dish telescope. As a result of this the side lobes are suppressed.

A further important property of a radio telescope is its antenna pattern. This describes the response of a radio telescope to the received emission from a source.

An interferometer observes interference patterns, which are sets of consequent minima and maxima (fringes). Figure 2.1 illustrates the response of a two-element interferometer. The resulting output *(bottom panel)* results from a modulation of the fringe pattern *(middle panel)* with the response of a single antenna *(top panel)*, which reveals a main lobe with suppressed side lobes.

The main lobe describes the direction dependence of the response to a signal. However, the side lobes also contribute undesirably to the total emission received by radio telescopes. For an interferometric observation, measuring the same object with different baselines helps to minimize the contribution of
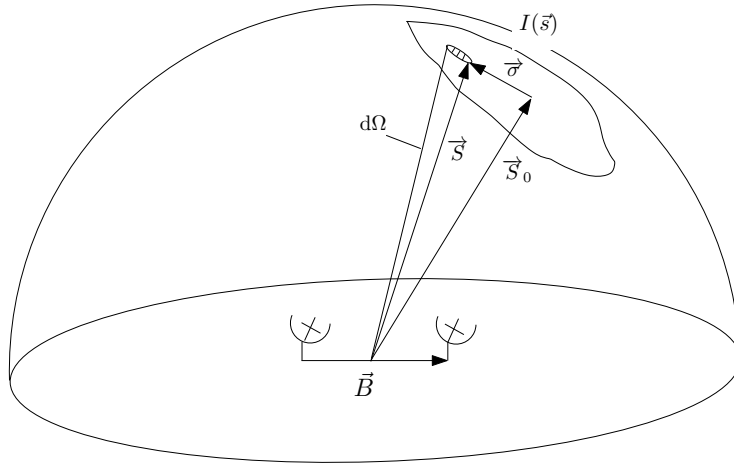
Figure 2.2: Sketch of an observation with a two-element interferometer.

side lobes to the received signal.

2.1.1 Single-dish radio observations

Raster imaging was the original method introduced for single-dish imaging. For raster imaging, the area to be observed is divided into different grids. The instrument measures the emission for each grid point until the entire area is captured. A significant fraction of observing time is lost due to the acceleration and deceleration of the telescope. Furthermore, a large number of single pointings is required to achieve a fully sampled data set (Shannon & Weaver 1949).

An alternative method to raster imaging is on-the-fly (OTF) mapping (Mangum et al. 2007). In OTF mapping the single-dish telescope moves continuously with a specific speed along right ascension and declination. OTF dumps are stored while the beam of the telescope moves across the source. The dumping speed must be fast enough so that two dumps per full width at half maximum (FWHM) can be stored (Nyquist theorem, Shannon & Weaver 1949). For the Effelsberg-Bonn H I Survey (EBHIS, Kerp et al. 2011) observations, however, the OTF dumps are stored every 500 ms, which is much faster. Due to the rapid storage the influence of short-term radio-frequency interference (RFI) is minimized. A comprehensive explanation of the method used for EBHIS is presented by Winkel et al. (2010).

2.1.2 Interferometric radio observations

The simplest interferometric array consists of two single-dish antennas (Fig. 2.3). The shortest possible distance between the two antennas is commonly referred to as the shortest baseline $\vec{B}_0$. $\vec{s}$ is the position vector associated to the single baseline $\vec{B}$, which reaches the both dishes with a geometric time delay τ_g, which varies with the length of the baseline:

$$c\,\tau_g = \vec{B}\,\vec{s}. \tag{2.2}$$

An additional time delay τ_i (Fig. 2.3) compensates for τ_g prior to the amplification of the incoming signals and their correlation. Both dishes are pointing at the same celestial coordinates and their main beam points in a specific direction $\vec{s_0}$, i.e., the center of phase. Different signals from different directions

$$cT_g = \vec{B}\vec{s}$$
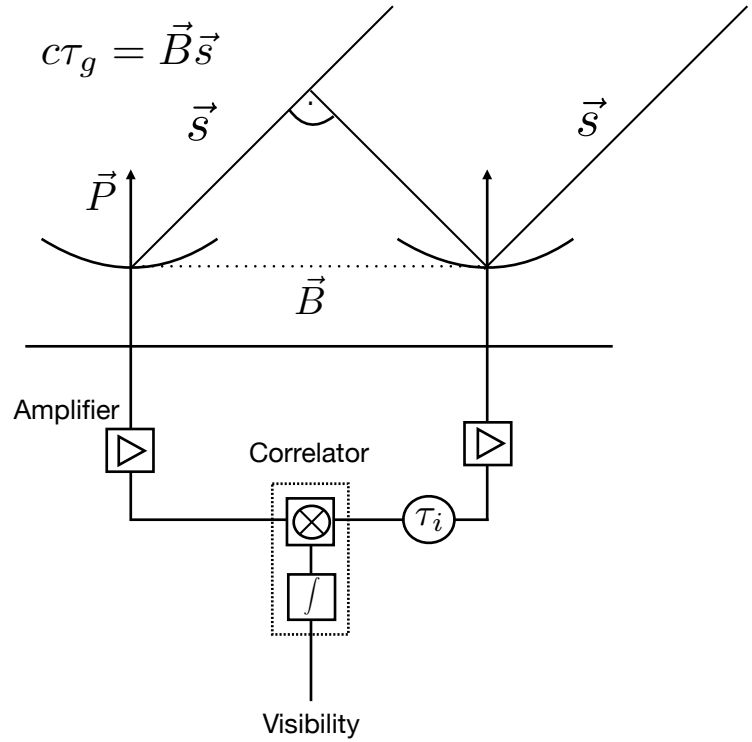
Figure 2.3: Schematic view of a two-element interferometer. $\vec{B}$ is the shortest possible baseline, τ_g the geometric delay of the incoming signal $\vec{s}$, and τ_i the so-called additional delay. $\vec{P}$ shows the direction of the main beam.

result in phase differences containing spatial information about the observed source. $\vec{\sigma}$ defines the relation between the pointing vector $\vec{s}$ and different positions in the source. $d\Omega$ is the beam-solid angle for a given baseline $\vec{B}$. Different baselines result in different $\vec{\sigma}$ (Fig. 2.2).

$$\vec{\sigma} = \vec{s} - \vec{s_0}. \tag{2.3}$$

Synthesis imaging

Each interferometer measures the visibility. This is to be understood as a cross correlation between voltage signals of two antennas, where the complex value presents both the amplitude and phase of the signal located in the field of view (FoV) of the antenna (see Fig. 2.3).

For each separation and orientation, the lobe pattern of the interferometer, i.e., synthesized beam, produces an output which is one sample of the Fourier transformation of the spatial distribution of the brightness of the observed object. This output is described by the visibility function.

$$V(u,v) = \iint I(\xi,\eta) \cdot e^{-i\,2\pi \cdot (u\cdot\xi + v\cdot\eta)} d\xi\, d\eta. \tag{2.4}$$

The intensity $I(\vec{s})$ is measured in real space. One distinguishes between spatial frequencies and spatial coordinates, where the spatial frequencies (u,v) are the Fourier duals of the spatial coordinates $\vec{\sigma} = (\xi,\eta)$ in the image plane. The brightness distribution of the source is retrieved via Fourier inversion from all the measured correlations for all $\vec{\sigma}$:

$$I(\xi, \eta) = \iint V(u, v) \cdot e^{i 2\pi \cdot (u \cdot \xi + v \cdot \eta)} du \, dv. \tag{2.5}$$

Sampling and (u, v) coverage

The measured visibilities are discrete values of the true visibility, which can be described by the following equation:

$$V^{\text{obs}}(u, v) = V^{\text{true}}(u, v) \cdot S_v(u, v) \tag{2.6}$$

$S_v(u, v)$ is the sampling function with

$$S_v(u, v) = \begin{cases} 1, & \text{if } (u, v) \in \text{observations} \\ 0, & \text{otherwise} \end{cases} \tag{2.7}$$

For an interferometric observation, measuring as many data points as possible is essential for a good image reconstruction. However, it is impossible to locate the telescopes at arbitrary positions, i.e., different baselines measure different spatial frequencies and it is not possible to have an infinite number of baselines. Because of this the (u, v) coverage, i.e., the distribution of visibilities is incomplete. Gaps in the (u, v) coverage limit the ability to reconstruct complex sources (Perley 1999). The under-sampled raw data produce artifacts in the final image. In order to reach a good (u, v) coverage the antennas should be located at many different positions during the observation. The measured visibilities are discrete.

The sampling of the (u, v) plane must comply with the Nyquist sampling theorem (Shannon & Weaver 1949). It is then possible to construct the image with the help of a finite number of sampling points. Astronomers also make use of the rotation of the Earth to complete the (u, v) coverage. Depending on the distribution of the (u, v) points, interferometric arrays can be more sensitive to small or rather large angular scale structures: large baselines correspond to high spatial frequencies, which in turn correspond to small spatial structures.

In practice, one uses the Fast Fourier Transformation (FFT) algorithm, as it is much more efficient. For FFT a regularly spaced grid of data is required. The size of the grid should be a power of two for best results. At this stage, an interpolation of the gridding points is required, as data points are measured hardly ever on a regular lattice (pixel size). Furthermore, a weight is assigned to each visibility measurement.

A detailed study of the weighting schemes and their impacts on the final image is presented in Chap. 4, where two imaging parameters: weighting scheme and pixel size, have been discussed.

Dirty beam and dirty image

Equation 2.6 reveals the relationship between the true visibility and the observed visibility. Using the inverse Fourier transformation and the convolution theorem, one retrieves the dirty image, which is the result of inverse Fourier transformation ($\mathfrak{F}^{-1}$) of the measured visibility function and the dirty beam. The latter is the inverse Fourier transformation of the sampling function $S(u, v)$. $*$ implies the convolution of the two inverse Fourier transformations:

$$
\begin{aligned}
\mathfrak{F}^{-1}(V^{\mathrm{obs}}(u,v)) &= \mathfrak{F}^{-1}(V^{\mathrm{true}}(u,v) \cdot S_v(u,v)) \qquad (2.8) \\
I^D(\xi,\eta) &= \mathfrak{F}^{-1}(V^{\mathrm{true}}(u,v) \cdot S_v(u,v)) \\
I^D(\xi,\eta) &= \mathfrak{F}^{-1}(V^{\mathrm{true}}(u,v)) * \mathfrak{F}^{-1}(S_v(u,v)).
\end{aligned}
$$

For randomly distributed visibility values, it is most efficient to apply a convolution. This ensures that each value of the interpolated visibility function is defined for all u and v. Fomalont (1999) mentioned common approaches regarding image correction and discussed two different image modifications, i.e., convolution and interpolation, in detail.

Synthesized image

After obtaining the dirty image, *cleaning* is necessary before the image can be used for scientific purposes, since the dirty image often contains diffraction structures, such as fringes or side lobes (sampling artifacts). Cleaning clears out the artifacts, using an appropriate deconvolution technique.

The basic concept of the clean algorithm is searching iteratively for bright points in the image and subtracting a small portion of the dirty beam from it until the entire emission is removed and only noise remains (Hogbom & Brouw 1974). The clean component is the position and amplitude of subtracted values, stored separately. The sum of all clean components is an approximation for the true image of the source. The cleaning depth, as well as the number of iterations, is empirical and varies significantly depending on the structure and science case. Nevertheless, an appropriate stopping criterion is of great importance for the reconstruction of true image of the sky.

2.1.3 Deconvolution

The *clean* algorithm as introduced by Hogbom & Brouw (1974) and its variants are the most common techniques and are widely used in synthesis imaging. A variety of modifications has been applied on the original method ever since to improve the performance (Clark 1980). However, for most astronomical objects, the assumption that the observed intensity distribution is a collection of point sources is not exactly valid. This was the main motivation for developing modifications as well as new deconvolution approaches for extended structures.

The clean algorithm (Hogbom & Brouw 1974) operates iteratively. It starts with the dirty image and defines a model which is blank before cleaning starts. The clean components (see step 2) are stored in this model. The subtraction of the the clean components from the original dirty image results in the residual maps. The clean algorithm requires exact knowledge of the synthesized beam (dirty beam) in order to distinguish between real structures and artifacts resulting from the side lobes in the dirty image. The algorithm consists of the following steps:

1. Determine the location $\vec{r}$ and value s of the peak in the dirty image.

2. A dirty beam centered on $\vec{r}$ and of amplitude λs is subtracted from the dirty image; $\lambda \ll 1$ and is known as the loop gain.

3. Clean components are stored in the model; residual map is computed.

4. The previous steps are repeated until the remaining peak is below a threshold defined initially by the user (clean depth). It should be noted that the search for the peak can also be restricted to a certain area in the dirty image, the clean window.

5. The final model consisting of the accumulative point sources with the clean beam, is convolved by a clean beam, which is usually an elliptical Gaussian fitted to the main lobe of the dirty beam.

6. The residuals are added to the clean image.

Although the clean algorithm is deterministic, the result of it depends strongly on human judgment. Therefore, it is necessary to address two important question regarding cleaning:

1. Is it possible to clean too deep?

2. Does the clean algorithm diverge?

From the theoretical point of view, it is possible to argue that *too deep cleaning* does not exist, since the cleaned image is a combination of all the cleaned components and residuals. This means that, independent of the number of clean components, the cleaned image contains all the components. In practice however, the cumulative flux as a function of clean components determines when the algorithm should stop (Mühle 2014, priv. comm.).

Wakker & Schwarz (1988) presented an approach, called Multi-Resolution Clean (MRC), to deal with clean deficiencies for extended sources. MRC does not modify the original clean algorithm but it breaks the cleaning into different steps distinguishing in resolution. MRC divides the original clean map into two components: diffuse and clumpy images. The diffuse image is the smoothed version of the dirty image, whereas the clumpy image consists of the difference between smoothed dirty and original image. Since the operation is linear, each map can be cleaned separately with the corresponding smoothed beam and dirty beam (Wakker & Schwarz 1988). The concatenation of both images results in the final image. For the final image, however, one needs to account for different gain and beam size. A detailed description is presented by Wakker & Schwarz (1988, their section 3.2).

Cornwell (1983) also showed that the original clean algorithm is in great need of improvement regarding flux reconstruction of extended sources. This author introduced the Multi-Scale Clean (MSC), which is the more common approach for cleaning extended sources. A brief introduction of modifications applied on clean algorithms and their impacts is provided by Cornwell (2008).

Stewart et al. (2011) discussed another case, where cleaning faces difficulties. They introduced an approach for overcoming cleaning limitations for sources varying in frequency and time. Cleaning should be handled with care, since it has important impacts on the final result. The difference between MSC and common clean is of interest, since all the presented objects are extended sources for the interferometric arrays. An overall comparison regarding this is presented by Rich et al. (2008) for a larger number of galaxies. However, in this work, the focus is on the combination. Chap. 4 of this thesis presents the results of different imaging parameters and clean philosophies as well as the effect of cleaning on the combination of low- and high-resolution data sets.

In addition to the clean algorithm, there also exist other deconvolution algorithms. However, they are not as commonly used as the clean algorithm. The most prominent algorithm from this list is the Maximum Entropy Deconvolution Method (MEM, Narayan & Nityananda 1986). MEM determines the best possible image for a set of measured visibilities. It is widely used for extend sources with low brightness where multiple pointings are required, whereas clean is more appropriate for point sources (Rohlfs & Wilson 2004). Sutter et al. (2013) presented an alternative approach for deconvolving and denoising radio interferometric images based on Gaussian process modelling. However, introduction and comparison of these methods is beyond the purpose of this thesis. In particular, because the classical deconvolution methods will still be mainly used in the near future.

2.1.4 Primary beam correction

The sensitivity of an instrument as a function of direction is described by the primary beam, which is usually approximated by a Gaussian. Therefore, the Eq. 2.4 needs to be modified by the beam pattern of a single antenna $A(\xi, \eta)$ as follows:

$$V(u, v) = \iint A(\xi, \eta) I(\xi, \eta) \cdot e^{-i\,2\pi \cdot (u \cdot \xi + v \cdot \eta)} d\xi\, d\eta. \tag{2.9}$$

The shape of the primary beam of the interferometric arrays has a strong impact on the final image. Especially if the size of the source to be imaged is comparable to the primary beam of the individual telescopes, i.e., for extended sources, then the power pattern of the primary beam will have a large effect. To account for this, one needs to perform the primary beam correction (PBC), i.e., performing the Fourier inversion and dividing the result by the primary beam $A(\xi, \eta)$.

The correction is typically conducted as a part of cleaning or as a post-imaging process. It is also essential in order to obtain true flux values. For PBC the deconvolved image is divided by the beam pattern of a single dish of the interferometric array (Eq. 2.10).

$$I_{\text{pbc}}(\xi, \eta) = \frac{I_{\text{deconv.}}(\xi, \eta)}{A(\xi, \eta)}. \tag{2.10}$$

For arrays consisting of identical single-dish telescopes, the primary beam pattern is identical for all the elements. For heterogeneous arrays, which consist of different single-dish instruments the primary beam correction is of course more complicated.

The correction also affects the properties of the noise in the data cube such that the noise level at the edges of the image is much higher than in the regions near the phase center. The noise of such a cube is highly position dependent.

For all the major instruments, specific functions or polynomials are known which describe the attenuation of the corresponding primary beam as a function of frequency and direction from the center of phase. These approximations can be very useful for masking of position-dependent noise in data sets, which are primary-beam corrected. In this thesis, primary beams of two instruments are of great importance: Very Large Array (VLA) and Westerbork Synthesis Radio Telescope (WSRT). Appendix D.1 presents a function and a polynomial to describe an empirical beam for the VLA and WSRT, respectively.

Subsequently, with respect to the PBC, the regions near the center of phase where the peak of Gaussian is located, achieve higher sensitivity. The sensitivity decreases for the regions further away from the center of the map. Prior to the combination of low- and high-resolution data, one needs to account for this variation. Also the choice of weighting schemes, i.e., the contribution of different parts of the visibilities to the final image needs to be accounted for. A more detailed study of this matter, in particular the impacts of different weighting schemes, are presented in Chap. 4.

2.1.5 Interferometric mosaic

There exist restrictions regarding the observation of extended sources with interferometric arrays. For a majority of celestial objects, one needs to consider two types of limitations in order to get a complete census of the extended structure. Firstly, the source can contain structures with spatial frequencies smaller than the shortest baseline ($\Theta > \lambda/b_{\text{min}}$), such that the interferometer is unable to image them. Secondly, the angular extent of the source can be large compared to the primary beam of a single

antenna ($\Theta > \lambda/D$), where D is the diameter of the single antenna of the interferometric array. In this case, the single pointing fails to image the complete structure. The approach to overcome the latter limitation is the so-called interferometric mosaicing (Holdaway 1999), i.e., a measurement consisting of a concatenation of different pointings.

There exists a number of approaches to perform the mosaicing: the linear combination of the single pointing (Holdaway 1999); joint deconvolution of the pointings (Sault et al. 1996); an additional approach to create an interferometric mosaic is adding the visibility measurements of individual pointings to obtain a so-called dirty mosaic.

- In the linear approach the interferometric mosaic consists of different single pointing observations, where each of these pointings is treated individually for imaging and deconvolution. The concatenation of all the cleaned pointings results in an interferometric mosaic. The concatenation occurs linearly considering proper weights for the primary beam (Holdaway 1999).

- In the joint deconvolution approach one requires a combined dirty image and a combined dirty beam. Here, the mosaicing occurs during the deconvolution. A detailed study of this approach has been presented by Sault et al. (1996).

Prior to any further analysis regarding the estimation of total flux and total H I mass the mosaic should be corrected for the primary beam shape. The mosaicing approaches affect the characteristics of root mean square (RMS) values as well as the measured gain in such a mosaic, significantly. As a result of this, both of these values are highly position dependent and regardless of mosaicing approach, the noise level in the overlap regions is lower. Appendix B provides detailed information about the measured RMS values in a data cube.

It should be noted that regardless of the mosaicing technique, the center of the (u, v) coverage is still incomplete. This is mostly significant if large-scale structure is present. Short-spacing correction (SSC), i.e., merging the interferometric data with those of single dish aims to provide this missing information. A detailed study of the SSC with a number of existing approaches as well as a new combination pipeline are presented in Chap. 3.

Stanimirović (1999) noted a very important fact. The deconvolution interpolates the missing information in the (u, v) coverage. However, it also tries to reconstruct the missing information in the central regions of the (u, v) coverage. The extrapolated information corresponding to spatial scales smaller than shortest measured spacing are unreliable. The author, however, argued that mosaicing reduces the shortest spacing to $d - D/2$, with d the size of the shortest baseline and D the size of a single antenna in the array.

2.2 H I surveys

Radio astronomy has experienced significant technical improvements regarding telescope backends and large performance enhancement in the field of software development in the last decade. Astronomers were able to cover larger areas on the sky and to process the raw data in a reasonable time.

In this regard, smaller and larger H I surveys have been carried out. Each of these surveys serves for a different scientific purpose. Some have been performed to complement the existing surveys. The larger surveys are mainly blind surveys, which cover a great portion of the sky, e.g., EBHIS or the Galactic All-Sky Survey (GASS, McClure-Griffiths et al. 2009; Kalberla et al. 2010). Smaller surveys focus preferentially on specific areas and achieve higher sensitivity as the result of longer integration time.

The major motivation for performing large-area surveys is the compilation of a complete picture of a certain astrophysical phenomenon. In addition to different spatial resolutions, they also cover a variety of velocity ranges. Some surveys aim for Galactic H I emission, e.g., GASS and the H I Parkes All-Sky Survey (HIPASS, Barnes et al. 2001), whereas other surveys investigate the emission from the extragalactic sources, e.g., the The H I Nearby Galaxy Survey (THINGS, Walter et al. 2008) or the Hydrogen Accretion in LOcal GAlaxieS (HALOGAS, Heald et al. 2011). Some surveys such as EBHIS cover both Galactic and extragalactic H I emission. A further characteristic is that GASS, HIPASS, and EBHIS are all blind surveys, whereas THINGS and HALOGAS are targeted surveys.

For the purpose of this dissertation a great ensemble of objects observed with both a single dish and an interferometer were required. In the first instance, the main interest is in investigating a possible approach for combining the low- and high-resolution data sets as well the impacts of imaging parameters on the cleaned interferometric images. The data sets presented in Chap. 3 were observed with the 64 m Parkes telescope and the Australia Telescope Compact Array (ATCA) [1](Stanimirović et al. 1999). For the data sets presented in Chap. 4, the single-dish data sets are mainly from EBHIS, whereas the interferometric data sets are from THINGS and the WSRT. The compact high-velocity clouds (CHVCs) presented in Chap. 5 are single observations carried out with the Effelsberg and the WSRT. The physical properties of each of these data sets are described in detail in the corresponding chapter. In the following section all the important surveys for this work are introduced in detail.

Effelsberg-Bonn H I Survey (EBHIS)   is a blind H I survey started in winter 2008/2009 Kerp et al. (2011). An L-band seven-feed-array receiver installed at the 100 m Effelsberg telescope in combination with modern Field Programmable Gate Array (FPGA) spectrometers make it possible to cover the whole northern sky hemisphere above -5° declination, observing both Galactic and extragalactic sky in parallel.

The modern spectrometers allow for 16,384 channels over 100 MHz of bandwidth. EBHIS covers the total local standard of rest (LSR) velocity ranges from -1000 km s^{-1} to +20,000 km s^{-1}, corresponding to redshift up to 0.07. The achieved spectral resolution of 1.28 km s^{-1} is sufficiently high for studying the Galactic H I (linewidth $\leq$ 4 km s^{-1}). Therefore, EBHIS is well suited for investigating faint, compact clouds around the Milky Way. The extragalactic data provide spectral resolutions between 10 km s^{-1} and 20 km s^{-1}, which is fine enough for faint extragalactic emission (Flöer 2010).

The first coverage of EBHIS was finished in Spring of 2013 and the data will be public in the near future. The observations have been carried out in the OTF mode (Sec. 2.1.1). The typical map size is 5° × 5°. The EBHIS science-ready data is processed for RFI, flux and gain-curve calibration, stray radiation removal (Kalberla et al., in prep.), baseline fitting, and gridding (Winkel et al. 2010). The system temperature varies from 22 to 39 K depending on elevation and Galactic continuum emission. The RMS noise ranges between 80 mK to 100 mK, depending on the elevation.

Galactic All-Sky Survey   (GASS, McClure-Griffiths et al. 2009; Kalberla et al. 2010) is a survey of Galactic H I of the southern sky ($\delta \geq +20°$) carried out with the 64 m Parkes telescope. The survey has been carried out in the OTF mode using a multi-feed array with 13 beams. The effective angular resolution is approx. 14' with a velocity resolution of 1.0 km s^{-1}. The measured RMS noise for the survey is 57 mK. The survey covers a LSR velocity range of $-400 \leq V \leq 500$ km s^{-1}. The Nyquist sampled data is suitable for combination with interferometric data to provide the missing-spacings information.

The H I Nearby Galaxies Survey   (THINGS, Walter et al. 2008) is a high spectral and spatial resolution pointed survey performed at the VLA. It comprises an ensemble of 34 Sa - Irr galaxies in a

---

[1] `http://www.narrabri.atnf.csiro.au`

Survey	θ	Δv [km s^{-1}]	ΔT [mK]	Coverage		Source
EBHIS	10.8'	1.25	80-100	$\delta \geq -5°$		Galactic and extragalactic
GASS	14.4'	1.0	57	$\delta \leq +2°$		Galactic
THINGS	6"	5.2	–	34	galaxies	extragalactic
HALOGAS	≈ 30"	5	–	24	galaxies	extragalactic

Table 2.1: Important parameters of the used surveys of 21-cm line emission for this thesis. EBHIS and GASS are single-dish surveys, THINGS and HALOGAS interferometric surveys. θ is the effective resolution of each survey. Δv the spectral resolution. ΔT is the RMS noise.

distance range of 3 to 10 Mpc. The total observation time for the survey accounts for ≈ 500 hours in the B,C and D array configurations. The array configuration is a designation of the extend of the telescopes and it decreases from A to D, which means A achieves the largest extend and therefore, can resolve the greatest detail. The less extended configurations are more suitable for studies of large scale structures, e.g., the extended diffuse gas. For the THINGS galaxies, visibilities from B,C and D arrays have been combined. This is of great advantage since different properties of the galaxies such as small structures and diffuse, low-temperature gas can be studied simultaneously. However, this makes the imaging process more complicated. THINGS achieves a spatial resolution of about 6″ and the velocity resolution is $1.3 \leq \Delta V \leq 5.2$ km s^{-1} with a sensitivity of 5×10^{19} cm^{-2}. The THINGS data sets are public [2]. The observations are available as natural (NA) and robust (RO) weighted data sets. In addition, the entire ensemble is residual rescaled and PBC (Walter et al. 2008). Both residual rescaling (App. D.2) and primary correction (Sec. 2.1.4) are essential for determination of the correct fluxes.

A smaller ensemble of the THINGS galaxies (29 galaxies) has been observed subsequently with the 100 m Effelsberg telescope within the framework of the EBHIS project (Kerp et al, in prep.). Ten of these galaxies are blended with Milky Way emission but the rest are well separated from the Milky Way (Walter et al. 2008, their Fig. 1).

Hydrogen accretion in LOcal GAlaxieS (HALOGAS, Heald et al. 2011) is a targeted H I interferometric survey carried out with the WSRT. The goal is providing deep observations (10×12 hour) for a sample of 24 nearby galaxies. One of the major goals of the survey is studying the gas accretion on the galaxies and its effects on the galaxy evolution. However, these deep observations are appropriate for studying any faint, diffuse gas around the galaxies. Its large-field, deep observations are important for studying systematics regarding the missing spacings (Chap. 3). An additional target of the survey is addressing the fundamental question regarding possible existence of high-velocity clouds (HVCs) in the halo of nearby galaxies. For this purpose, achieving a lower limit of 10^{19} cm^{-2} for column densities is essential. Different approaches have been tried to detect large quantities of cold, neutral gas around a number of nearby galaxies such as NGC 2403 (Fraternali et al. 2002), Andromeda galaxy (Westmeier et al. 2005a), NGC 891 (Oosterloo et al. 2007), NGC 3198 (Gentile et al. 2013), NGC 55 (Westmeier et al. 2013), UGCA 105 (Schmidt et al. 2014). With the help of HALOGAS ensemble it is possible to deepen the current knowledge of HVC in the halo of nearby galaxies.

---

[2] `http://www.mpia-hd.mpg.de/THINGS/Overview.html`

Merging of low- and high-resolution data sets

In the current chapter, short-spacing correction (SSC) also known as zero-spacing correction (ZSC) is addressed. A thorough understanding of this phenomenon is essential, since SSC bridges the gap between the two classes of radio telescopes, i.e., single dish and interferometers. Section 3.1 provides an overview of the missing-spacing problem (MSP). It gives an explanation of the problem and shows the necessity for the combination of single-dish and interferometric data sets for the study of large and small angular-scale structures of the same object. Section 3.2 provides an overview of the existing approaches. The section addresses important facts and points, which should be considered prior to the combination. Section 3.3 introduces a new implemented pipeline for performing SSC in the image domain. The algorithm has been evaluated with low- and high-resolution data sets of the Small Magellanic Cloud (SMC) obtained with the 64 m Parkes telescope and the Australia Telescope Compact Array (ATCA), respectively (Sec. 3.4). Section 3.5 offers a comparison with existing methods. Finally, a summary is presented.

3.1 Missing-spacing problem

Since the shortest baseline an interferometer can cover is given by the size of the dishes[1], the central part of the (u, v) coverage is never sampled. This lack of coverage at low spatial frequencies, known as the short-spacing problem (SSP), leads to an insensitivity of interferometers towards large angular scales. The SSP can be motivated as follows. The relationship between visibility and intensity has been described using equations 2.4 and 2.5:

$$V(u, v) = \iint I(\xi, \eta) \cdot e^{-i\, 2\pi \cdot (u \cdot \xi + v \cdot \eta)} d\xi \, d\eta$$

$$I(\xi, \eta) = \iint V(u, v) \cdot e^{i\, 2\pi \cdot (u \cdot \xi + v \cdot \eta)} du \, dv.$$

---

[1] Additionally, a phenomenon known as shadowing might have some impacts on the result of the observation if two dishes are very close. Shadowing occurs when the beam of one dish is obscured by another dish, which can occur particularly at low elevations.

The total flux for a given source is then given by:

$$S_{\text{tot}} = \int\limits_{\text{source}} I \, d\Omega. \tag{3.1}$$

The central part of the (u, v) coverage is not sampled, therefore,

$$u = v = 0 \Rightarrow V(0, 0) = S_{\text{tot}} = 0. \tag{3.2}$$

This illustrates that for an interferometer, which is not able to measure the central part of the (u, v) coverage, the measurement of the total flux will yield naught.

Figure 3.1 illustrates the effect of missing spacings on the interferometric image (Braun & Walterbos 1985). *The left panel* shows three different box functions in the spatial frequency domain, whereas the right panel presents the same function in the image domain. *The bottom left panel* shows a simplified version of the (u, v) coverage for an interferometer, where the central region of it is not sampled. The result in the image domain is a sinc function with distinguished negative bowls around the structure.
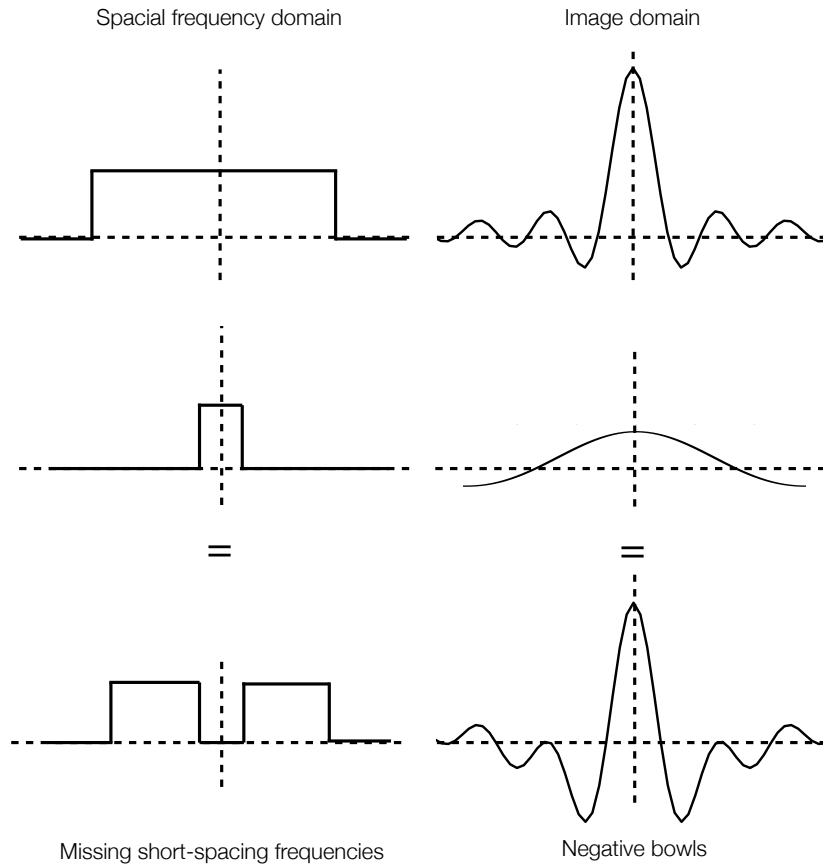
Figure 3.1: Illustration of the effect of the MSP recreated after Braun & Walterbos (1985). *The left panel* shows three different box functions in the frequency domain. *The right panel* shows the corresponding Fourier transformation of each function. *The bottom left panel* represents the simplified (u, v) coverage of an interferometer, where the central region of the (u, v) coverage is not sampled. The Fourier transformation of this function is a sinc function with high amplitude negative bowls.

Schwarz & Wakker (1991) show that for some synthesis observations the lack of short spacings can not be tolerated, e.g., if the emission fills the whole primary beam. Furthermore, they introduce a factor θ_m. It is the least size of the structure in one direction as the crucial size for an extended structure. For these structures, restoration techniques using only the interferometric data are able to fill the gap that arises from the lack of coverage at low spatial frequencies in interferometric observations. For larger structures the SSC is inevitable. To overcome this problem, interferometric data has to be combined with single-dish observations, which contain the information about the largest angular scales. With the help of both single-dish and interferometric observations, it is possible to study different properties of the same object.

3.2 Existing approaches and motivation for a new algorithm

The MSP also known as SSP has been a very well known phenomenon from the earliest stages of interferometry on. Nevertheless, the number of existing publications regarding the SSC in the literature is very limited. The correction is important, since it brings the best of both data sets together, i.e., high angular resolution of an interferometer and total flux measured by a single-dish telescope. However, there are several points, which should be considered prior to the combination of single-dish and interferometric data sets. Performing the SSC is not always feasible. The correction is important for the objects that reveal considerable amount of diffuse, extended structures. For these objects the measured flux densities in the low- and high-resolution data sets show a significant difference. For Galactic objects as well as a number of nearby galaxies adding the missing-spacing information is crucial for studying the star formation regions as well as for tracing the impacts of gas inflows in these regions. Additionally, the correction is important for the neutral gas mass determination, as well as for studying the decomposition of the interstellar medium (ISM) phases. The amount of missing flux depends highly on the physical and morphological properties and on the proximity of the object.

Stanimirović (2002) argued that different combination approaches are able to produce acceptable results for the combination regarding the flux consistency if the calibration in the overlap region of both high- and low-resolution data sets are in good agreement.

Stanimirović (2002) poses two questions in order to solve the MSP:

1. How to provide the missing data?

2. How to combine the missing data with interferometric observations?

The choice of single-dish telescope to provide the required information for solving the MSP is essential. For the combination, interferometric and single-dish observations need to overlap in the ranges of spatial scale they are sensitive to. The overlap region corresponds to the structures towards which both interferometer and single dish are sensitive. Figure 3.2 shows a schematic scheme of the overlap region between the single-dish and interferometer as a function of (u, v) distance, i.e, the baselines.

Furthermore, both observations must be conducted at the same frequency (wavelength). The integration time for both interferometric and single-dish observations also plays a significant role in the result of the combination. Especially for upcoming deep interferometric observations, the difference between the total integration time for single-dish and interferometric observation is crucial. For a reasonable combination of deep interferometric observations, longer single-dish observations are required. Vogel et al. (1984) argued that the measured signal-to-noise ratio for the visibilities from the single-dish should be comparable with the measured values from the interferometric visibilities in the overlap region, i.e., measured values in the shortest baselines, in order to avoid any depreciation in the combined map. For instance, for the sample of Hydrogen Accretion in LOcal GAlaxieS (HALOGAS, Heald et al. 2011)
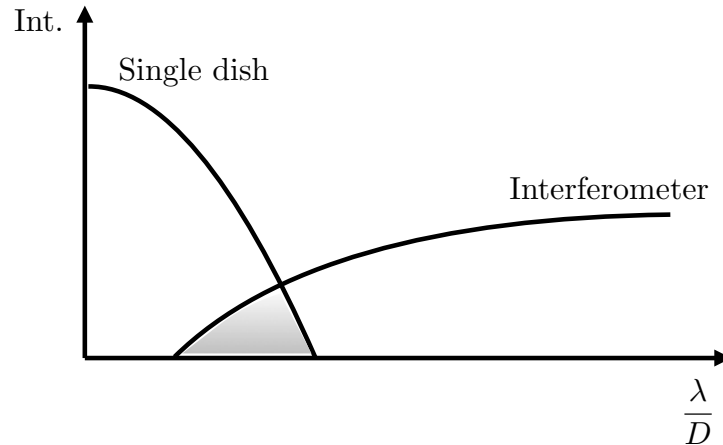
Figure 3.2: Schematic view of the overlap region between single dish and interferometer. The overlap region corresponds to the structures towards which both instruments are sensitive.

(Chap. 2.2) galaxies observed with the 100 m Effelsberg telescope, the integration time has been chosen such that the measured root mean square (RMS) noise level in the Effelsberg data cube is of the same order of the measured RMS noise level of the shortest baselines in the WSRT data sets. For these observations the technique of basket weaving as introduced by Winkel et al. (2012a) has been applied.

Secondly, one has to consider how to perform the SSC, since there exist different approaches and each approach has its advantages and disadvantages. The existing approaches are developed mainly for only one or a restricted number of objects. Moreover, approaches differ depending on if the combination is performed before or after the deconvolution. One work that performs the combination prior to the deconvolution is Stanimirović et al. (1999), who performed the combination on the basis of the interferometric dirty image. Their method has been evaluated with observations obtained with the 64 m Parkes telescope and with ATCA. The same data sets have been used for the evaluation of the performance of the algorithm introduced in this work. Section 3.4 presents the result of the combination for these data sets. It also provides a comparison between the results of both approaches.

Another important aspect regarding the combination is the choice of combination domain. The combination of two data sets can be performed either in the image- (Ye et al. 1991; Chemin et al. 2009) or in the frequency domain (Bajaja & van Albada 1979; Vogel et al. 1984).

Combination in the frequency domain will be a real challenge in the case of large data sets. This aspect is essential for the upcoming pathfinders of the Square Kilometer Array (SKA, Johnston et al. 2009) such as the Australia's Square Kilometer Array Pathfinder (ASKAP, Duffy et al. 2012). Since the amount of data these systems produce is much larger compared to current interferometric arrays. In this case, it will be very difficult to get access to the original visibilities, in order to add the pseudo visibilities coming from a single-dish prior to the deconvoltion. In particular, since adding the missing information at this stage certainly increases the operating expense in the data reduction process. The edge-effects are also significant when Fourier transforming to the (u, v) domain, if the structure is very extended and column densities are significant at the edge of the surveyed region[2]. This can lead to horizontal and vertical artifacts present in the combined map in particular for bright continuum sources or H $\scriptstyle\mathrm{I}$ 21-cm line observations with significant amount of information at the edges of the mapped area (for more information see Gibbs phenomenon, Gibbs 1899).

---

[2] This is the case for the majority of Galactic objects

Furthermore, the different approaches differ in their required input data. For most of the methods, additional information such as visibilities, beam patterns or dirty images are of great importance (e.g., Kurono et al. 2009; Stanimirović 2002; Weiß et al. 2001). Yet, it is common that one only has access to the final data products, such as cleaned images and retrieving the supplementary information can be difficult.

The combination is a complex approach, since the nature of both observations and the involved physical principles differ significantly (see Chap. 2). Data reduction packages, such as CASA or MIRIAD, provide easy-to-use tasks to perform the combination using only the cleaned interferometric and single-dish data. However, often these packages function as a black box, which makes it difficult to analyze the result.

Therefore, it has been decided to design and implement a new pipeline to perform the SSC in the image domain. The approach to be introduced addresses a number of important questions, including the impacts of some of the imaging parameters, e.g., pixel size and weighting schemes on the result of the combination (Chap. 4). The focus is on the cleaned interferometric images, since the majority of interferometric data sets stored on disks are cleaned images. The algorithm does not require any additional information, e.g., exact knowledge of the dirty beam. In general, the same approach can be applied on dirty images prior to the deconvolution. In this case, a combined beam is required for a proper deconvolution as described by Stanimirović (2002) or Kurono et al. (2009).

Section 3.3 presents the ground principle of the implemented pipeline for the purpose of this work. The section focuses on the physical and astronomical aspects of the pipeline. A detailed description of the pipeline's constitution and functionality is presented in App. C. It provides detailed information regarding the overall structure of the pipeline as well as used functions and routines for realizing the approach.

3.3 Principle of the pipeline

In short, the combination pipeline operates as follows. In the first step, different projection and geometry for single-dish and interferometric data are accounted for; then the interferometric data are smoothed to the resolution of the single dish, and then subtracted from the single-dish data. The resulting difference cube contains only diffuse extended neutral atomic hydrogen (H I) structures detectable by the single dish. Finally, this is added to the interferometric data cube.

This procedure allows to recover both the complete flux from the single dish and the highest angular resolution of the interferometer.

As already mentioned, both single-dish telescopes and interferometers are sensitive towards the detection of different components of the same structure. However, in some cases there are structures towards which both of the instruments are sensitive, i.e., with spatial scales located in the overlap region (Fig. 3.2). The difference between single-dish and interferometric data sets reveals the missing information detectable only with the single-dish telescope (Fig. 3.5, panel c). This corresponds to the low spatial frequencies in the (u, v) domain and extended and diffuse structures in the image domain (Sec. 3.1). Once the missing information is obtained it can be added to the interferometric data set for filling the gaps around the central regions of the (u, v) coverage. Figure 3.3 provides a schematic view of the data flow, different components, and the internal constitution of the pipeline. The retrieved values from the header are presented with dotted lines. The solid lines present the data flow of the pipeline.

- **Importing FITS files:** The first step is importing the single-dish and interferometric Flexible
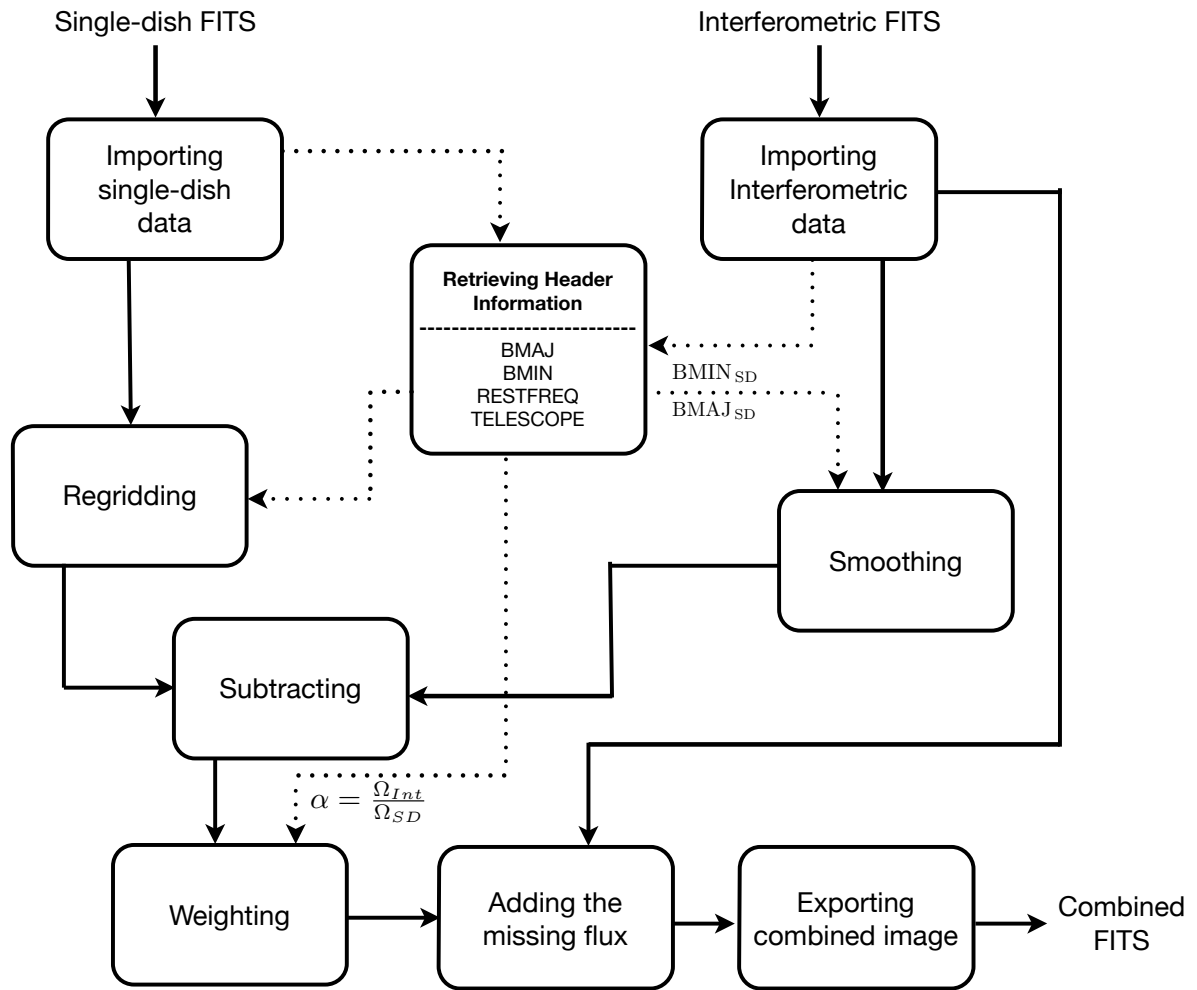
Figure 3.3: Data flow scheme of the developed short-spacing pipeline in the image domain. The dotted lines represent retrieved values from the header. The solid lines present the data flow of the pipeline. The input of the combination pipeline are the low- (single-dish) and high-resolution (interferometeric) data sets. The output is the merged data set.

Image Transport System (FITS) files[3]. A number of subroutines retrieve the required information from the headers of single-dish and interferometric data sets. This information is necessary for regridding and convolving the data sets. The dotted lines in Fig. 3.3 indicate the steps that require information from the header.

- **Regridding of single-dish data:** Often, the single-dish and interferometric data have different coordinate systems, or have different projections on the celestial sky. Furthermore, the size of the field of view (FoV) and the pixel size can differ. To be able to perform the SSC, these parameters need to be identical for both data sets. Thus, to prepare these data sets for the combination, reprojection to the same coordinate system and type of projection on the celestial sphere, as well as interpolation is required *(regridding)*[4].

  The used interpolation scheme for the presented data in this work is linear. Linear interpolation is flux conserving, which is a decisive factor for the combination. However, it also introduces some artifacts which can affect the result of the combination.

- **Convolving of interferometric data:** The interferometric data set needs to be convolved with a two dimensional Gaussian kernel, such that the full width at half maximum (FWHM) of the beam major and minor axes of the convolved image equal those of the single-dish instrument *(smoothing)*. This is to put the interferometer data on the same spatial resolution as the single-dish data. After the convolution, the interferometric data cube has the same angular resolution as of the regridded single-dish data cube.

- **Determination of missing spacings:** The convolved interferometric data subtracted from the regridded single-dish data results in a new data cube *(subtracting)*. The resulting data cube contains the missing information that the interferometer lacks.

- **Weighting of missing spacings:** Before this information can be added to the interferometric data set, the data has to be weighted with a factor α. Stanimirović (2002) argued: "for an extended source I_{Int} and I_{SD} are often, for convenience, expressed in units of $\mathrm{Jy\,beam^{-1}}$ not $\mathrm{Jy\,sr^{-1}}$, and so will be different numbers because of the different beams considered (with beam areas Ω_{Int} and Ω_{SD}, respectively). For this purpose, an estimate of the resolution difference between the two data sets ($\alpha = \Omega_{\mathrm{Int}}/\Omega_{\mathrm{SD}}$) is also needed" (Eq. D.2). Therefore, the missing information is scaled by α to account for different resolutions in both data sets *(weighting)*. The weighting factor is mandatory for data sets in units of $\mathrm{Jy\,beam^{-1}}$. For data sets in units of Kelvin, however, the weighting step is redundant, since the difference in brightness caused by different resolutions has been considered during the conversion from $\mathrm{Jy\,beam^{-1}}$ to Kelvin. Appendix A describes the relationship between flux density in units of $\mathrm{Jy\,beam^{-1}}$ and brightness temperature in units of Kelvin.

- **Adding the missing spacings:** Once the difference between both data sets is properly determined the information must be added to the interferometric data set *(adding the missing flux)*.

- **Exporting the combined FITS file:** As a final step, the combined Common Astronomy Software Applications (CASA, McMullin et al. 2007) image is exported as a FITS file. Appendix C provides detailed information regarding the internal constitution of the introduced pipeline. All the involved tasks, tools, and subroutines are explained in detail.

---

[3] FITS is a standardized file format, which is commonly used for storing scientific data. Each file consists of a ASCII header with specific keywords that is easily readable for both human and machine.

[4] The designation of the corresponding step in the pipeline (see Fig. 3.3).

3.4 Evaluation and comparison of combined data sets

The current section introduces the result of the combination of low- and high-resolution data sets using the introduced pipeline. The data sets stem from a previous study conducted by Stanimirović (1999). She used observations with the 64 m Parkes telescope, the ATCA, and the result of their combination to investigate the H I distribution as well as the kinematics of the SMC. The result of the studies regarding the kinematics of the SMC as well as the spatial correlation of dust and gas in the cloud are presented in Stanimirović et al. (1999).

3.4.1 The small Magellanic cloud

The SMC is a nearby dwarf irregular galaxy with a complex morphology. The previous studies show that the galaxy has a considerable amount of diffuse and warm gas as well as small, compact clumps (Staveley-Smith et al. 1997; Stanimirović et al. 1999). Hence, the SMC is an interesting testbed for studying different components of the ISM. It is also one of the most suitable objects for studying the impacts of the SSC, since both warm and cold components are present significantly.

The SMC is smaller than the Large Magellanic Cloud (LMC). The assumed distance to the SMC is about 60 kpc, which corresponds to an H I mass of $3.4 \times 10^8 \leq M_\odot \leq 5.5 \times 10^8$ (Bajaja & Loiseau 1982; Stanimirović 1999; Putman et al. 2003; Brüns et al. 2005). The variation in the measured H I masses is mostly due to different FoVs of the corresponding observation (Putman et al. 2003). Stanimirović (1999) assumed a distance of approx. 60 kpc to the SMC for her calculations, which is in agreement with the result of the more recent study done by Graczyk et al. (2014) proposing a distance of 62.1 ± 1.9 kpc to the SMC. The distance of ≈ 60 kpc has been also assumed for the driven values in this work.

Figure 3.4 shows the column density maps for both the LMC and SMC (Planck Collaboration et al. 2013) as well as their relative position to the Milky Way based on the LAB observations.

The SMC is located at the southeast edge of the LMC at $L_M \approx 340°$[5]. The bridge between the LMC and SMC consists mainly of gas without any considerable star formation. It is the result of the encounter of the both clouds, where the ISM flows in the direction of the more massive object. *The upper panel* presents both Magellanic clouds embedded in the strong Milky Way emission. *The bottom panel* presents the Magellanic clouds without the Milky Way emission. The separation is based on the numerical model developed by Kalberla & Dedes (2008).

3.4.2 The SMC observations and data

A detailed description of the SMC observations and the data reduction process has been presented by Stanimirović (1999). She used these data sets to study the overall properties of the ISM embedded in and around the SMC. For this purpose both single-dish and interferometric data sets have been combined. For the combination four different approaches have been evaluated. Section 3.4.3 presents a brief introduction of the methods used by Stanimirović (1999). It also provides a comparison between the presented results in the aforementioned work and the result of the combination using the algorithm introduced in the current work (Sec. 3.3)

The 21 cm line observations of the SMC reveal a complex morphology in the H I gas (Fig. 3.5, panel d). The SMC comprises a non-symmetric and non-spherical shape, in particular obvious in the Parkes and the combined data set (Fig. 3.5, panel a and d). The interferometric data set shows small-scale structures in form of small arches and small clumps. The disruption of the SMC, especially observable

---

[5] The maps are in the Magellanic coordinates as described by Nidever et al. (2008). The center of the LMC is defined as the Magellanic longitude $L_M = 0°$.
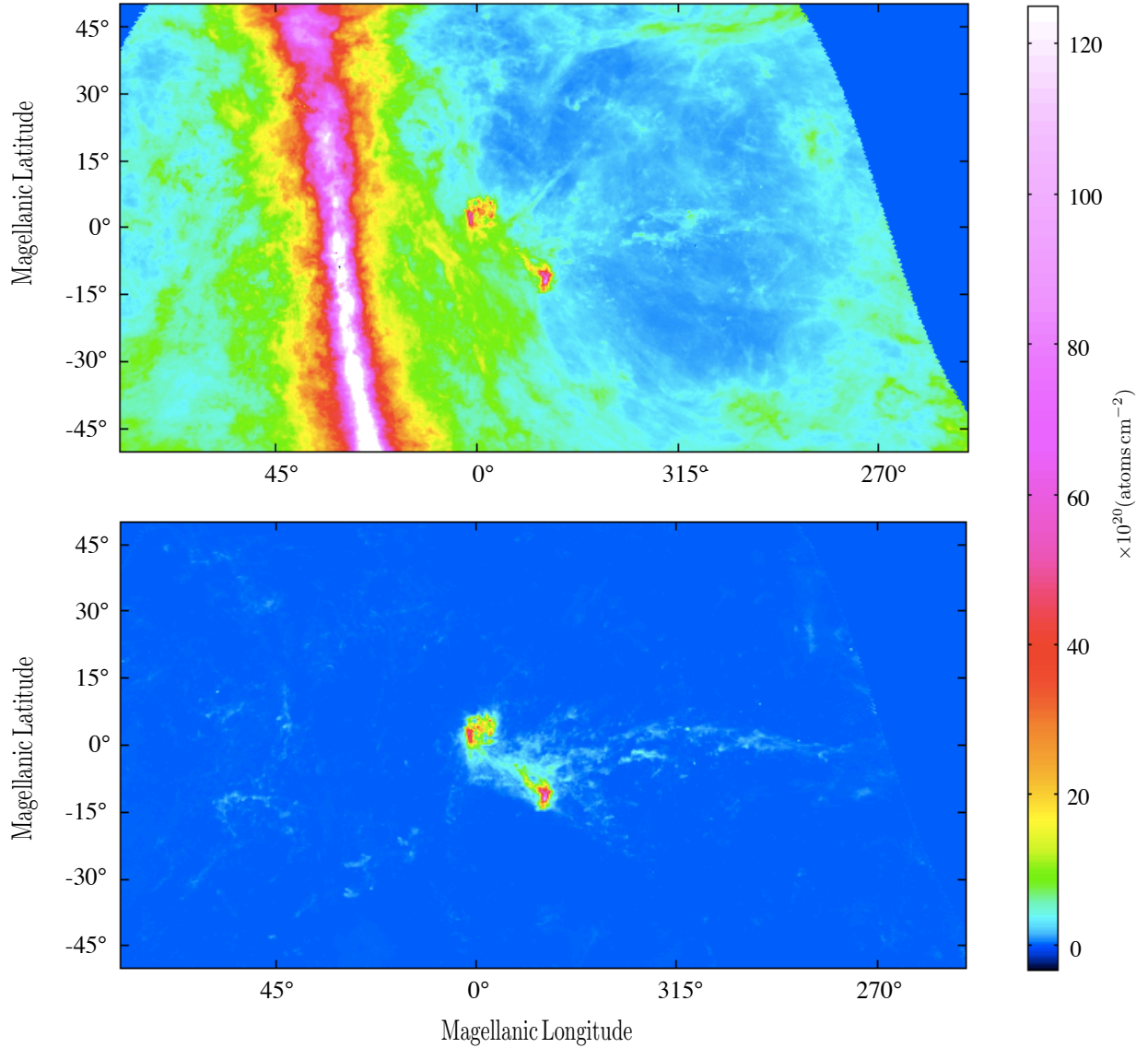
Figure 3.4: Column density maps of the LMC, SMC, and their relative location to the Milky way based on Galactic All-Sky Survey (GASS, McClure-Griffiths et al. 2009; Kalberla et al. 2010) observations. The maps are in the Magellanic coordinates as described by Nidever et al. (2008). *The top panel:* both Magellanic clouds embedded in the strong Milky Way emission. *The bottom panel:* the Milky Way emission has been eliminated using the numerical model developed by (Kalberla & Dedes 2008) based on Leiden/Argentine/Bonn Galactic H I Survey (LAB, Kalberla et al. 2005) observations (Planck Collaboration et al. 2013). The center of the LMC is defined as the Magellanic longitude $L_M = 0°$. The SMC is located in the southeast edge of the LMC approx. at $L_M = 340°$.

Characteristic	SD_{reg}	Int	Unit
Type	irregular dwarf galaxy		
Distance	60		[kpc]
Total covered area	20		[degrees^2]
Spectral resolution	1.65		[km s^{-1}]
Heliocentric velocity range	$88 \leq V_{helio} \leq 216$		[km s^{-1}]
Angular resolution	18.8'	98"	
RMS values	180	30	[Jy beam^{-1}]

Table 3.1: Physical and observational parameters of the SMC

in the combined data set, is believed to be the result of interaction with the LMC and the Milky Way (Stanimirović 1999; Putman et al. 2003, and references therein).

Both the interferometric and single-dish observations cover a total area of 4.5° × 4.5°. In order to cover the area of approximately 20 degrees^2, an interferometric mosaic was created using 320 pointing centers. The mosaicing has been performed using the approach introduced by Staveley-Smith et al. (1997). Moreover, the final dirty cube has been deconvolved using the Maximum Entropy Deconvolution Method (MEM, Narayan & Nityananda 1986). A brief description of this method is presented in Sec. 2.1.3. The FWHM of the beam major and minor axes in the cleaned interferometric cube is ≈ 98 arcsec. The data cube is in units of Jy beam^{-1} and has a size of 578 × 610 × 78 in RA, DEC, and frequency, respectively. The spectral resolution is ≈ 1.65 km s^{-1} with heliocentric velocities ranging $88 \leq V_{helio} \leq 216$ km s^{-1}. The measured RMS noise level in the emission-free regions of the interferometric cube is approx. 20-30 mJy beam^{-1}. High-resolution observations of the object reveal the filamentary structure of the SMC. The measured total flux in the velocity-integrated map is ≈ 1.4×10^5 Jy km s^{-1} for the interferometric data cube.

The single-dish raw data has been convolved onto a grid using a Gaussian convolution kernel with an FWHM of approximately 12 arcmin. The Parkes data set has been regridded prior to the combination according to the ATCA data set. This resulted in a new data cube with the north celestial projection (NCP) as that of the ATCA data cube. `HGEOM` from the Astronomical Image Processing System (AIPS, Greisen 1990) software package has been used originally to perform the regridding. The preliminary results of the regridding were unsatisfactory and therefore, it has been repeated. In a further attempt, the single-dish data has been gridded with a larger convolving function and with a pixel size of 30 arcsec as for the interferometric data cube. Consequently, the angular resolution of the new Parkes data cube has been broadened to 18.8 arcmin (Stanimirović 1999). The spectral resolution in the regridded single-dish data is ≈ 1.65 km s^{-1}, which is the same as the measured channel width in the interferometric cube. The measured RMS noise level in the regridded single-dish data cube is approx. 150-180 mJy beam^{-1}.

A comparison of the total fluxes measured in the regridded single-dish and interferometric data set reveals that the SMC has a considerable amount of diffuse and warm gas (Fig. 3.10). Table 3.1 summarizes the physical and observational properties of the low- and high-resolution data sets for the SMC. Section 3.4.3 introduces the result of SSC for the SMC data sets.

3.4.3 Short-spacing correction for the SMC data

The SSC has been performed using the SMC data sets as described in Sec. 3.4.2. The regridded Parkes and the interferometric data sets are the inputs for the combination pipeline.

Stanimirović (1999) has noted that a *gridding correction factor* of 1.63 was applied. The factor is the ratio of the new and old beam areas of the single-dish data cubes and "ensures that the measured peak flux density for a point source is equal to its true value" (Stanimirović et al. 1999, and references therein). Therefore, the combination has been performed for two cases, considering the gridding factor and without it. For the former case, the original Parkes data set has been multiplied by the beam correction factor of 1.63.

Figure 3.5 comprises different flux density maps for the SMC. Panel (a) shows the regridded Parkes H I 21 cm flux density map, panel (b) the corresponding ATCA maps, and panel (d) the flux density map of the combination. The measured total flux in the regridded Parkes and combined data is $\approx 4.1 \times 10^5$ Jy km s^{-1}. The corresponding value for the ATCA data is $\approx 1.4 \times 10^5$ Jy km s^{-1}, respectively. A comparison between measured total fluxes reveals a $\approx 65\%$ higher total flux density in the combined map than in the interferometric map. The large difference suggests that the SMC consists of a considerable amount of diffuse and warm gas, towards which the interferometer is insensitive.

The single-dish observations suggest that the H I gas density increases from the east to the west wing in the SMC, where the densest region in both single-dish and interferometric maps is located in the southwest edge of the SMC. In the combined map, three adjacent smaller dense regions are observable. The most dense region in the combined data cube is located at the position with RA: $00^h : 47^m : 33^s$ and Dec: $-73^\circ.05^m.27^s$ and accounts for ≈ 114.1 Jy beam^{-1} km s^{-1}.

The SMC reveals an estimated velocity gradient of about 110 km s^{-1} in its velocity distribution (Fig. 3.5, panel e). The peak velocity measured in the southwest edge of the cloud is ≈ 90 km s^{-1}, in the northeast edge of the SMC ≈ 200 km s^{-1}, respectively. The measured values in the southeast edge of the cloud suggest a velocity gradient of about ≈ 180 km s^{-1}. The strong velocity gradient measured in the cloud as well as its distribution can be due to its proper motion. However, the tidal interaction between the SMC, LMC, and Milky Way may also affect it. An additional process, which affects the morphology of the SMC are the H I shells (Staveley-Smith et al. 1997). Staveley-Smith et al. (1997) were able to determine numerous arch-shaped structures, the so-called shells in the position-velocity images. They argued that these structures are ISM, which is driven away by the stellar wind of massive stars or as a result of a supernova explosion (Staveley-Smith et al. 1997, and references therein).

Stanimirović (1999) was able to detect three super giant shells after combing the single-dish and interferometric data. She located these at the northeast, southeast and southwest wings of the cloud. These are the regions with distinguished velocity gradients, which are also observable in the combined map presented in this work.

The combination has also been performed for the SMC data without considering the gridding factor (Fig. 3.9). The observational parameters of the input data cubes, i.e., the regridded Parkes data cube as well as the ATCA data cube are the same as described previously. However, the measured total flux in the regridded and combined data cube is about $\approx 2.5 \times 10^5$ Jy km s^{-1}. The measured value in the interferometric data cube is $\approx 1.4 \times 10^5$ Jy km s^{-1}. The difference in measured total fluxes for the combined and interferometric data cubes is about 43%. The measured total flux in the combined data sets are in very good agreement with the measured values in the regridded single-dish cubes in both cases (with or without the gridding factor).

Table 3.2 summarizes the H I masses calculated for different data sets. For these estimates, the assumed distance to the SMC is 60 kpc. Regarding the total flux values and the H I masses two cases have been considered: with (a) or without the gridding factor (b). The measured total flux in the combined data cube with consideration of the gridding factor as described in Sec. 3.4.3 corresponds to a total H I mass of 3.4×10^8 M$_\odot$ (a). Without considering the gridding factor, the estimated H I mass accounts for 2.1×10^8 M$_\odot$ (b). The former value (a) is in agreement with the reported value by Putman et al. (2003) (3.4×10^8 M$_\odot$ - their Table 2). Brüns et al. (2005) estimated 4.0×10^8 M$_\odot$ (their Table 3). Stanimirović

(a) SMC: Parkes$_{reg}$

(b) SMC: ATCA

(c) SMC: Parkes$_{reg}$ - ATCA
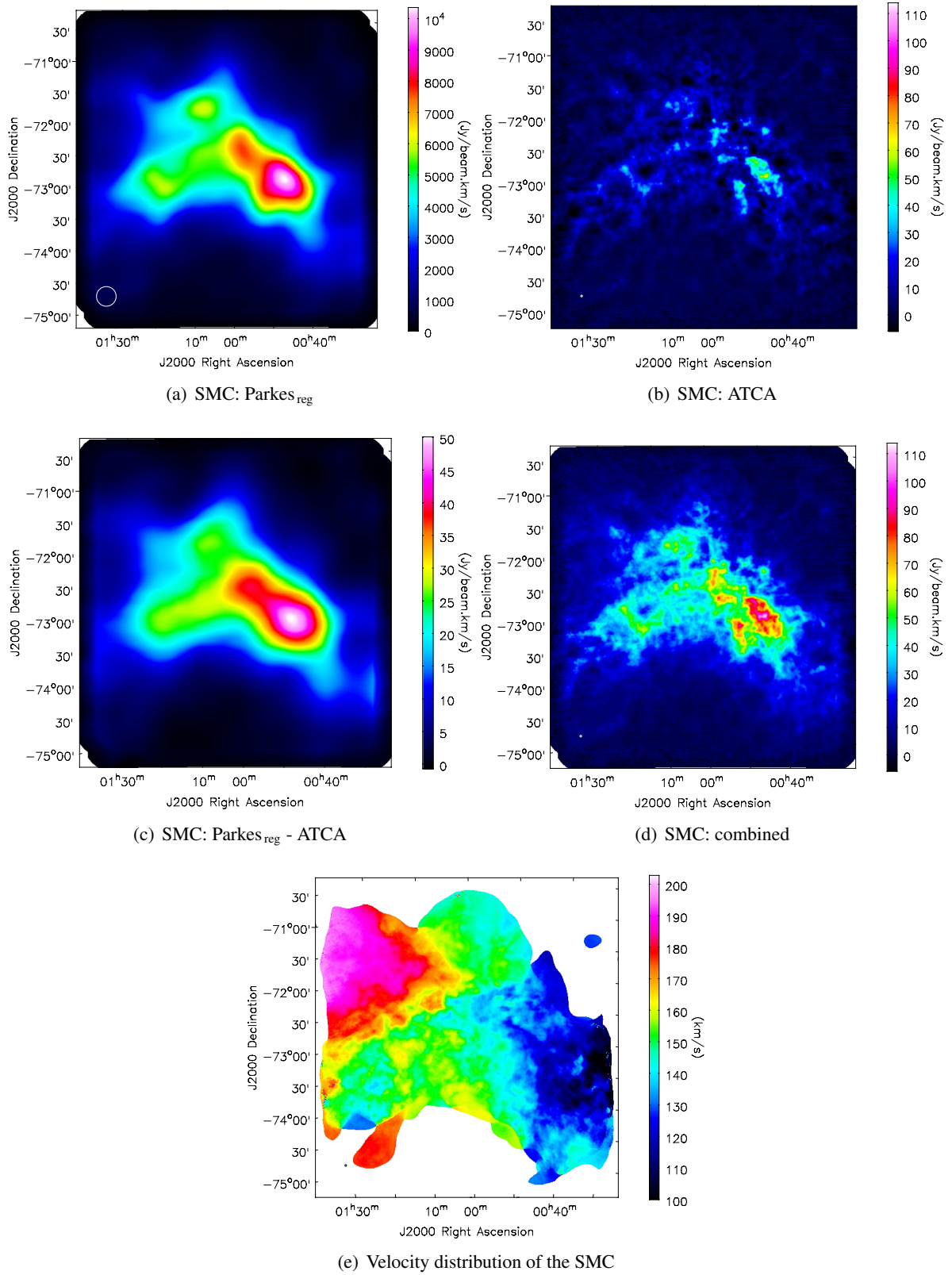
(d) SMC: combined

(e) Velocity distribution of the SMC

Figure 3.5: The SMC flux density maps. Panel (a) shows the regridded flux density map of the Parkes data; panel (b) flux density map of the ATCA data; panel (c) the combined flux density map; panel (d) flux density measured only by the single dish; and panel (e) the velocity distribution of the SMC measured in the combined map. The estimated velocity gradient is about $100 \, \mathrm{km \, s^{-1}}$ obvious from the northeast to the southeast edge of the cloud.
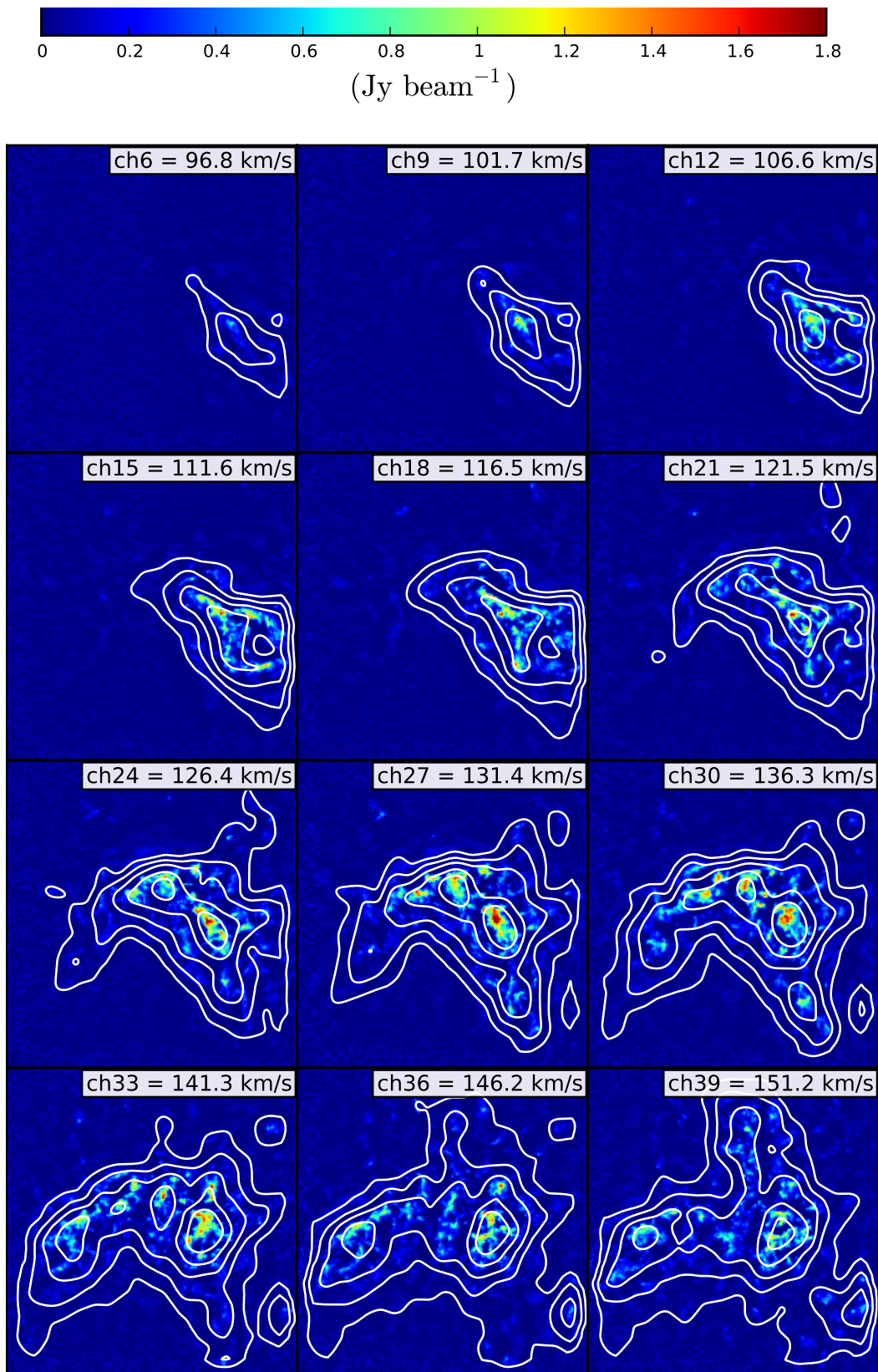
38

Figure 3.6: Multi-channel map of the SMC. The ATCA data set is overlaid with contours from the Parkes data. The contour levels are 10, 20, 40, 80, and 130 Jy beam^{-1} for the Parkes cube.
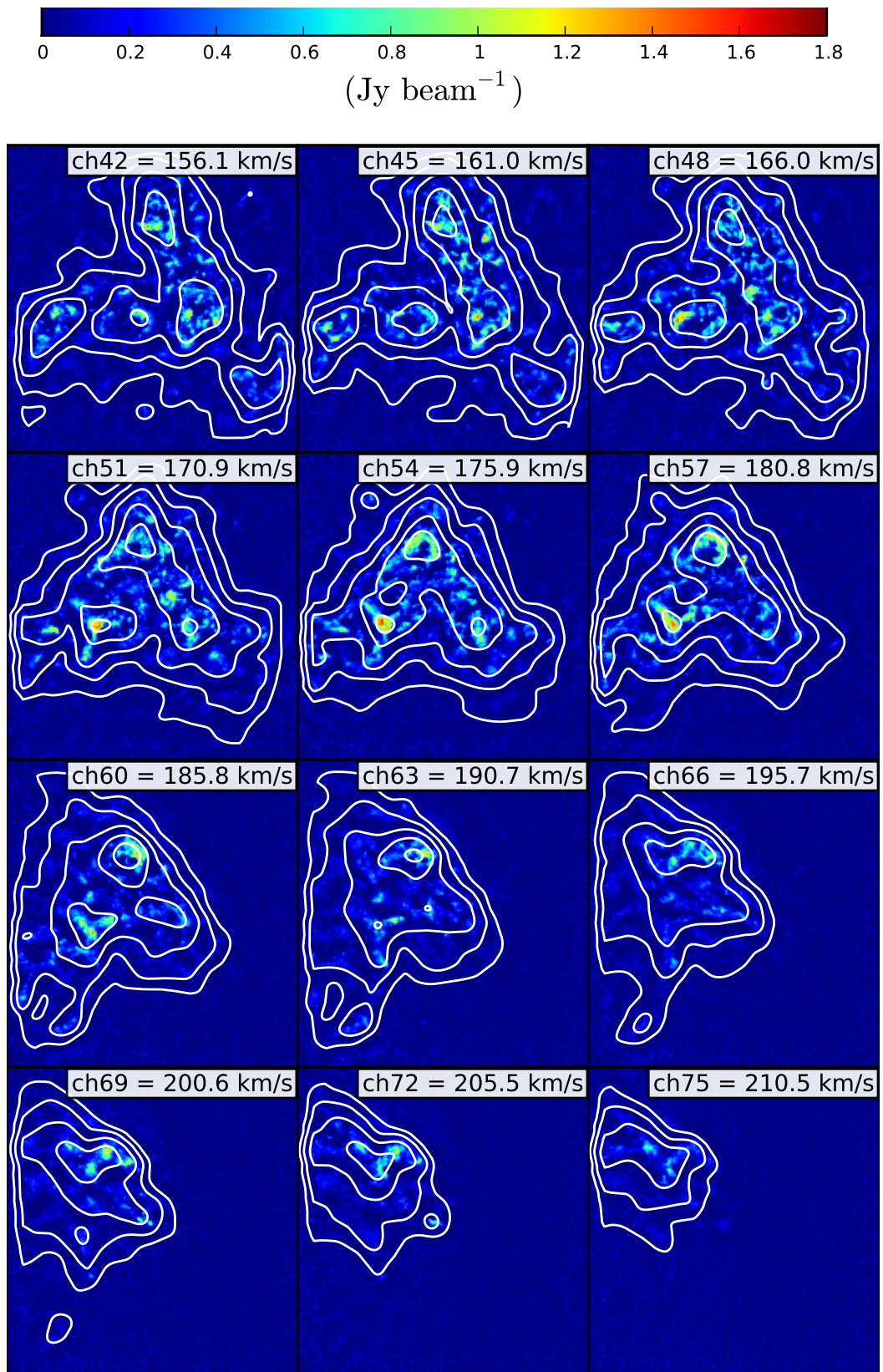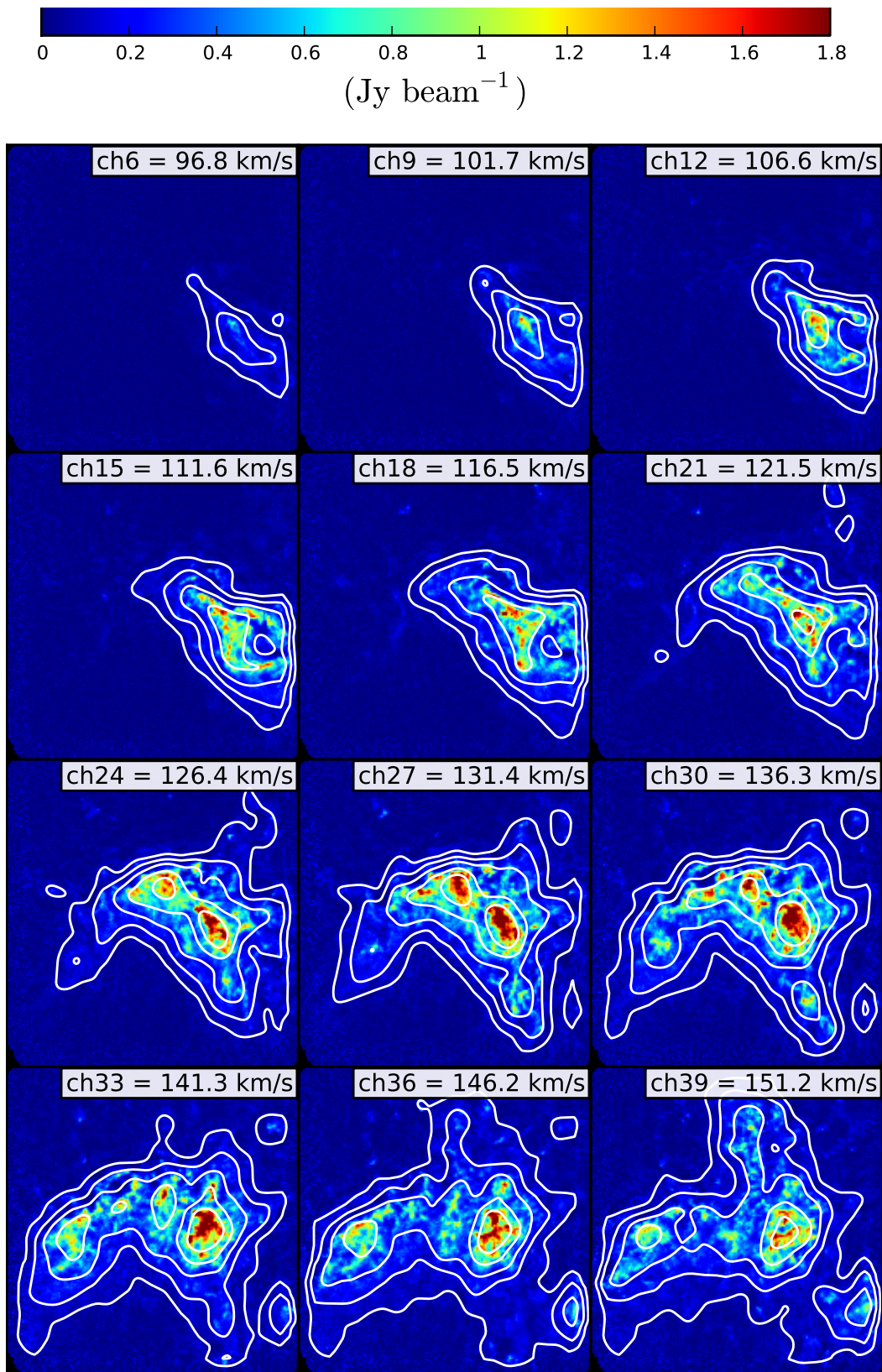
Figure 3.6: continued

Figure 3.7: Multi-channel map of the SMC. The raster image is the combined data set. The overlaid contours are from the Parkes data cube, where contour levels are 10, 20, 40, 80, and 130 Jy beam^{-1}.
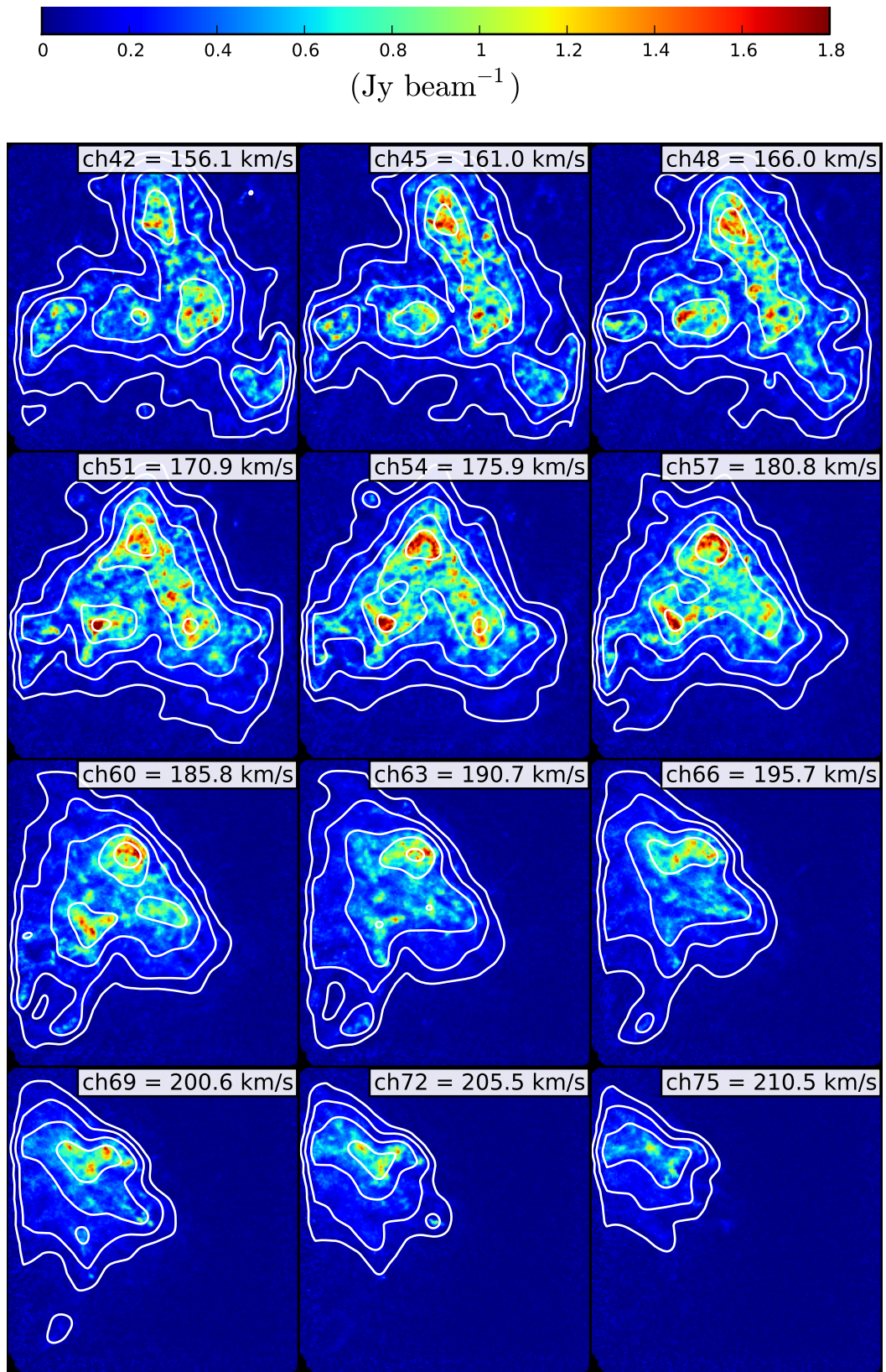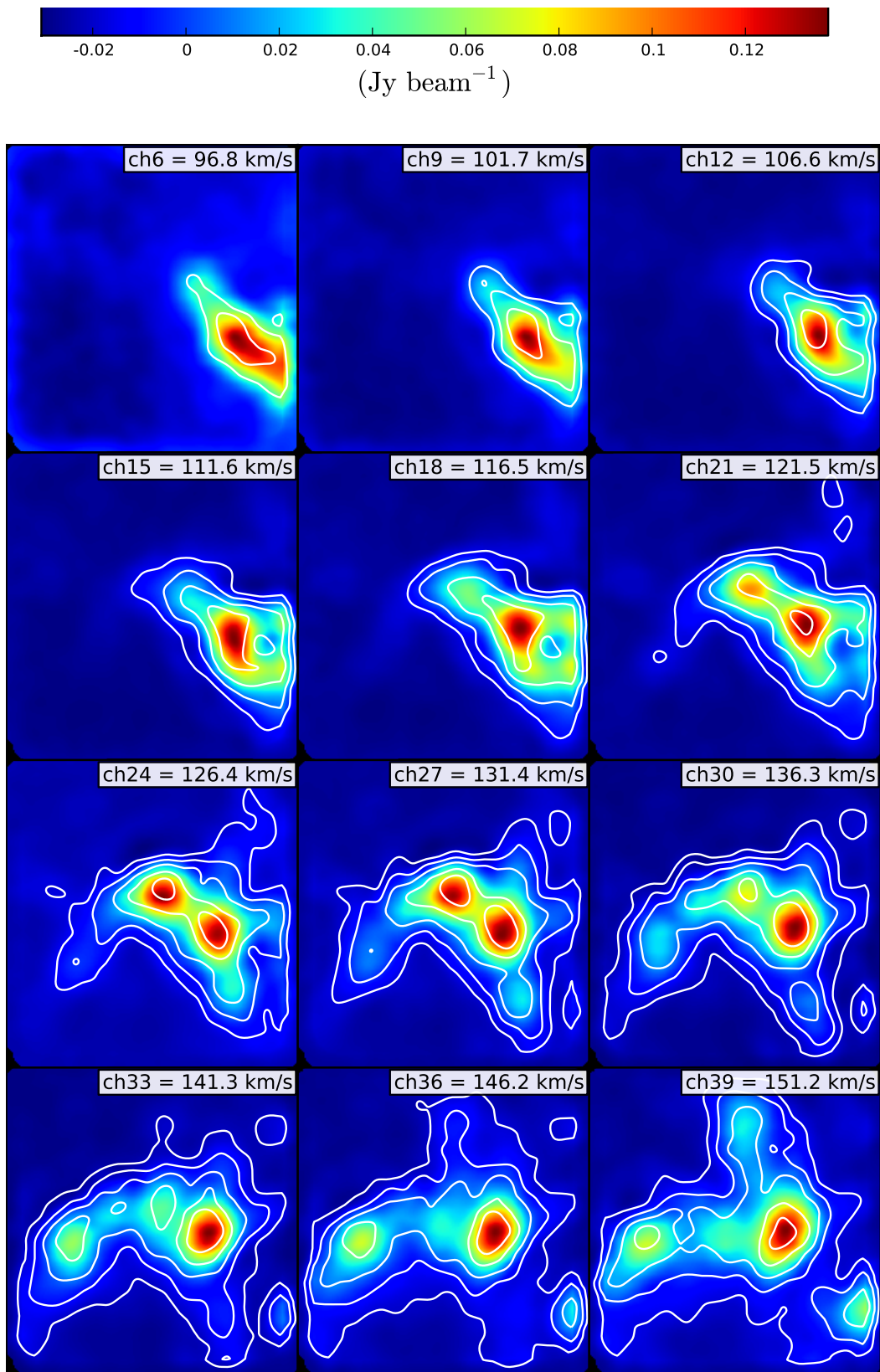
Figure 3.7: continued

Figure 3.8: Multi-channel map of the SMC. It shows the difference between the interferometric (ATCA) and combined data cube for each channel. The overlaid contours are from the single-dish (Parkes) data. The contour levels are as before 10, 20, 40, 80, and 130 Jy beam^{-1}. The difference map contains flux density which is measured only by the single dish.

Figure 3.8: continued

(a) SMC - Parkes_reg

(b) SMC - ATCA

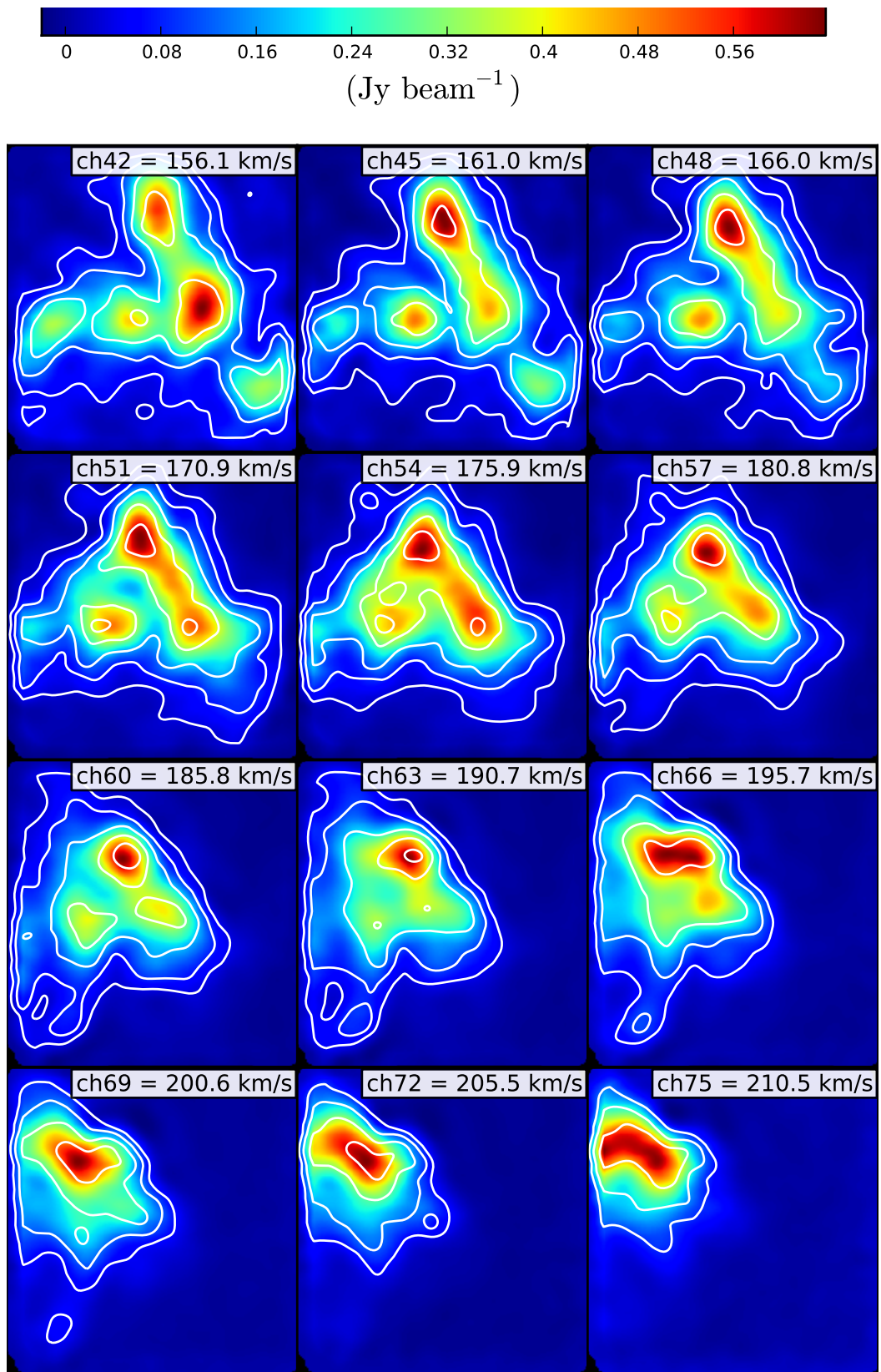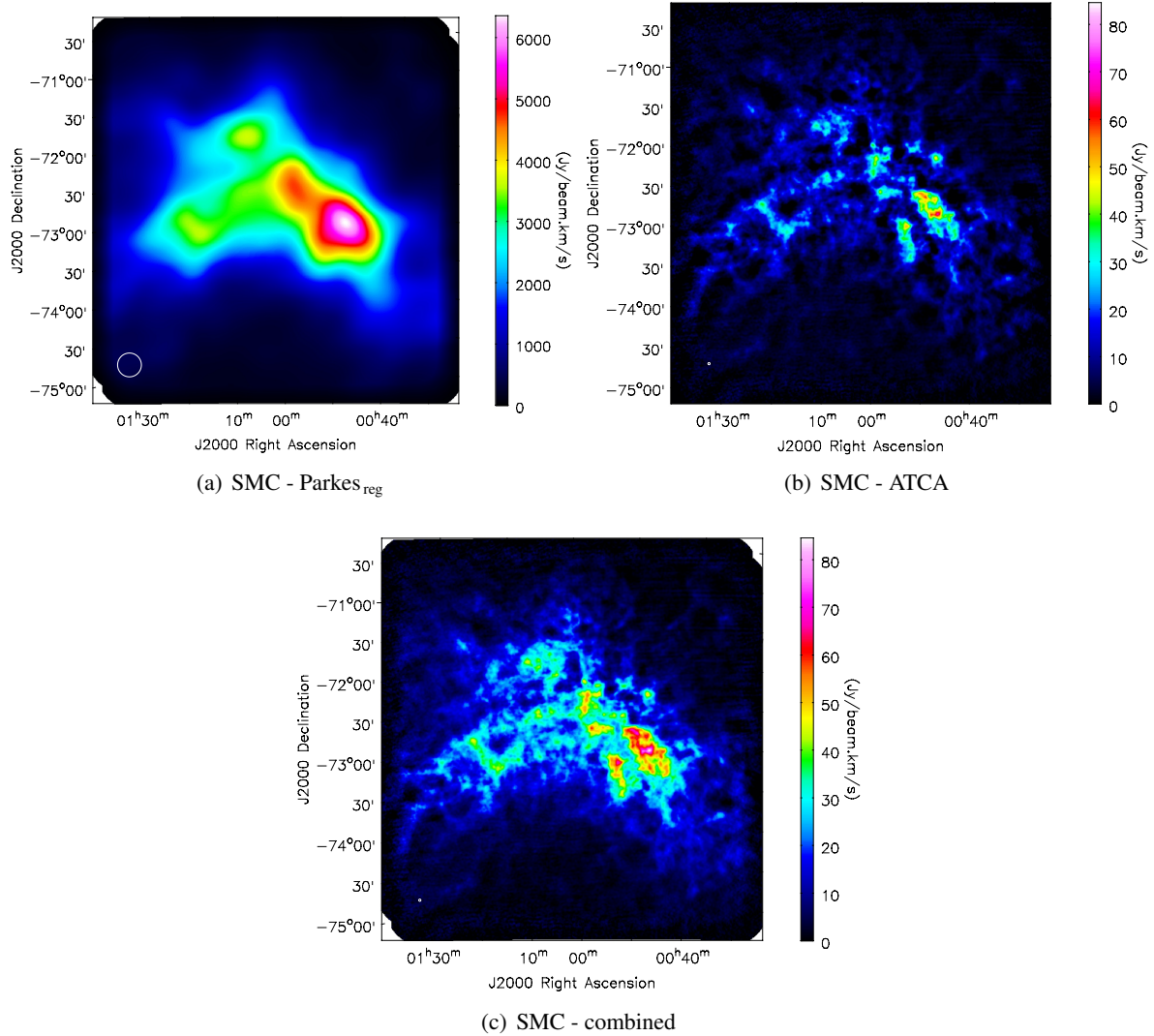(c) SMC - combined

Figure 3.9: The SMC flux density maps without the gridding factor as described in Sec. 3.4.3. Panel (a) shows the regridded flux density map of the Parkes without the gridding factor; panel (b) the flux density map of the ATCA data; and panel(c) the combined flux density map. The difference in measured total flux for the combined and interferometric data cubes is about 43%.

45

Characteristic	SD_{reg}	Int	Comb	Unit
Angular resolution	18.8'	98"	98"	
Spectral resolution		1.65		$[\mathrm{km\,s^{-1}}]$
Angular size of a pixel		30"		
With gridding factor (a):				
H I mass	3.4	1.2	3.4	$[10^8\,\mathrm{M_\odot}]$
Total flux	4.1	1.4	4.1	$[10^5\,\mathrm{Jy\,km\,s^{-1}}]$
F_{Int} / F_{comb}		35%		
Without gridding factor (b):				
H I mass	2.1	1.2	2.1	$[10^8\,\mathrm{M_\odot}]$
Total flux	2.5	1.4	2.5	$[10^5\,\mathrm{Jy\,km\,s^{-1}}]$
F_{Int} / F_{comb}		57%		

Table 3.2: Estimated H I mass for different SMC data sets. For these estimations, the SMC is assumed to be at a distance of 60 kpc. For the H I mass estimation, two different cases are considered: with (a) or without (b) the gridding factor. In both cases the measured total flux in the regridded single-dish data cube is in very good agreement with the corresponding value in the combined data cube. However, due to the gridding factor these values differ strongly. Consequently, the estimated total H I masses are different. The measured H I mass for the first case (a) is in agreement with the value reported by Putman et al. (2003). It is lower than the value listed by Stanimirović (1999). She estimated originally a H I mass of $3.8 \times 10^8\,\mathrm{M_\odot}$. However, after the self-absorption correction, the reported value is $4.2 \times 10^8\,\mathrm{M_\odot}$.

(1999) estimated originally a H I mass of $3.8 \times 10^8\,\mathrm{M_\odot}$. However, after the self-absorption correction, the author reported a value of $4.2 \times 10^8\,\mathrm{M_\odot}$. Bajaja & Loiseau (1982) estimated the H I mass of $5.5 \pm 0.4 \times 10^8\,\mathrm{M_\odot}$ for the SMC. The variations in the estimated H I masses might be due to the different FoV for these data sets.

Figure 3.6 shows the multi-channel maps of the interferometric data sets overlaid with single-dish contours, Fig. 3.7 the multi-channel maps of the combined data sets overlaid with contours from the single-dish cube, respectively. The contour levels in both figures are 10, 20, 40, 80, and 130 Jy beam^{-1}. The plotted channels along the velocity axis vary from 6 to 78 in steps of 3 channels. Furthermore, the difference map between combined and interferometric data has been computed (Fig. 3.8). This data cube contains exclusively flux measured with the single-dish (missing spacings). The overlaid contours have the same levels as described before.

3.4.4 Annuli flux and sum spectrum

Panel (a) of Fig. 3.10 shows the measured cumulative flux as a function of radial separation from the center of the map for the single-dish, interferometric, and combined map for the SMC data. Panel (b) of the same figure shows the sum spectrum for these data sets. In both panels, the blue line presents the measured flux for the combined data cube, the green line the interferometer, and the red line the regridded single-dish data cube, respectively. The measured flux in the combined data cube presented in panel (a) is in good agreement with the measured value from the single-dish data. The difference in the measured total flux between the single-dish and interferometer data cube is about 65%, which suggests strongly that the SMC consists of a considerable amount of warm and diffuse gas.

For the sum spectrum (panel b) the total flux in units of Jy has been measured for each channel independently. The measured value for each channel in the combined data cube is again in good agreement
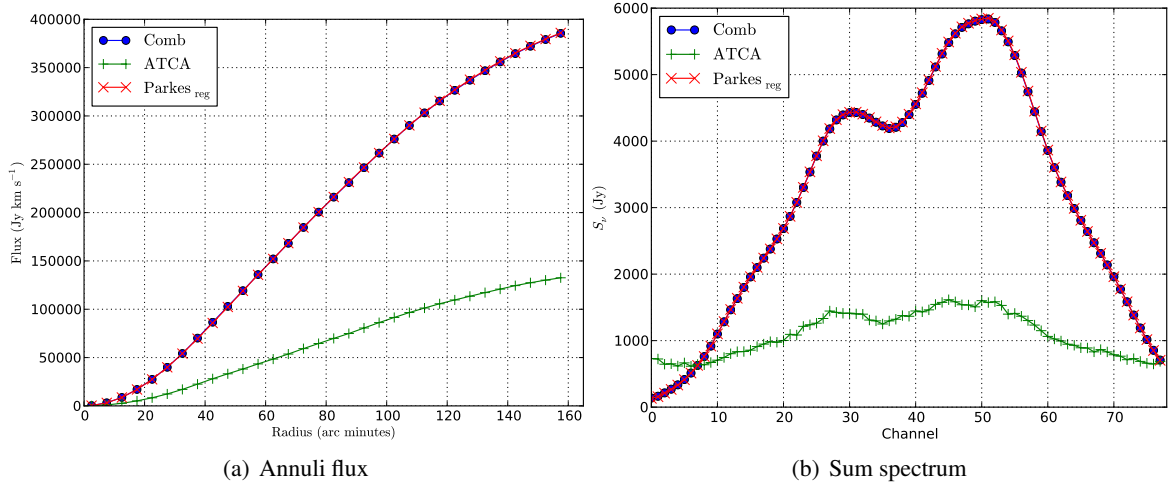
(a) Annuli flux

(b) Sum spectrum

Figure 3.10: Panel (a) presents the measured cumulative flux as a function of radial separation from the center of the map. In both panels, the blue line presents the measured flux for the combined data cube, the green line for the interferometric, and the red line for the regridded single-dish data cube. The measured flux in the combined data cube is in good agreement with the measured value from the single-dish data. The difference in total flux is about 65%, which suggests strongly that the SMC consists of a considerable amount of warm and diffuse gas. Panel (b) shows the sum spectrum for all three data sets, i.e., combined, interferometric, and single-dish. For the sum spectrum the total flux (Jy) has been measured for each channel independently. The measured value for each channel in the combined data cube is again in good agreement with the corresponding value in the regridded single-dish cube. The highest flux value of about 5.84×10^3 Jy is measured in the 51st channel at $172.6 \, \mathrm{km \, s^{-1}}$.

with the corresponding value in the regridded single-dish cube, whereas the measured value in the interferometric data cube is much smaller. The highest flux value is measured in the 51 th. channel with a heliocentric velocity of about $172.6 \, \mathrm{km \, s^{-1}}$. This value accounts for $\approx 5.8 \times 10^3$ Jy.

The measured total fluxes in the first channels (0 to 6) of the sum spectrum for the single-dish and interferometric data sets reveal a strong deviation, where single-dish only measures values around 100 $\mathrm{Jy \, beam^{-1}}$, whereas the interferometer accounts for values about 700 $\mathrm{Jy \, beam^{-1}}$. A closer inspection shows that the difference is because of different noise levels in the interferometric data cube. The nature of the offset could not be concluded. However, the interferometric data cube is a mosaic of a large number of pointings, which have been conducted in different time windows. This could lead to variable systematics and consequently various RMS levels in different parts of the map. Stanimirović (1999) listed two different sorts of artifacts: low-level artifacts and horizontal stripes. The former artifacts are obvious in the northeast regions of the interferometric data cube, whereas the latter are obvious in the southeast regions. Furthermore, the author argued that the low-level artifacts are because of underestimation of line-free velocity ranges, whereas the latter artifacts are the result of solar artifacts (Stanimirović 1999, Fig. 2.3 - channel map at $V_{\mathrm{helio}} \approx 90 \, \mathrm{km \, s^{-1}}$).

Figure 3.11 shows the histograms of the first channel of the interferometric cube. The blue histogram shows the left half of the first channel, whereas the red one shows the right half of the same channel. The shape of both histograms are identical, however, the blue histogram is broader, which suggests higher RMS levels in the left region. Extra emission can also lead to the width of the histogram. Nevertheless, the trend is present in all the velocity channels. The only reason, why it is not very obvious in other channels as shown in the panel (b) of Fig 3.10 is that these channels are strongly dominated by the strong emission from the SMC and therefore, is not significantly obvious in the further channels of the
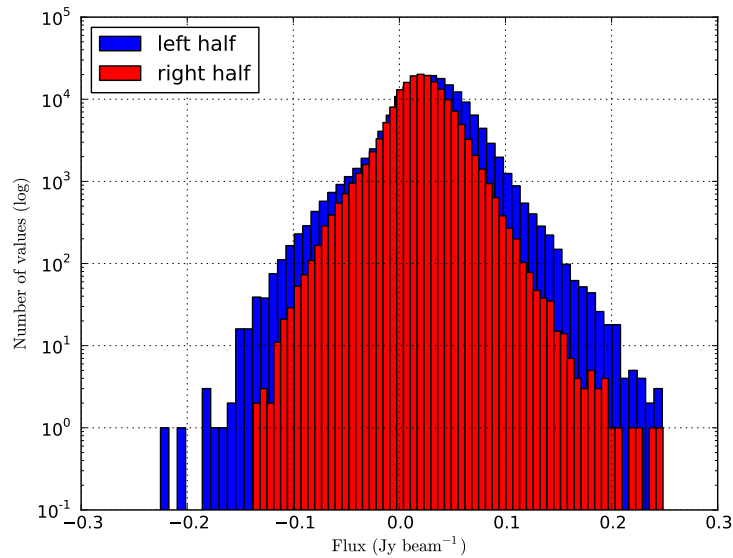
Figure 3.11: The channel of the interferometric data cube is divided into two equivalent halves, where for each half a separate histogram is shown. The broader histogram (blue) corresponds to the left half and the narrower one (red) to the right half. The broadness suggests higher noise level in this region.

calculated sum spectrum.

3.5 Comparison with the previous approaches

The majority of existing approaches for performing the SSC operate in the Fourier (spatial frequency) domain (Sec. 3.2). Among these methods, the most widely used approach for combining the deconvolved interferometric data cube with the single-dish data cube is probably *feathering*. The method uses the Fourier transformation of the single-dish beam to *taper (down weight)* the central regions of the interferometric (u, v) coverage. Furthermore, the single-dish and tapered interferometric data are combined in the spatial frequency domain. Finally, an inverse Fourier transformation is required to obtain the combined image.

Feathering is very sensitive to the edge-effects resulting from strong emission present at the edges of the single-dish data cube. The result of the combination may suffer from artifacts resulting from the Gibbs phenomenon (Sec. 3.2). Therefore, tapering is required. However, tapering can over weight the single-dish data in the spatial overlap region. The higher weighted data can consequently result in higher total flux in the combined data (Stanimirović 1999). In fact, she measured about 10% more flux from the combined SMC using *immerge* form MIRIAD (Stanimirović 1999, Table 3.1). For the method introduced in this thesis, no Fourier transformation is required, since the combination occurs entirely in the image domain. It is an advantage, when dealing with a large amount of data with strong emission over the edges of the map.

Stanimirović (2002) discussed further combination methods: the *linear combination method* (Stanimirović et al. 1999), the *merging during deconvolution*, and the *joint deconvolution* method. In the latter approach the combination is the result of the MEM deconvolution of a dirty interferometric data set with a single-dish data set. The author used the *linear combination method* for merging the ATCA data set with that of the Parkes telescope. This approach adds the missing spacings in the image domain prior to deconvolution of the interferometric image. The following equations describe the $I_{\text{comb}}^{\text{D}}$, the

combined dirty image and B_{comb} the combined beam.

$$I^{\mathrm{D}}_{\mathrm{comb}} = (I^{\mathrm{D}}_{\mathrm{Int}} + \alpha f I^{\mathrm{D}}_{\mathrm{SD}})/(1 + \alpha) \qquad (3.3)$$

$$B_{\mathrm{comb}} = (B_{\mathrm{Int}} + \alpha B_{\mathrm{SD}})/(1 + \alpha). \qquad (3.4)$$

$I^{\mathrm{D}}_{\mathrm{Int}}$ is the interferometric dirty image, $I^{\mathrm{D}}_{\mathrm{SD}}$ that of single dish. B_{Int} is the dirty beam of the interferometer, B_{SD} the beam of the single dish. α is an estimate of the ratio of the beam areas for the single dish and interferometer. For this data set $\alpha = 0.75$. f is the calibration scaling factor measured in the overlap region of the ATCA and Parkes spectral line observations. It is equal to $f = \frac{S_{\mathrm{ATCA}}}{S_{\mathrm{Parkes}}} = 1.05 \pm 0.05$ as described by Stanimirović et al. (1999).

The ATCA and Parkes data cubes as well as the combined cube using the linear combination method have been kindly provided by S. Stanimirović. In the following this data and their overall physical and morphological properties are presented. Furthermore, a comparison between two combined data sets (linear combination used by Stanimirović (1999) and the presented method in this work) is provided.

The original combined data cube as presented by Stanimirović (1999) was in units of Kelvin, which has been converted to Jy beam^{-1}. The corresponding conversion factor is 0.93 K Jy^{-1}. The spectral resolution in the combined data cube is ≈ 1.65 km s^{-1}. The measured total flux in the combined data cube is $\approx 4.5 \times 10^5$ Jy km s^{-1}, whereas the total flux in the regridded single-dish data cube accounts for $\approx 2.5 \times 10^5$ Jy km s^{-1} corresponding to a multiplicative factor of 1.82 in the total flux. The difference can be due to the *gridding correction factor* of 1.63 as described in Sec. 3.4.3. However, the correction factor explains the difference in the total fluxes measured in the single-dish and combined data sets to about 90%. The difference of 10% can be due to a small factor regarding the Parkes calibration (Stanimirović 2013, priv. comm.). For simplicity the method presented by Stanimirović (1999) is labelled as method (a). For the result of combination using the introduced pipeline in Sec. 3.3 the designation method (b) has been used. Table 3.3 summarizes important physical and observational parameters of both data sets.

Both data sets cover the same area. Additionally, the spectral and angular resolutions of both data sets are identical. The pixel size and beam area are the same for both data sets. The total flux measured in the combined data from method (a) is about 10% higher than the corresponding value measured in the combined data set using method (b). Note, that the former value is also approx. 10% higher than the measured total flux in the regridded single-dish data as listed in Table. 3.2. Additionally, the RMS levels have been measured in both data sets using MAD. The measured RMS value in method (a) is about 61 mJy beam^{-1}, whereas the value from method (b) is slightly higher with ≈ 66 mJy beam^{-1}. The positive peak in method (a) is lower than the corresponding value in method (b), whereas the negative peak in (a) is higher than in (b).

Fig. 3.12 shows flux density maps for the combined SMC data using the two combination approaches as described before. Panel (a) shows the total flux density map for the combined data set using method (a) presented by Stanimirović (1999), panel (b) the result of combination for method (b) as introduced pipeline in Sec. 3.3. Both data sets reveal similar morphology in their H I elongation. Panel (c) shows the difference map Comb$_{\mathrm{method\,(a)}}$ - Comb$_{\mathrm{method\,(b)}}$. The total intensity and flux density for both data set is listed in Table 3.3. The measured total flux in the difference map is about $4.6 \cdot 10^4$ Jy km s^{-1}. The difference is also obvious in the sum spectrum for both combined data sets (Fig. 3.13). The result suggests that the difference is probably not due to the combination method but eventually an additional calibration factor as mentioned before. It is obvious that the flux value measured in the data set from method (a) is higher than the value from method (b). For the channels, where the measured flux is not very high, the difference between two data sets is not significant. However, for the channels with higher flux values, in particular from 30 - 55th. channel the difference is large. However, the trend also obvious

Characteristic	Value		Unit
Heliocentric velocity range	$88 \leq V_{\text{helio}} \leq 216$		$[\text{km s}^{-1}]$
Spectral resolution	1.65		$[\text{km s}^{-1}]$
Total covered area	20		$[\text{degrees}^2]$
Pixel size	30"		
Angular resolution	98"		
	Method (a)	Method (b)	
Total intensity	5.5	4.9	$[10^6 \text{ Jy beam}^{-1}]$
Total flux	4.5	4.1	$[10^5 \text{ Jy km s}^{-1}]$
RMS values	61	66	$[\text{mJy beam}^{-1}]$
Min / max value	-0.2 / 2.8	-0.4 / 2.9	$[\text{Jy beam}^{-1}]$

Table 3.3: Method (a) presents the important physical and observation parameters of the combination data cube presented by Stanimirović (1999). Method (b) lists the same characteristics for the combined data using the introduced pipeline in Sec. 3.3. Both data sets have the same FoV. Furthermore, the spectral and angular resolutions of both data sets are identical. The pixel size and beam area are the same for both data sets. The total flux measured in the combined data from method (a) is about 10% higher than the corresponding value measured in the combined data set using method (b). Note, that the former value is also approx. 10% higher than the measured total flux in the regridded single-dish data as listed in Table. 3.2. Additionally, the RMS levels have been measured in both data sets using median absolute deviation (MAD).

in the sum spectrum suggests that the difference is due to a multiplicative factor and not because both methods are differently sensitive towards different components.

3.6 Summary and conclusions

- An automated pipeline has been introduced for performing the SSC. For the evaluation of the pipeline single-dish and interferometric observations of the SMC has been used. The introduced approach combines the *cleaned* interferometric data with that of the single dish in the image domain. Moreover, It does not require additional information such as visibilities or the exact knowledge of the dirty beam.

- For the combination regridding is necessary. Regridding is an interpolation algorithm, which accounts for different projection and geometry in different data sets. For the presented data sets in the current chapter the linear interpolation has been chosen. This is an appropriate interpolation scheme for the combination, since it preserves the amount of total flux in the regridded data set.

- The measured total flux in the combined data cube is in a very good agreement with the measured value in the single-dish data. This is the case for both the measured total flux from the velocity-integrated map as well for each channel in the calculated sum spectrum.

- The results of the current study show that the combination in the image domain is able to fulfill the expectations regarding flux consistency and final angular resolution. Furthermore, the method does not require any Fourier transformation. This is of particular importance for data sets with strong emission at the edges of the map.

(a) SMC: Combined data using method (a)

(b) SMC: Combined data using method (b)

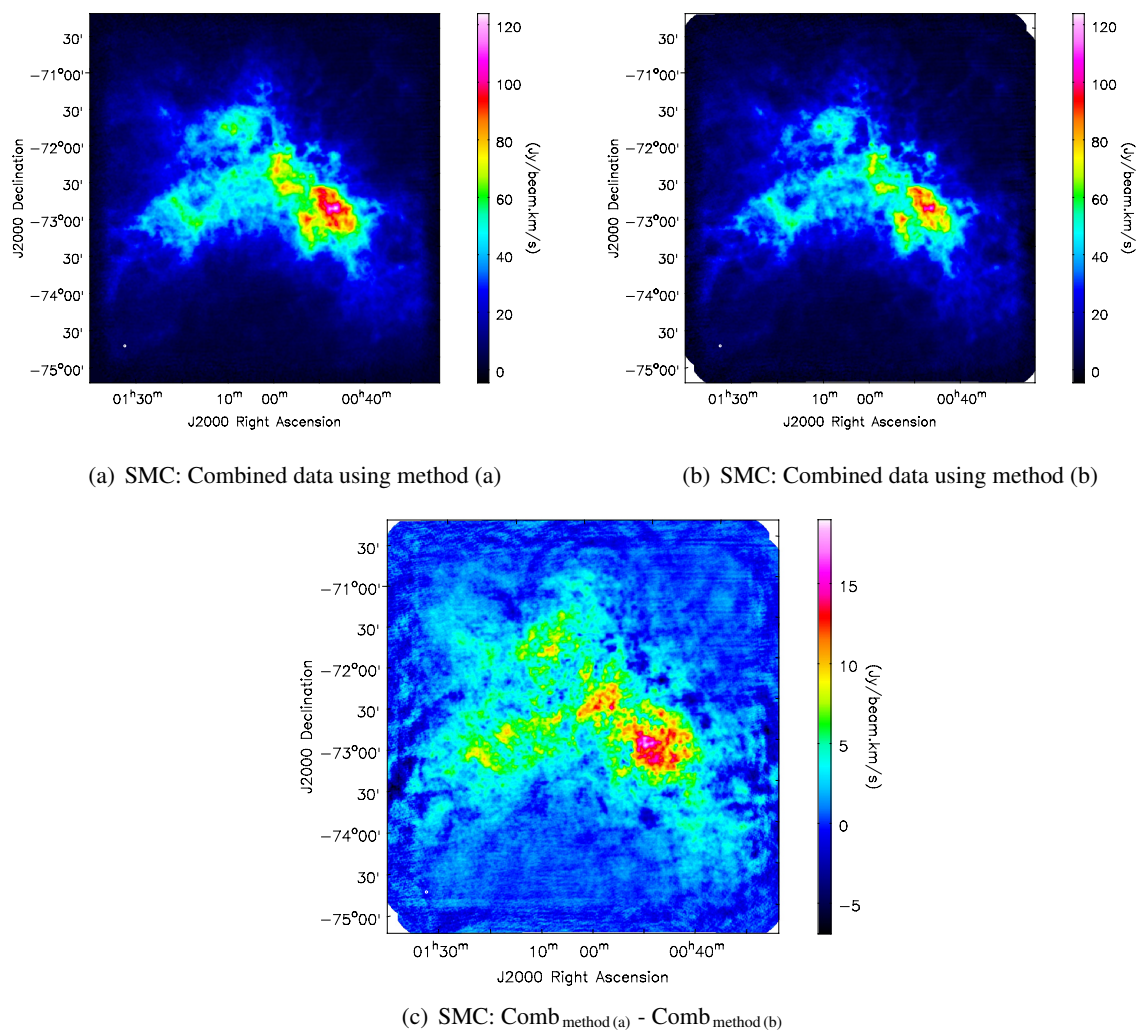(c) SMC: $\mathrm{Comb}_{\mathrm{method\,(a)}}$ - $\mathrm{Comb}_{\mathrm{method\,(b)}}$

Figure 3.12: Flux density maps for the combined SMC data using different combination approaches. Panel (a) shows the total flux density map for the combined data set using method (a) presented by Stanimirović (1999), panel (b) shows the result of combination for method (b) as introduced in Sec. 3.3. The color maps for both data sets are indentical. Both data sets reveal similar morphology in their H I distribution. Panel (c) shows the difference map $\mathrm{Comb}_{\mathrm{method\,(a)}}$ - $\mathrm{Comb}_{\mathrm{method\,(b)}}$. Note that the flux scale in panel (c) has been enhanced.
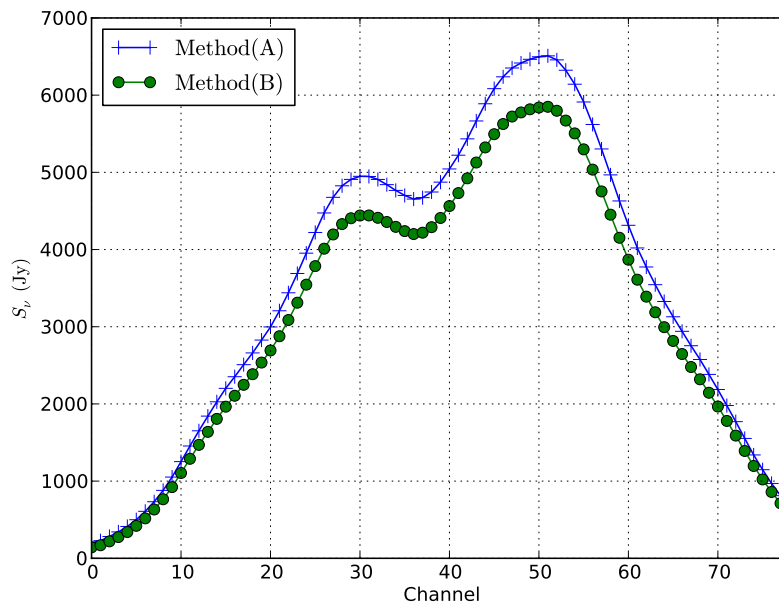
Figure 3.13: Sum spectrum of combined data sets. Method (a) presents the sum spectrum for the combination conducted by Stanimirović (1999). Method (b) the combined data set using the introduced pipeline in this thesis. It is obvious that the flux value measured in the data set from method (a) is higher than the value from method (b). For the channels where the measured flux is not very high, the difference between two data sets is not significant. For channels with higher flux values, in particular from the 30 - 55th channels, the difference is large. The apparent trend in the sum spectrum suggests that the difference is due to a multiplicative constant and not because both methods are differently sensitive towards different components.

- The results emphasize the importance of SSC for a detailed understanding of the ISM for the Galactic objects. The correction is also important for the estimation of the total neutral gas mass. The large difference in the measured total flux in the interferometric and combined maps suggests that the interferometer underestimates the total H I mass of the SMC by about 65%.

Study of short-spacing correction for a sample of three nearby galaxies

4.1 Introduction

A smaller ensemble of The H ɪ Nearby Galaxy Survey (THINGS, Walter et al. 2008) galaxies (29 galaxies) has been observed subsequently with the 100 m Effelsberg telescope. Ten of these galaxies are blended with the strong Milky Way emission. The rest is well separated from the Galactic emission (Kerp et al., in prep.).

   The study to be presented in this chapter concerns the short-spacing correction (SSC) for three nearby galaxies: NGC 4214, NGC 5055, and NGC 2403. It is therefore, complementary to the presented studies for the Galactic objects (Chap 3 and Chap. 5). The reason for this selection is that the galaxies are located in different distances. Additionally, they have substantial differences in their morphology, extension, and physical parameters. In particular, they differ in the amount of faint diffuse gas present in and around the galaxy.

   The current chapter is organized as follows. The first part gives an understanding of the effect of Galactic emission on the SSC data. The second part is devoted to the systematical study of the impacts of interferometric imaging parameters on the SSC data. The last part, presents the result of SSC for different interferometric arrays. Finally, a conclusion is presented.

4.2 Study of the effect of Galactic emission on the SSC data

In the current section the effect of Galactic emission on the result of the combined data is presented using NGC 2403 as a case study. The strong Galactic emission stemming from the Milky Way has been the subject of many different studies. However, this emission can also be of significant importance for a number of nearby galaxies, if the galaxy is not well separated from the Galactic emission. This can cause systematics in the single-dish observations of such objects. Subtracting the Milky Way emission is not an easy task and requires a complicated and accurate numerical model (e.g., Kalberla & Dedes 2008). The interferometric observations of these galaxies are less sensitive towards the Milky Way emission, since the gas is mainly warm and diffuse. Regarding contamination with the Milky Way emission, the antenna pattern of the single-dish telescope also plays a significant role. For low Galactic latitudes, it is possible that considerable amounts of the Milky Way emission propagates into the single-dish

Characteristic	Value
Object name	NGC 2403
Object type	Sc spiral galaxy
RA / DEC	07h36m51.4s / +65d36m09s
V_{sys}	133 km s^{-1}
Total H I mass	3.2 10^9 M$_\odot$

Table 4.1: Characteristics of NGC 2403

observation via the side lobes of the antenna pattern (Verschuur & Kellermann 1988). In the following, it is shown how the systematics propagate into the SSC data. Furthermore, it is tried to quantify the impacts of the Galactic emission on both physical and kinematical properties of the combined data (Sec. 4.2).

4.2.1 NGC 2403

NGC 2403 is a nearby Sc spiral galaxy similar to M33 with an inclination angle of 60°. It is located at a distance of 3.18 Mpc (Fraternali et al. 2004, and references therein). Fraternali et al. (2002) estimated a total H I mass of about 3.2×10^9 M$_\odot$ for this galaxy. The dynamics of the galaxy has also been the subject of several studies. Fraternali et al. (2002) studied the gas inflow in outer and surrounding regions of the H I disk. A detailed study of the galaxy has been done by den Heijer (2014, priv. comm.) in the framework of his Ph.D thesis. This author puts the emphasis on the kinematical aspect and deals with the impacts of strong Galactic emission on the kinematics of the combined data and shows that large errors are present in the SSC data set. The current thesis investigates the effect of Milky Way emission on the flux values measured in the combined cube as well as the morphology in the corresponding data set. Table 4.1 lists the most important characteristics of NGC 2403.

Figure 4.1 shows the optical map of NGC 2403 obtained from the ESO online Digitized Sky Survey (DSS) overlaid with H I map observed with the Very Large Array (VLA). The contours show 1-, 2-, 3-, 6-, 10-, 20-, 50-, and 100-σ levels measured in the interferometric data cube. The image reveals the extended H I disk compared to the optical disk.

4.2.2 Observations and data

The single-dish observation of NGC 2403 was carried out with the 100 m Effelsberg telescope as part of Effelsberg-Bonn H I Survey (EBHIS, Kerp et al. 2011) observations. The angular resolution of the Effelsberg data is $\approx 10.8'$. The spectral resolution of this data set is about 1.28 km s^{-1} with 253 spectral channels. The interferometric observation of the object has been carried out with the VLA telescope in the framework of THINGS observations (Sec. 2.2). The angular resolution of the interferometric observation is $\approx 9'' \times 8''$. The spectral resolution of the interferometric data cube is about 5.1 km s^{-1} over 61 spectral channels. The radial velocity range of NGC 2403 is from approximately $-25 \leq V_{sys} \leq 280$ km s^{-1}. For this object, the single-dish observation reveals very strong Milky Way emission in particular from approximately $-20 \leq V_{sys} \leq +20$ km s^{-1}. Figure 4.2 shows the multi-channel map of this observation. It is obvious that the galaxy is blended with the Galactic emission in particular, in a radial velocity range of $\approx -25 \leq V_{sys} \leq 30$ km s^{-1}. Note that the structures from the Milky Way in particular apparent in channels in neighborhood of 0 km s^{-1} are much larger than the extent of the galaxy. This will cause a shift in the peak of the velocity towards 0 km s^{-1}. It is also the reason why the
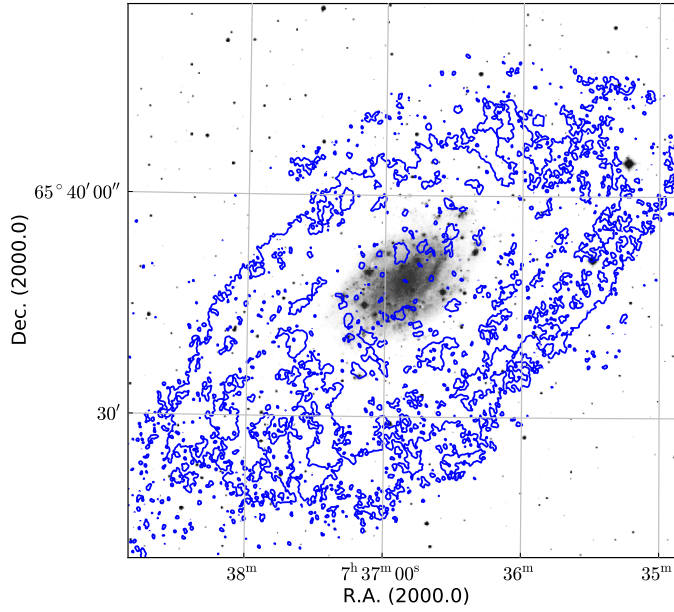
Figure 4.1: DSS optical map of NGC 2403 overlaid with the corresponding H I map observed with the VLA. The contours show 1-, 2-, 3-, 6-, 10-, 20-, 50-, and 100-σ levels measured in the interferometric data cube. It shows an extended H I disk compared to the optical disk.

interferometric observation of the galaxy is not affected significantly by the strong Galactic emission.

The low- and high-resolution data sets of NGC 2403 are the inputs of the combination pipeline as described previously in Sec. 3.3. The angular and spectral resolution of the combined data are identical to the corresponding values in the interferometric data. Additionally, velocity-integrated maps of the regridded single-dish, the interferometer, and the combination are created to measure the total flux density in each data set. In order to estimate the root mean square (RMS) levels in three data sets median absolute deviation (MAD) has been used (App. B). The estimated RMS value in the original Effelsberg data cube is about 85 mJy beam^{-1}. The measured RMS value in the combined data is about 1 mJy beam^{-1}. Table 4.2 summarizes the physical and observational parameters for all three data sets of NGC 2403.

Characteristic	SD$_{reg}$	Int	Comb	Unit
Spectral resolution		5.1		[km s^{-1}]
Angular size of a pixel		3.4"		
Angular resolution	10.8'	9"	9"	
Beam area	119368	20	20	
Total flux	$2.4 \cdot 10^3$	$7.8 \cdot 10^2$	$2.4 \cdot 10^3$	[Jy km s^{-1}]

Table 4.2: Physical properties as well as observational details of the regridded single-dish, the interferometric, and the combined data cube for NGC 2403. The angular resolution of the VLA data cube is much higher than that of the Effelsberg data cube and the former resolution is preserved in the combined data. The amount of measured total flux in the combined data is in very good agreement with the measured value in the regridded single-dish data. The ratio of the total flux measured in the interferometer data is only about 30% of the measured value in the combined data. However, the total flux measured in the combined cube is biased due to the strong Galactic emission propagated from the single-dish observation and therefore, can not be trusted.
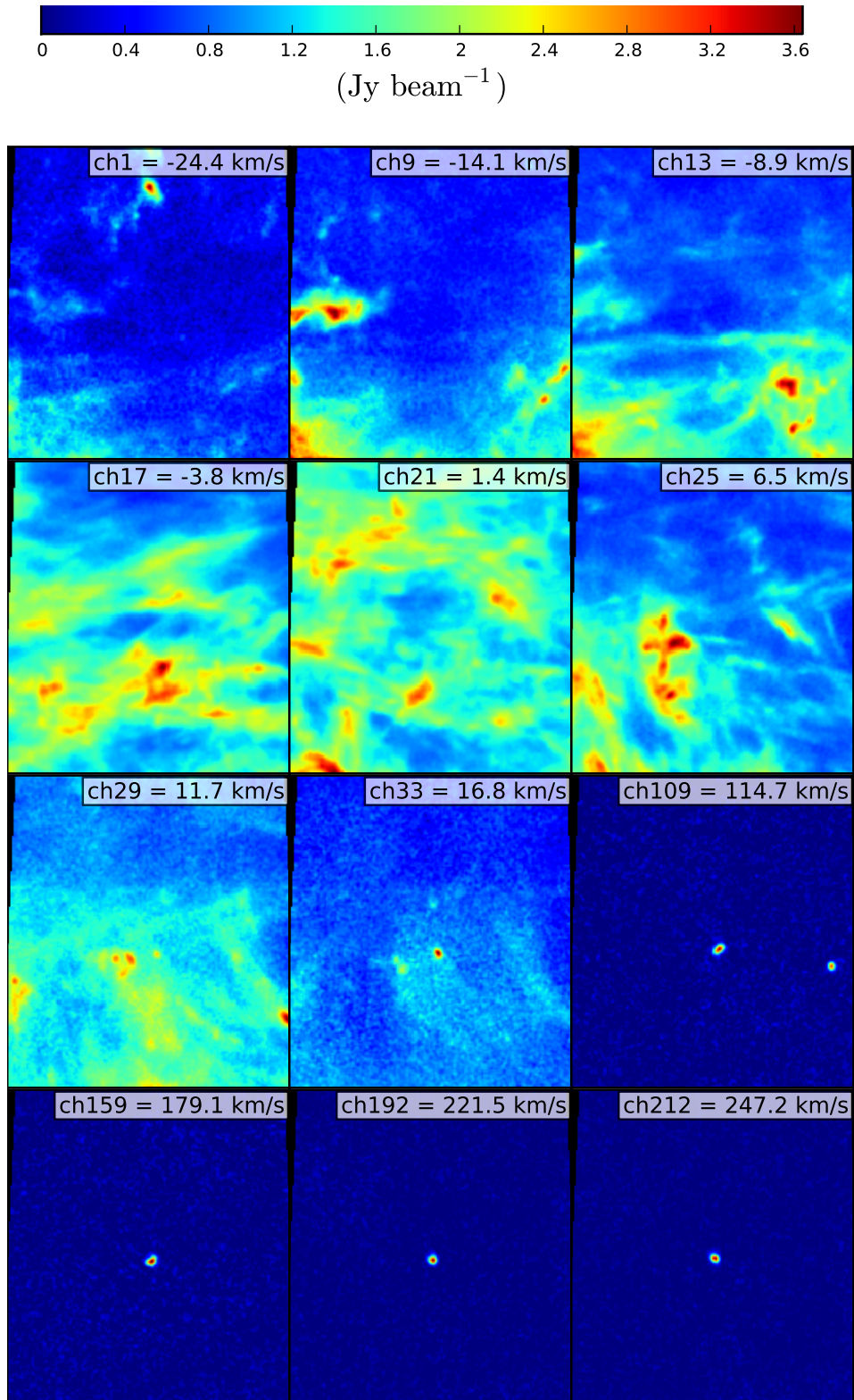
Figure 4.2: Multi-channel map of the Effelsberg's observation of NGC 2403. The velocity extent of the galaxy is roughly $-20 \leq V_{sys} \leq 280 \, \mathrm{km \, s^{-1}}$. Therefore, the galaxy's emission is blended in the strong Milky Way emission. The strong Galactic emission is dominant within channels with lower radial velocities. It decreases significantly in the higher radial velocities away from $0 \, \mathrm{km \, s^{-1}}$, where the galaxy can be identified clearly. The Galactic emission has significant impacts on the result of the combination regarding the total flux. It also affects the kinematical analysis for the combined data set.

4.2.3 Results

The effects of Milky Way contamination on the SSC data set are of importance for the analysis of two quantities: firstly, the velocity distribution, and secondly, the measured flux density.

- **Velocity distribution of NGC 2403:** Figure 4.3 shows the velocity distribution maps of NGC 2403 for the interferometric (panel a) and combined map (panel b) as well as for the combined map without the channels containing the bulk of the Galactic emission (panel c). For the latter map the first 30 km s^{-1} have been omitted. The first-moment map of the interferometric data set corresponds to that of a flat rotating disk. However, the velocity distribution of the combined map shows strong evidence for abnormality. The rotation characteristic has been dramatically altered. The reason for the distortion of the velocity distribution in the combined map is the Galactic emission, which has a certain intrinsic velocity structure.

- **Total flux density in the interferometric and combined data:** Figure 4.4 shows the result of the combination for the NGC 2403. Panel (a) shows the interferometric data, panel (b) the combined data, respectively. Panel (c) presents the sum spectrum for both interferometric and combined data sets in units of Jy. The strong Galactic emission is strongly obvious in the combined data set, whereas the interferometer is insensitive towards this component, since the origin of the emission is mainly warm and diffuse Galactic gas.

  The sum spectrum also reveals the domination of the Galactic emission in the combined data cube, in particular, in the first 5 to 6 channels, corresponding to a radial velocity range of $\approx$ 25 to 30 km s^{-1} considering the spectral resolution of $\approx$ 5.1 km s^{-1}. The Galactic emission decreases for higher radial velocities away from 0 km s^{-1}. The result of the combination can only be trusted in the channels where the strong Galactic emission is entirely absent. However, it is impossible to ensure if no Milky Way emission is present in spectral channels with higher radial velocities. In any case, it is impossible to get an accurate estimate for the total flux density from any of these three data cubes.

4.3 The effects of interferometric imaging parameters on the SSC data

This section introduces two synthesis imaging parameters: weighting schemes and pixel size. Furthermore, the impact of the two parameters on the interferometric and SSC data are discussed. The focus of this study is to demonstrate how important the choice of interferometric data is for the best possible result of the combination. For this purpose, different data sets for NGC 4214 and NGC 5055 are analyzed.

4.3.1 Imaging parameters

Interferometers do not measure the intensity distribution of an object directly. They measure samples of the true intensity distribution of the object in the spatial frequency domain at discrete locations defined by the configuration of the array. The relationship between the visibility and the brightness distribution for an interferometer as well as the principle of interferometric imaging have been described in Chap. 2. Each data point on the (u, v) coverage corresponds to a baseline vector. For a given interferometer different baselines exist. The projected baseline length varies depending on the configuration of the interferometric array and the hour angle of the source. Each baseline is sensitive to different spatial

(a) NGC 2403 - Interferometer

(b) NGC 2403 - Combined
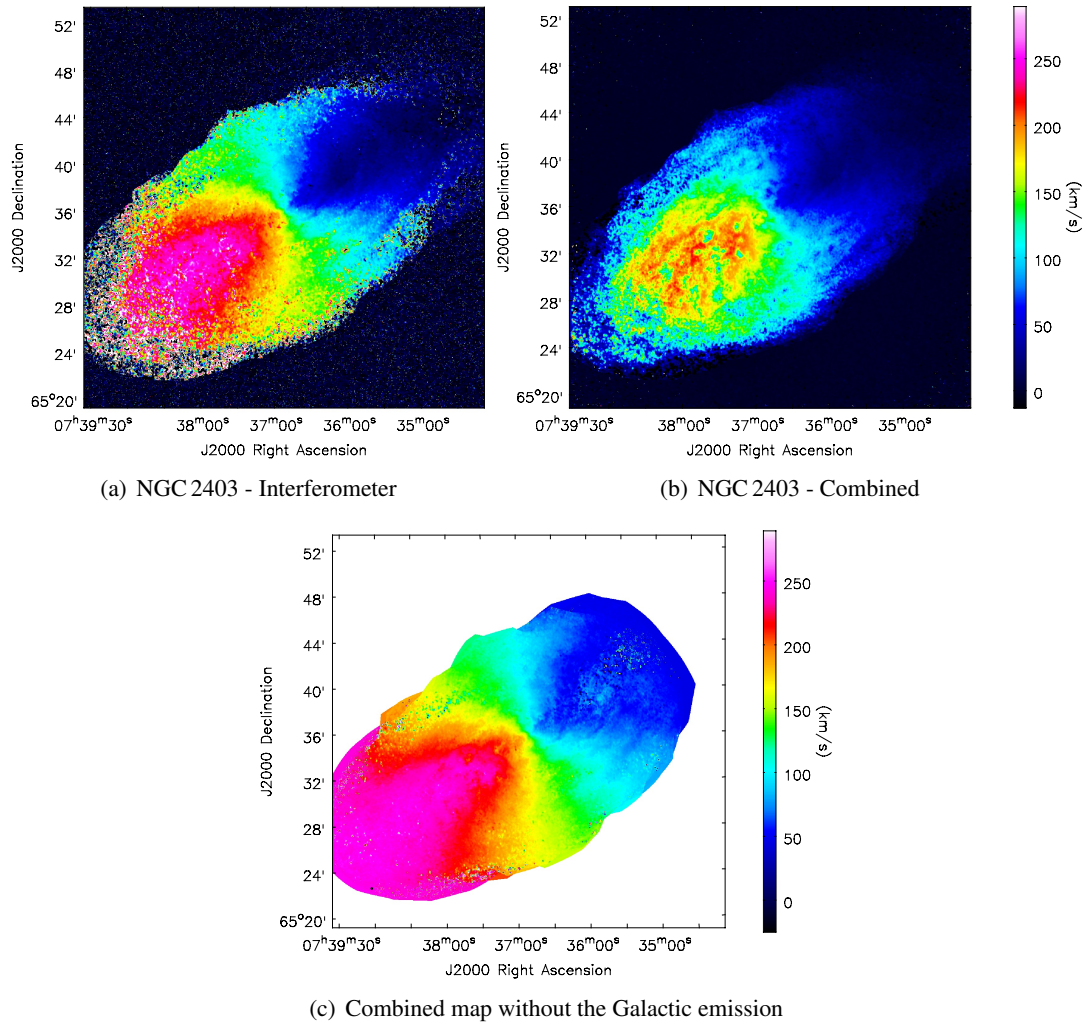

(c) Combined map without the Galactic emission

Figure 4.3: Velocity distribution maps of NGC 2403. Panel (a) shows the velocity distribution for the interferometric data set, panel (b) for the combined map, and panel (c) for the combined map with radial velocity interval from approximately $30 \leq V_{sys} \leq 280 \, \text{km s}^{-1}$, where the channels with strong Galactic emission have been left out.
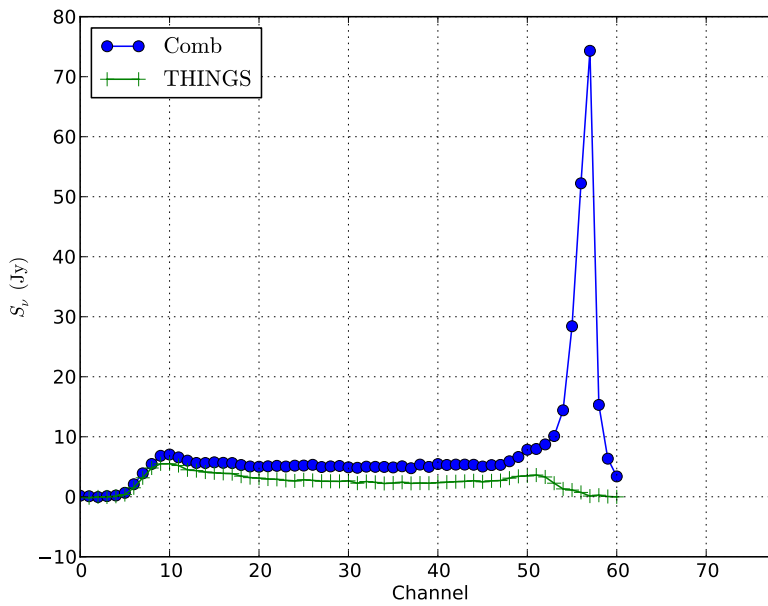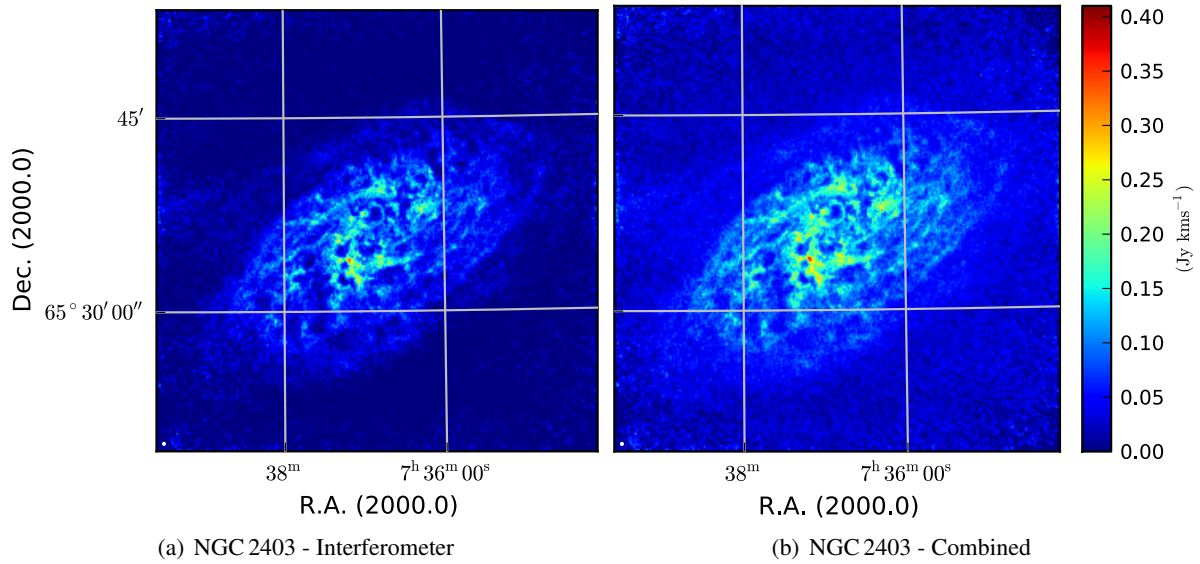
(a) NGC 2403 - Interferometer

(b) NGC 2403 - Combined

(c) NGC 2403 - Sum spectrum

Figure 4.4: Panel (a) shows the flux density map of the interferometric data, panel (b) for the combined data. Panel (c) shows the sum spectra for the interferometer and the combined map. Note the strong Galactic emission obvious in the first velocity channels of the combined data cube. This strong emission dominates the velocity-integrated map of the combined data cube.

scales and therefore, different gas components of an object. The long baselines are sensitive towards small angular scale structures, whereas the short baselines are sensitive towards large angular scale structures.

- **Weighting schemes:** For a given interferometer the density of the sampling points on the (u, v) coverage varies. The density in the central regions is usually higher than in the outer regions of the (u, v) coverage. Weighting schemes have been introduced in order to achieve the desired sampling density for a given (u, v) coverage (Briggs 1995). Each weighting scheme emphasizes different regions in the (u, v) coverage. Depending on how the weights are set, either small or large angular scale structures are emphasized in the final image. The RMS noise values also vary in the interferometric image depending on the applied scheme. The latter parameter will be discussed in detail in Sec. 4.3.3. To illustrate the concept of weighting schemes in the imaging process, Eq. 2.8 can be modified as follows:

$$
\begin{aligned}
\mathfrak{F}^{-1}(V^{\text{obs}}(u, v)) &= \mathfrak{F}^{-1}(V^{\text{true}}(u, v) \cdot S_v(u, v) \cdot W(u, v)) \\
I^D(\xi, \eta) &= \mathfrak{F}^{-1}(V^{\text{true}}(u, v) \cdot S_v(u, v) \cdot W(u, v)) \\
I^D(\xi, \eta) &= \mathfrak{F}^{-1}(V^{\text{true}}(u, v)) * \mathfrak{F}^{-1}(S_v(u, v)) * \mathfrak{F}^{-1}(W(u, v)),
\end{aligned}
\tag{4.1}
$$

where $V^{\text{true}}(u, v)$ is the true visibility, $S_v(u, v)$ the sampling function, and $W(u, v)$ the weighting scheme. $I^D(\xi, \eta)$ is the dirty image.

The weighting scheme $W(u, v)$ can have strong impact on the final result of the dirty image $I^D(\xi, \eta)$. Through multiplication of $S_v(u, v)$ by the weighting scheme, the dirty beam and clean beam change. Furthermore, depending on the weighting scheme the sensitivity and peak values change. This again affects directly the result of the cleaned image.

In general, one distinguishes between *natural* and *uniform* weighting[1]. The natural scheme yields the same weighting for all visibilities. The natural weighting results in a better sensitivity compared to the uniform weighting. For the uniform scheme, the weights are inversely proportional to the density of the sampling function. This leads to a higher noise level in the final map (Teuben 2012). However, uniform weighting yields a better resolution compared to natural weighting.

Briggs (1995) introduced a modification for the existing weighting schemes, *robust* weighting. The scheme uses a *robustness factor* to compromise between the natural and uniform weighting. The effect of different weighting schemes on the result of the interferometric image and the SSC data is introduced in Sec. 4.3.4. Figure 4.5 demonstrates the effect of natural and uniform weighting schemes on the (u, v) coverage as described before.

- **Pixel size:** Prior to the Fourier transformation, the visibilities need to be brought onto a regular grid. For this aim, the raw data is convolved with an specific kernel, the *gridding* kernel, where a pixel size is set. Depending on the pixel size, the data is over or under sampled. Under sampling should be avoided. If the data is not fully sampled (Nyquist theorem is not fulfilled), it can result in lost data (Sec. 2.1.2). Oversampling also affects the data: then data points become increasingly dependent, making structures appear more coherent than they actually are. Additionally, oversampling is computationally expensive, since more data points exist.

---

[1] There also exist super- and sub-uniform weighting schemes. These schemes are modification of the uniform scheme (Teuben 2012).

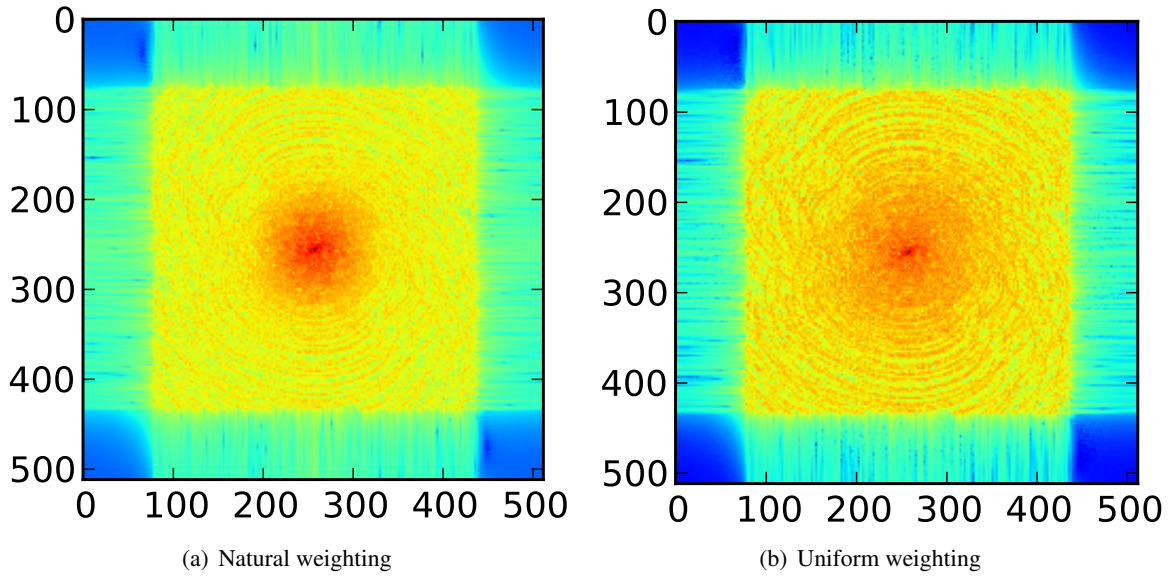(a) Natural weighting   (b) Uniform weighting

Figure 4.5: Effect of different weighting schemes. Both panels show the result of Fast Fourier Transformation (FFT) of two interferometric data cubes with different weighting schemes (2D power spectrum). Panel (a) shows the gridded (u, v) coverage for natural weighting, panel (b) for uniform weighting. The former scheme emphasizes regions of higher sampling density and therefore, is more sensitive towards large angular scale structures in an object. The latter scheme puts the stress on regions of lower sampling density and therefore, is more sensitive towards small angular scale structures. Note that the the RMS noise values in both data sets are very different. This is higher in the uniform weighted data (Sec. 4.3.4).

4.3.2 NGC 4214 and NGC 5055

- NGC 4214 is a Magellanic starburst dwarf irregular galaxy (Sollima et al. 2013; Andrews et al. 2013; Hermelo et al. 2012) with an extended H I halo (McIntyre 1998) with significant spiral pattern. Various observations performed in different wavelengths present evidence for the existence of intense star formation in the center of the galaxy (e.g., Hermelo et al. 2012). The H I emission of the galaxy is observed in the radial velocities between $\approx 270 \leq V_{sys} \leq 360$ km s^{-1} (Walter et al. 2008).

- NGC 5055 is a moderately inclined Sbc galaxy with a large pronounced warp of the extended gaseous disk (Battaglia et al. 2006). Patterson et al. (2012) detected faint H I in the outskirts of the galaxy in the Hydrogen Accretion in LOcal GAlaxieS (HALOGAS, Heald et al. 2011) observation of the NGC 5055 and reported an extent of ≈ 48 kpc for the gaseous disk. The galaxy is also part of the THINGS H I observations of a number of nearby galaxies. Both surveys have been introduced in Sec. 2.2.

  The radial velocity range of the galaxy is about $245 \leq V_{sys} \leq 660$ km s^{-1} (Walter et al. 2008). The HALOGAS and VLA observations of the galaxy have been combined with its Effelsberg observation. The results of the combination are discussed in detail in Sec. 4.5.

  Table 4.3 presents the observational parameters of these two galaxies. Figure 4.6 shows the DSS optical maps of NGC 4214 and NGC 5055. The overlaid contours are from the VLA observations of both galaxies. The contours show 1-, 2-, 3-, 6-, 10-, 20-, 50-, and 100-σ levels. For both of these galaxies the H I disk is much more extended than the optical one.

Characteristic	NGC 4214	NGC 5055
Object type	dwarf irregular galaxy	Sbc galaxy
RA/Dec	12h15m39.2s / +36d19m37s	13h15m49.3s / +42d01m45s
V_{sys}	291 [km s^{-1}]	484 [km s^{-1}]

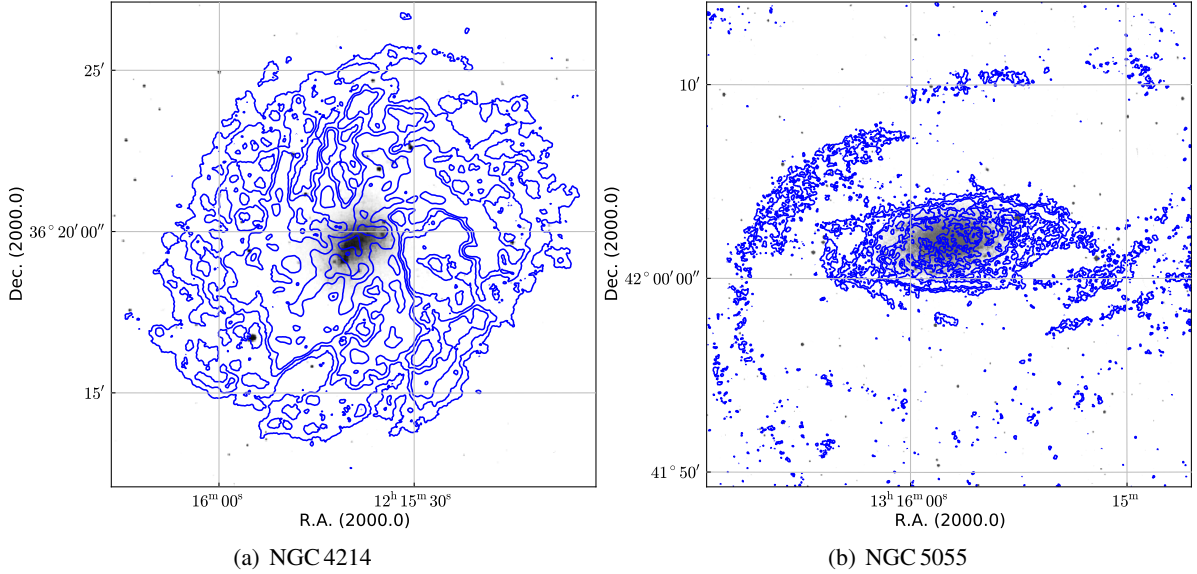Table 4.3: Characteristics of NGC 4214 and NGC 5055.

(a) NGC 4214   (b) NGC 5055

Figure 4.6: Optical maps of NGC 4214 and NGC 5055 overlaid with the corresponding H I map observed with the VLA. The contours show 1-, 2-, 3-, 6-, 10-, 20-, 50-, and 100-σ levels measured in the interferometric data cube. The images reveal an extended H I disk in comparison with the optical disk.

4.3.3 Observations and data

The current section presents the overall properties of the interferometric and single-dish observations of NGC 4214 and NGC 5055. Both galaxies have been observed with the 100 m Effelsberg telescope in the framework of EBHIS. Both data sets have an angular resolution of 10.8'. The spectral resolution is about 1.28 km s^{-1}. The RMS noise level in the EBHIS data cube of NGC 4214 and NGC 5055 is about 60 km s^{-1}.

In the case of NGC 5055, additional single-dish data has been provided by Winkel (2013, priv. comm.). This data set is reduced with the basked weaving technique as described by Winkel et al. (2012a). The technique serves to improve the baseline solutions in the single-dish observations. The basket-weaving data set consists of 10 coverages each with an integration time of 360 seconds per beam (Heald 2011, priv. comm.). For the presented basket-weaving data cube the integration time has been chosen such that the RMS value in this data set is comparable with the corresponding value measured in the short baselines of the HALOGAS observation of the galaxy. As a result of longer integration time as well as the nature of the technique the measured RMS noise level in the basket-weaving cube is about 18 mJy beam^{-1}, which is lower than the corresponding value in the EBHIS data cube. Table 4.4 lists the observational parameters of different Effelsberg observations for the NGC 4214 and NGC 5055.

For the study of the effect of the imaging parameters on the interferometric and the SSC data a large

Characteristic	EBHIS NGC 4214 NGC 5055	Basket-weaving NGC 5055	Unit
Spectral resolution		1.28	$[\mathrm{km\,s^{-1}}]$
Angular resolution		10.8'	
RMS noise level	60	18	$[\mathrm{mJy\,beam^{-1}}]$

Table 4.4: Effelsberg observations of NGC 4214 and NGC 5055. The angular and spectral resolution of all three data sets are identical. The measured noise value in the EBHIS data cubes for both NGC 4214 and NGC 5055 is about 60 mJy beam^{-1}. However, this value in the basket-weaving cube (Winkel et al. 2012a) of NGC 5055 is about 18 mJy beam^{-1}.

number of interferometric data sets with different physical properties are required. These have been kindly provided by F. Bigiel. For this aim, new interferometric data sets have been reimaged using the VLA raw data of the THINGS observations. The data cubes are the output of the THINGS imaging pipeline (Bigiel 2013, priv. comm.). The imaging process is presented in detail by Walter et al. (2008). All the data sets are corrected for the primary beam (Sec. 2.1.4) and the flux values are residual rescaled. The concept of flux residual rescaling is presented in App. D.2. The approach accounts for the resolution variations in different parts of an interferometric map. This is important to gain the true flux in a cleaned map. For extended structures with faint and diffuse gas, particularly around a galaxy, residual rescaling gains more importance. This is because the contribution of such structures to the measured flux in the cube is significant. In order to avoid any flux over- or underestimation all the VLA data presented in Chap. 4 has been residual rescaled in the process of imaging.

For both NGC 4214 and NGC 5055, 4 different data sets have been imaged (Table 4.5) from the same visibilities. For each galaxy, two data sets have the robust factor 5, which corresponds to natural weighting. The other pair has the robust factor 0.5, which corresponds to uniform weighting. It is important to mention that the robust factors are for Astronomical Image Processing System (AIPS, Greisen 1990). For other astronomical frameworks, the robust factors may differ. Accordingly, the final image with the robust factor 5 in AIPS can have different properties compared to the final image with the same robust factor imaged in MIRIAD. For each pair of data sets, two different pixel sizes: 1.5" and 3" are chosen. All the data sets have the same field of view (FoV), which makes the comparison easier.

The synthesized beam varies with the applied weighting scheme. Both dirty and clean beam have been discussed in Chap. 2. This is because, the sampling function (Chap 2) changes depending on the applied weighting.

Furthermore, the estimated RMS noise level is higher in the uniform weighted data cube. The noise level has been estimated using MAD.

Figure 4.7 presents the results of two different weighting schemes and pixel sizes for the NGC 4214 data sets. Figure 4.8 presents the same results for NGC 5055. In both figures the designation *NA* indicates the natural weighting and *UN* has been used for uniform weighting. The numbers 1024 and 512 in the captions of the figures correspond to the sizes of the data cubes in units of pixel in both spatial axes. The second number indicates the size of a pixel in the data cube in units of arc seconds.

4.3.4 The effect of weighting schemes and pixel size

In Sec. 4.3.3, it has been shown that different imaging parameters, in particular different weightings, affect the size of the synthesized beam, the measured total flux, and the estimated noise level for different

(a) NGC 4214 - 1024 1.5" NA

(b) NGC 4214 - 1024 1.5" UN

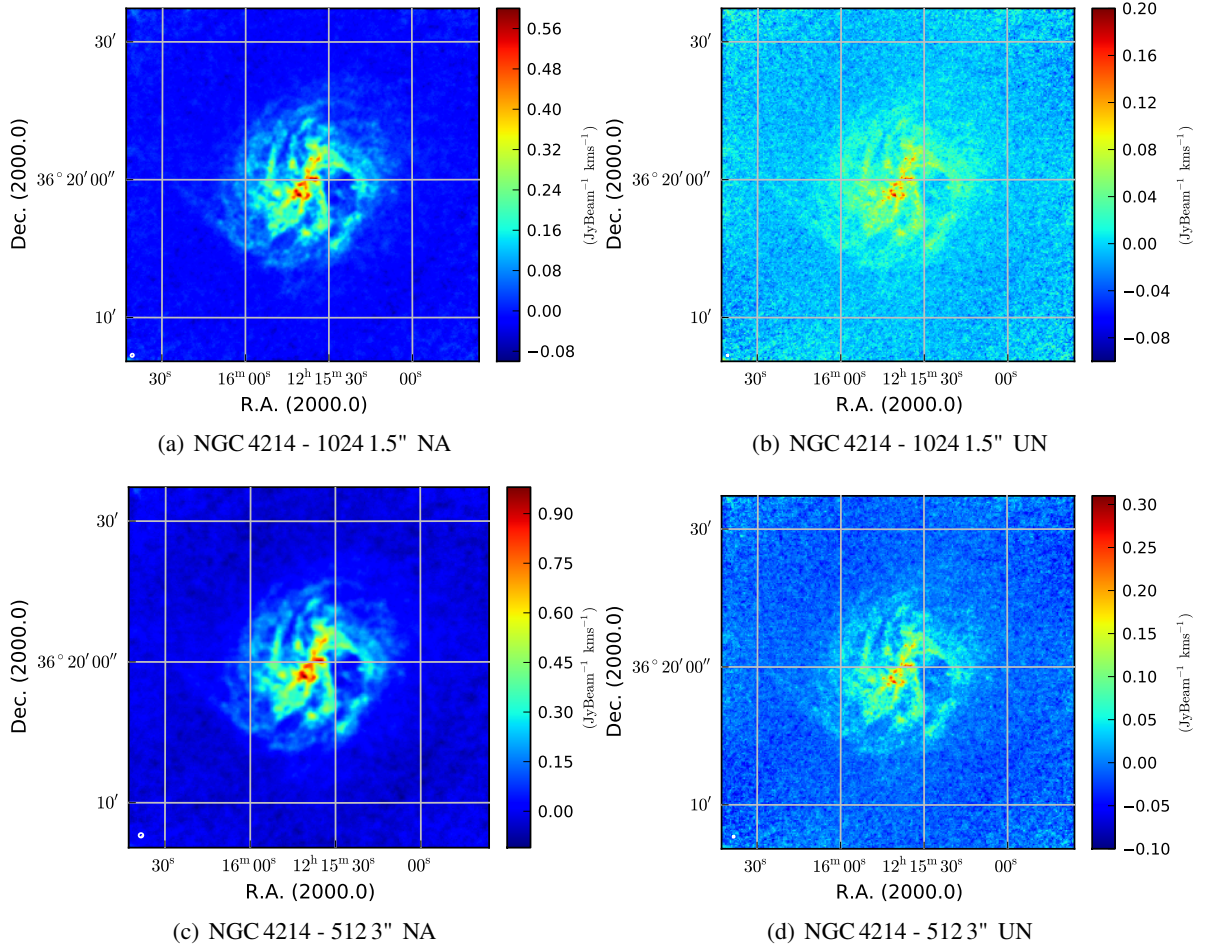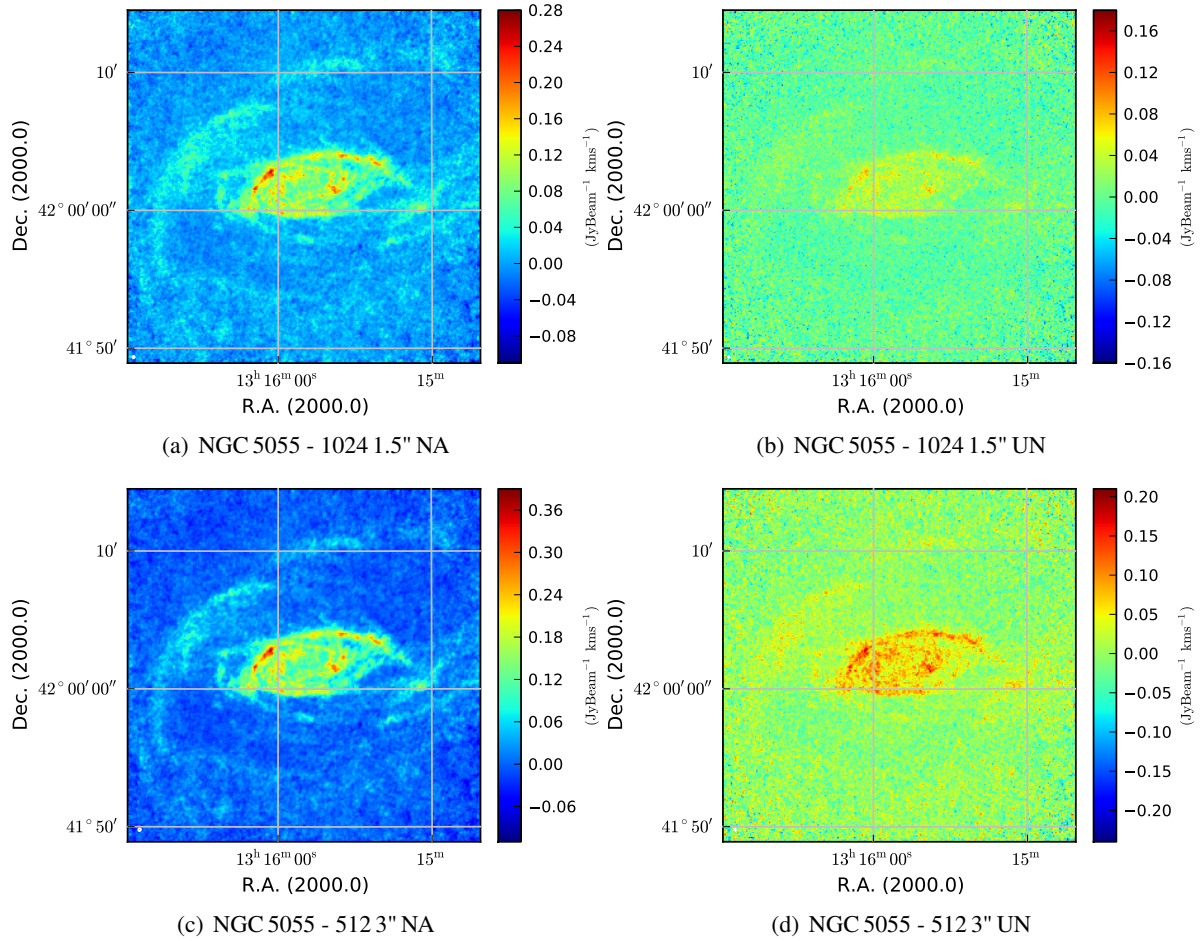(c) NGC 4214 - 512 3" NA

(d) NGC 4214 - 512 3" UN

Figure 4.7: Velocity-integrated maps for NGC 4214 with different imaging parameters and their impacts on the result of the interferometric image. All the presented data sets have the same FoV. However, they differ in applied weighting schemes and pixel sizes. NA stands for natural weighting scheme and UN designates the uniform weighting. Two pixel sizes 1.5" and 3" have been chosen. 1024 and 512 are the sizes of the data cubes in units of pixel along both spatial axes. Note that peaks of negative and positive values as well as the sensitivity vary in these data sets.

(a) NGC 5055 - 1024 1.5" NA

(b) NGC 5055 - 1024 1.5" UN

(c) NGC 5055 - 512 3" NA

(d) NGC 5055 - 512 3" UN

Figure 4.8: Velocity-integrated maps for NGC 5055 with different imaging parameters and their impacts on the result of the interferometric image. All the presented data sets have the same FoV. However, they differ in applied weighting schemes and pixel sizes. NA stands for natural weighting scheme and UN designates the uniform weighting. Two pixel sizes 1.5" and 3" have been chosen. 1024 and 512 are the sizes of the data cubes in units of pixel in both spatial axes. Note that peaks of negative and positive values as well as the sensitivity vary in these data sets.

NGC 4214	Pixel Size [arcsec]	Weighting	Beam size [arcsec]	Total flux [Jy km s^{-1}]	Noise [mJy beam^{-1}]
512×512	3	NA	18.7×19.8	116.1	0.27
512×512	3	UN	8.7×8.8	-0.57	0.28
1024×1024	1.5	NA	13.8×14.6	106.1	0.18
1024×1024	1.5	UN	6.3×7.4	-19.4	0.21
NGC 5055	Pixel Size [arcsec]	Weighting	Beam size [arcsec]	Total flux [Jy km s^{-1}]	Noise [mJy beam^{-1}]
512×512	3	NA	10.4×12.6	263.5	0.07
512×512	3	UN	7.6×8.0	110.4	0.19
1024×1024	1.5	NA	8.6×10.1	255.9	0.06
1024×1024	1.5	UN	5.3×5.8	81.1	0.13

Table 4.5: The natural (RA) and uniform (UN) weighted data cubes of NGC 4214 and NGC 5055. In the process of imaging, for each data set two different pixel sizes have been chosen. Furthermore, the noise level within the data cube is estimated. Beam size corresponds to the full width at half maximum (FWHM) of the beam minor and major axis in each data cube. The measured total flux for each data cube is presented. MAD has been used to estimate the RMS noise level.

data sets. Table 4.5 summarizes the important characteristics of different NGC 4214 and NGC 5055 interferometric data sets. *UN* and *NA* designate uniform and natural weighting schemes, respectively. The presented beam size for each data cube corresponds to the FWHM of the beam minor and major axis in the data cube. Additionally, the measured total flux as well as the RMS noise level are presented. Note that the RMS values have calculated in the data cubes with full spectral resolution of 1.28 km s^{-1}. The current section presents the causes of these variations in terms of measured total flux and total power as a function of different spatial scales in a data set. Additionally, the results of SSC for these data sets are presented.

Figure 4.9 shows the measured cumulative flux as a function of radial separation from the center of the maps for the presented interferometric maps of NGC 4214 and NGC 5055. The figure is arranged as follows: panel (a) shows the radial profile of all the cleaned interferometric data sets containing both negative and positive values. Panel (b) shows the radial profiles for the same data cubes with the exception that all the negative values are blanked. Panel (c) as well as panel (d) show the same for NGC 5055 data cubes, respectively.

The shape of the radial profiles for both galaxies can be explained as follows:

- **NGC 4214:** The amount of measured total flux increases in the central regions. The maximum of the cumulative flux is measured at a radius of about 8 arc minutes for all 4 data sets. These radii contain the bulk of the emission from the galaxy. For the larger radii the cumulative flux decreases. This is due to the deep negative bowls around the galaxy, which are the result of the missing spacings (Fig. 4.10) as described in Chap. 3. The measured total fluxes for both data sets with the natural weighting (panel a - red and green lines) are higher than the corresponding values measured in data cubes with the uniform weighting (panel a - blue and black lines). For a given weighting scheme, the amount of measured total flux is higher for data sets with larger pixel size (3").

Panel (b) shows the annuli fluxes for the data cubes of NGC 4214, for which the negative values

(a) NGC 4214: cumulative flux

(b) NGC 4214: positive cumulative flux

(c) NGC 5055: cumulative flux
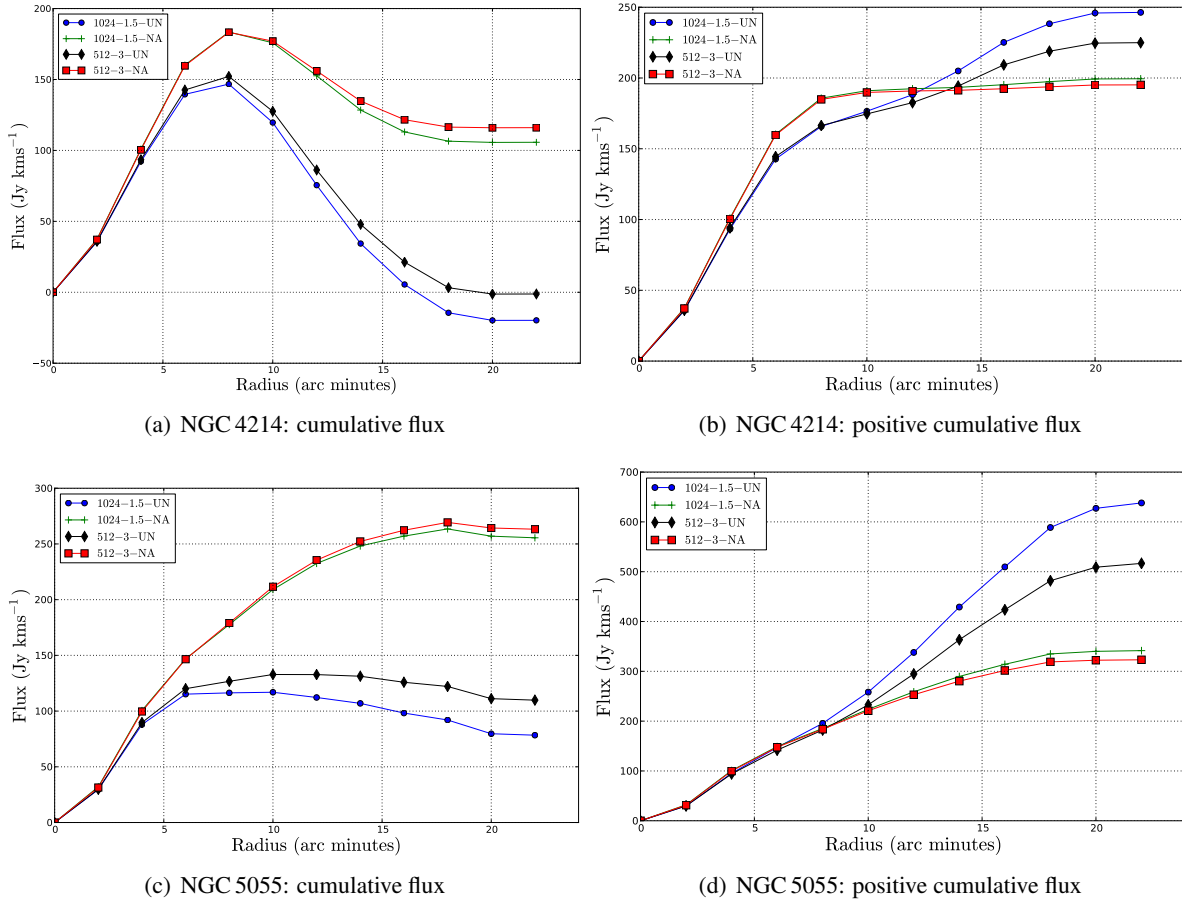
(d) NGC 5055: positive cumulative flux

Figure 4.9: measured cumulative flux as a function of radial separation from the center of the velocity-integrated maps for the presented interferometric maps of NGC 4214 (Fig. 4.8) and NGC 5055 (Fig. 4.8). NA and UN stand for natural and uniform weighting, respectively. Two different pixels sizes: 1.5" and 3" have been considered. 512 and 1024 are the number of pixels along both spatial axes. Panel (a) shows the radial profiles of all the cleaned interferometric data sets of NGC 4214, containing both negative and positive values. Panel (b) shows the radial profiles for the same data cubes with the exception that all the negative values are blanked. Panels (c) and (d) show the measured cumulative flux for the original and blanked data cubes of NGC 5055, respectively.

have been masked. As a result of the masking, the negative bowls around the structure vanish. Because of this, both curves corresponding to the natural weighting flatten out (panel b - red and green lines). The measured total flux is higher, yet still comparable with the measured value in the case in which the negative values have not been removed. The measured total flux in the masked data cubes with uniform weighting increases significantly (panel b - blue and black lines). In the case of uniform weighting, the curves are above the ones from natural weighting for large radii (panels a and b - black and blue lines). The higher value for the uniform weighting is caused by the positive value from the noise, which is higher in the uniform-weighted data sets as described before.

In the masked data sets, the measured total flux increases with smaller pixel size for a given weighting scheme. This is because, as the resolution increases, the noise values become on average higher. Since the negative bowls are eliminated after the masking, the amount of total flux is higher in these data sets.

- **NGC 5055:** The same findings as presented for NGC 4214 are generally valid for the data sets of NGC 5055. However, in contrast to NGC 4214, NGC 5055 has an extended H i disk. Additionally, the two galaxies reveal different angular scales located in different distances.

  The position of the negative bowls depends on the shape of the galaxy. The shape and depth of the bowls however, depends on the antenna pattern of the telescope. Due to the different distances to the galaxies (Table. 4.3) the bowls reveal different physical scales of the galaxy.

  The bowls arise through lack of information, i.e., they tend to occur where there is no measured interferometric signal. In the case of NGC 4214, there is not much gas structure at small angular scales at the location of the negative bowls. Therefore, the measured interferometric flux gets significantly negative, whereas in the case of NGC 5055, at this location, there is a considerable amount of compact gas present. This explains why the drops in panel (c) of Fig. 4.9 are much smaller than those present in panel (a) of Fig. 4.9.

Figure 4.10 shows a simple illustration of visibilities for an interferometric observation and the corresponding image. *The left panel* shows a box function. *The right panel* is the Fourier transformation of the box function (sinc function). Note that the negative bowls present in the sinc function are the result of missing information in the center of the (u, v) coverage. The presented figure in combination with Fig. 4.9 serve to explain the effect of two imaging parameters: weighting scheme and pixel size. This can be summarized as follows:

- **Weighting scheme:** Depending on the applied weighting scheme, a different region of the sampling function is emphasized. In the case of uniform weighting, these are long baselines. The sampling points in these regions are, however, more poorly sampled than the central regions. The image is the result of the Fourier transformation of the sampled visibilities, which in this case results in stronger oscillations. The side lobes have higher amplitudes resulting in deeper negative bowls around the structure.

  Natural weighting puts the emphasis on the short baselines, which are better sampled. Analogous, the corresponding regions in the sampling function are denser. As a result of this, the natural weighting yields a better sensitivity and the amplitude of negative bowls around the structures are lower compared to robust weighting. Subsequently, the amount of measured total flux in the data cube with natural weighting is higher.
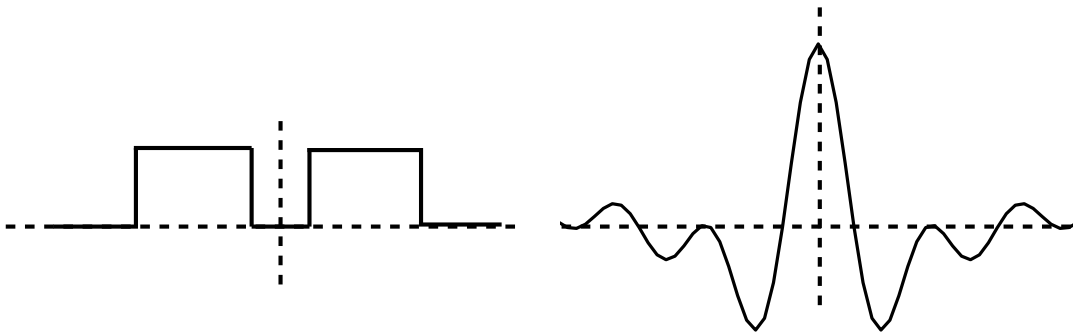
Figure 4.10: *The left panel* shows a box function. *The right panel* illustrates the Fourier transformation of the box function, which results in a sinc function. The missing information in the central region of the box function cause the deep negative bowls around the main lobe of the sinc function. This is a simplified illustration of the visibilities of an interferometer as well as the corresponding image.

- **Pixel size:** The effect of pixel size is less significant than that of weighting scheme as is also obvious in Fig. 4.9. This is purely an interpolation effect. A larger pixel grid smoothes the visibilities. This shifts the side lobes in the sinc function away from the main lobe as shown in Fig. 3.1. This again decreases the negative oscillations. Additionally, the smoothing eliminates the sharp edges of the box function (Fig. 3.1), which demagnifies the amplitude of the negative bowls around the bright structures.

An important finding regarding the cumulative flux profiles is the strong variation in the measured total flux if the negative values get blanked. As a matter of fact, discarding the negative values in interferometric maps is somewhat common. This results in higher measured total flux in interferometric data sets. This is even more significant for data sets with uniform weighting (blue and black lines). However, blanking the negative bowls prior to the combination is not sensible, since these are exactly the regions in the interferometric data, which are supposed to be filled with the information from the single-dish observation.

In addition to the presented analysis of cumulative radial profiles for the aforementioned imaging parameters, power spectral density (PSD) profiles have been computed for the same data sets. A PSD profile measures the amount of power corresponding to a specific angular scale as follows: first, the Fourier transformation of the image is calculated using a 2 dimensional FFT. Furthermore, an FFT-shift is required, so that low spatial frequencies are located in the center. The averaged power spectrum for concentric radii from the center results in the presented image. Through this analysis, it is possible to measure the amplitude of different scales for different data sets[2]. In the following, the result of the PSD analysis for NGC 4214 and NGC 5055 is presented.
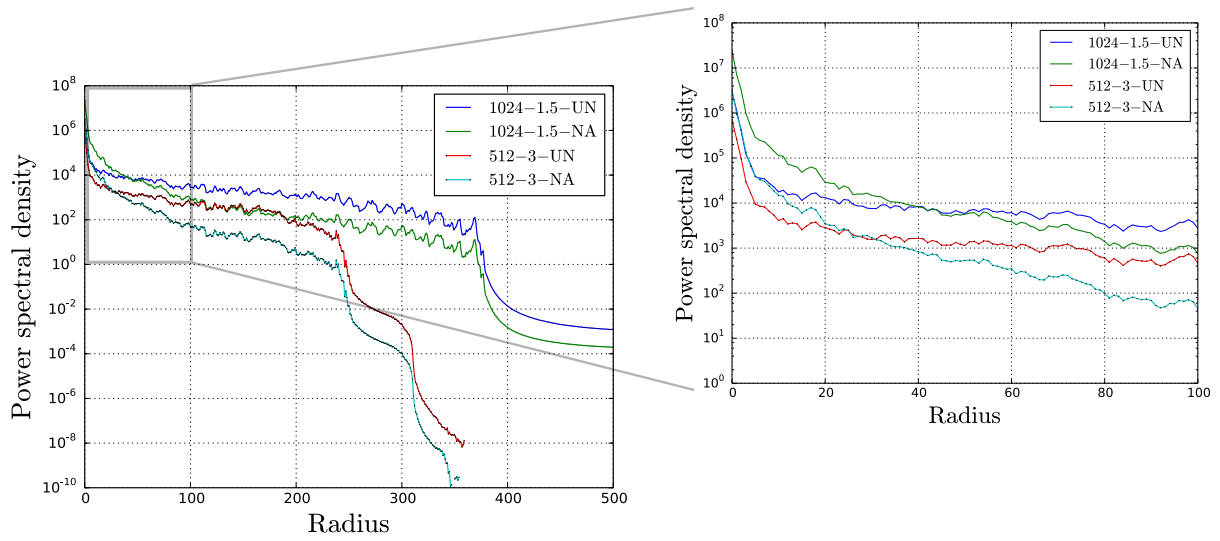
Figure 4.11 shows the results of the PSD analysis for NGC 4214 and NGC 5055 (Figs. 4.7 and 4.8). These data sets differ in the applied weighting scheme and pixel size (Sec. 4.3.4).

Panel (a) demonstrates the results of PSD for the NGC 4214 data sets, panel (b) shows the same for the NGC 5055 data, respectively. The total power for each cleaned data set is measured at the center of the velocity-integrated map. For each plot this region has been magnified (plots on the right). For both galaxies, the measured total power in the natural weighted data cube with smaller pixel size is the highest, whereas the total power measured in the uniform weighted data cube with larger pixel size is the smallest (red line in both figures). Considering the data sets with the same weighting scheme, the

---

[2] The radial profile for computing the PSD profiles has been adopted form astrobetter.com
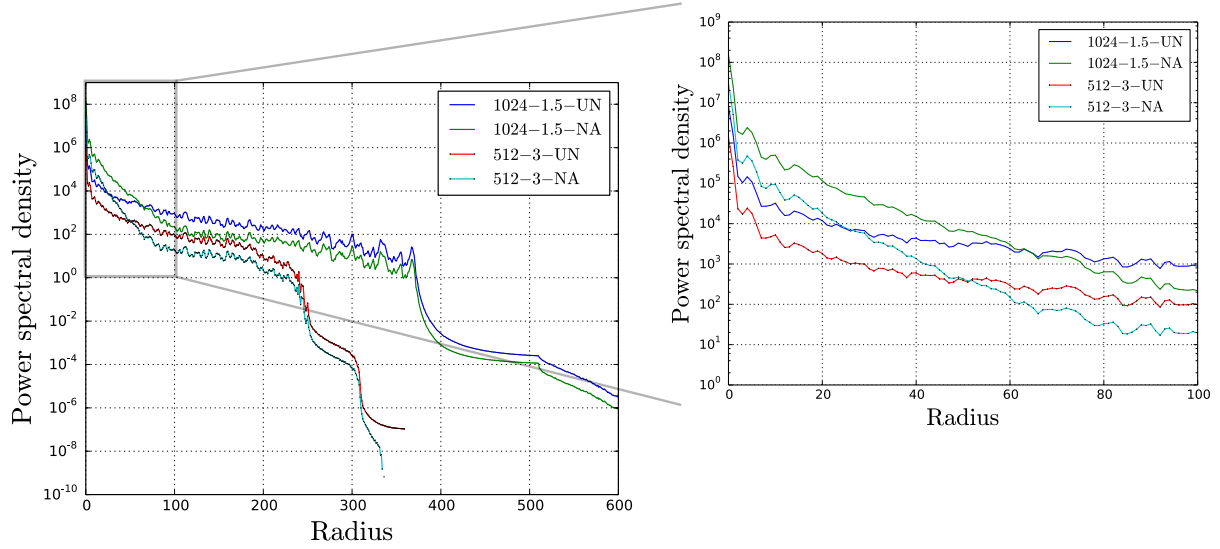
(a) NGC 4214 - power spectral density

(b) NGC 5055 - power spectral density

Figure 4.11: Results of the PSD analysis for the NGC 4214 and NGC 5055. The data sets differ in the applied weighting scheme and pixel size. Panel (a) demonstrates the result of PSD for NGC 4214 data sets, panel (b) shows the same for NGC 5055 data sets, respectively. The total power for each data set is measured at the center of the map. In plot this region has been magnified (plots on the right). The results show that the measured total power is higher in natural-weighted data cubes for a given pixel size. Note that the measured power profiles shown in the current figure are not normalized.

amount of measured total power is higher for the data set with smaller pixel size for all the radii and the difference seems to be constant. Note that the difference is not constant if one compares weighting schemes with constant pixel size.

Additionally, for data sets with the same pixel size, the amount of measured power within the inner radii is higher for natural weighting than the corresponding values for data sets with uniform weighting. However, this trend changes for larger radii corresponding to the outer region of the map. The results show that natural weighting results in highest total power in the inner regions, whereas the total power derived from the uniform-weighted data cube is higher in the outer radii. This is because natural weighting emphasizes the large angular scale structures, whereas uniform weighting puts the emphasis on small angular scale structures. In the outer regions the dominant factor is the noise. Therefore, the measured total power in the PSD profiles in the inner regions in higher for natural weighting, whereas this value is higher for outer regions in the case of uniform weighting.

4.4 The effect of imaging parameters on the SSC data

In the previous section it has been shown that weighting scheme and pixel size affect the result of the interferometric data significantly. Furthermore, the effect of each parameter has been analyzed in detail. In the current section, the impacts of these parameters on the result of the combination are discussed.

For all the data sets introduced in Sec. 4.3.3 the combination has been performed using the pipeline described in Chap. 3. However, the result of the combination will be discussed only for two data sets.

4.4.1 Result of SSC for NGC 4214

Figure 4.12 shows the results of the combination of single-dish and two different interferometric data sets for NGC 4214. The interferometric data sets differ in their weighting schemes, yet the pixel size (3") is identical in both data sets. The missing spacings for these data sets are provided by the EBHIS observation of the galaxy. Panels (a) and (b) show the interferometric and combined velocity-integrated maps for the natural weighting scheme. Panels (c) and (d) show data sets with the uniform weighting scheme, respectively. For all data sets the beams are represented by white circle on the bottom left. Note that, the beam is slightly smaller for the uniform weighted data. Panel (e) shows the velocity-integrated map of the regridded single-dish data cube for the same galaxy. There is no evidence of the spiral arms and small angular scale structures in the latter data set. This is the result of the poor single-dish resolution compared to the resolution of the interferometer. Note the huge difference between the beam sizes in the interferometric and combined maps compared to the beam size of the presented single-dish data cube.

The measured total flux in the combined data with natural weighting (panel b) is higher than the corresponding value measured in the data set with uniform weighting.

Figure 4.13 shows the measured cumulative flux profiles for various NGC 4214 data sets. All the panels show the measured cumulative flux for the regridded single-dish (red line), the interferometric (green line), and the combined (blue line) data cube. The data cubes differ in their pixel size: 1.5" and 3". However, they also differ in their number of pixels along both spatial axes, such that all the presented data sets have the same FoV. LR stands for low resolution (Effelsberg), HR for high resolution (VLA), comb for combination, respectively. For all the panels, total flux measured by the single dish is higher than the measured value by the interferometer. However, the measured cumulative flux for different radii varies strongly for the interferometric maps (see the discussion in Sec. 4.3.4). For the data sets with the uniform weighting, the negative bowls strongly reduce the cumulative flux. The measured total flux for these maps is lower than for the corresponding maps with natural weighting.

(a) NGC 4214: VLA$_{\text{NA}}$

(b) NGC 4214: Combined$_{\text{NA}}$

(c) NGC 4214: VLA$_{\text{UN}}$

(d) NGC 4214: Combined$_{\text{UN}}$
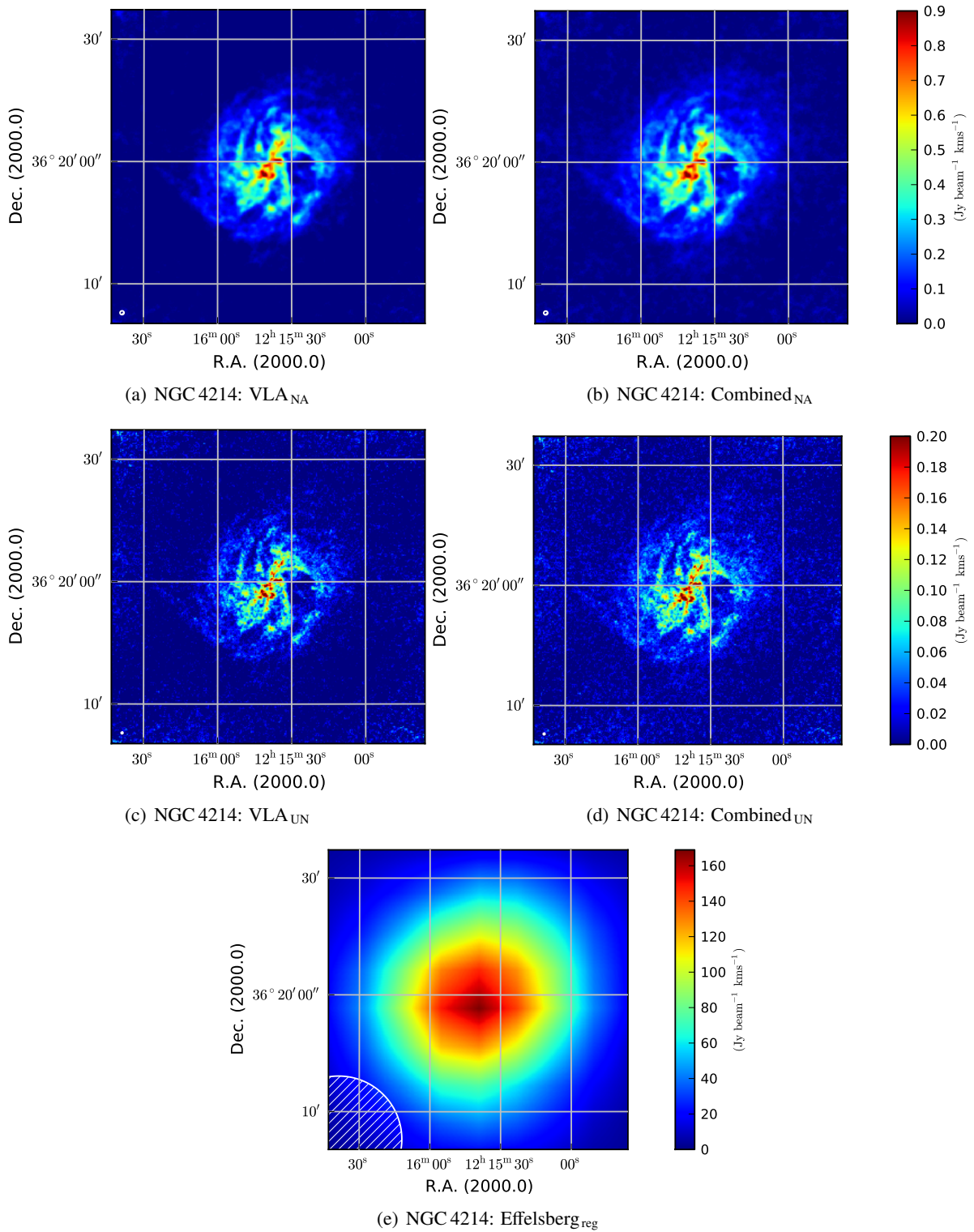
(e) NGC 4214: Effelsberg$_{\text{reg}}$

Figure 4.12: Velocity-integrated maps of interferometric and combined data sets for NGC 4214. Panel (a) shows the interferometric map with natural weighting (NA), panel (b) the result of SSC. Panels (c) and (d) show the same data sets with uniform weighting (UN). For each pair of data sets, the dynamic range for the color map is the same. Panel (e) shows the velocity-integrated map of the regridded single-dish data cube for the same galaxy. There is no evidence of the spiral arms and small angular scale structures in the latter data set as a result of poor resolution compared to that of an interferometer.

Moreover, the measured cumulative fluxes for the inner radii are higher in the interferometric maps than in the single-dish maps independent from the applied weighting scheme and pixel size. The latter phenomenon can be explained as follows: as the result of higher angular resolution in an interferometric map, the flux is more concentrated in the inner radii, whereas for outer rings the dominant component is the extended large scale structure (diffuse gas). The latter is more dominant in the single-dish maps. Therefore, the measured cumulative flux for outer radii is higher in single-dish data than in the interferometer. Figure 4.14 shows a simple simulation to demonstrate this effect. The top panel from left to right shows a simulated an arbitrary source, the single-dish, and interferometric observation of the source, respectively. It is apparent that the measured total flux in the inner radii is higher for the interferometric data sets, however, the latter values are higher for the larger radii in the single-dish data set.

For all the presented data sets, the results suggest that the effect of the negative bowls can be compensated through the SSC. The level of compensation, however, varies strongly depending on the interferometric data sets.

4.4.2 Result of SSC for NGC 5055

A similar analysis has been performed for different interferometric and combined maps of NGC 5055. There is a major difference between the presented interferometric maps of NGC 4214 and NGC 5055 (see discussion presented in Sec. 4.3.4). The interferometric map of the NGC 5055 reveals high emission values at the edges. The the outer regions of the galaxy, where possibly more diffuse gas exists are not observed at all. The single-dish observation of the galaxy covers the whole object. The single-dish is regridded to the interferometric grid prior to the combination (Sec. 3.3). Hence, the combined data cube does not consider the outskirts of the galaxy at all. In this case, the difference in measured flux corresponds to the extended and large angular scale structures located in the inner part of the galaxy in and between the spiral arms.

Moreover, the interferometric data cube needs to be corrected for the primary beam prior to the SSC. The correction is of significant importance regarding the measured true flux. Figure 4.15 shows the result of the combination. Panel (a) of Fig. 4.15 shows the interferometric map of NGC 5055 after the primary beam correction (PBC). The noise at the edges of the map is significantly higher than in the central regions. The latter property makes the combination for this data set even more complicated, since the higher noise level affects the result of the combination directly. In particular the outer regions of the combined map are vulnerable to the outliers.

After the combination, sub-images have been prepared. The latter maps show only the inner part of the galaxy without the high-level noise at the edges. Panel (b) shows the regridded single-dish data cube, panel (c) the interferometric data set. For the latter data set the natural weighting has been applied. The pixel size of this data cube is 1.5". Panel (d) shows the result of combination. The dynamic range of the color bars for are the same for both interferometric and combined maps.

Figure 4.16 shows the measured cumulative flux for different NGC 5055 data sets. The arrangement of the panels as well as the color coding is the same as described in Fig. 4.13. The highest measured flux is for the data sets presented in panel (a). The latter panel presents the result of the combination for the natural weighted interferometric map with a pixel size of 3". The measured total flux for the latter interferometric data set is also the highest. This is also the case regarding the measured total flux in the corresponding interferometric map. Note the shape of the green line (interferometer) in all four panels. Contrary to the green lines (interferometer) presented in Figs. 4.13, the interferometric data sets of NGC 5055 do not exhibit any steep drops. In all the presented cases, except for panel (c) the measured total flux in the combination is in line with the measured total flux in the single-dish data cube. In the

(a) 512 - 3" - Natural

(b) 512 - 3" - Uniform

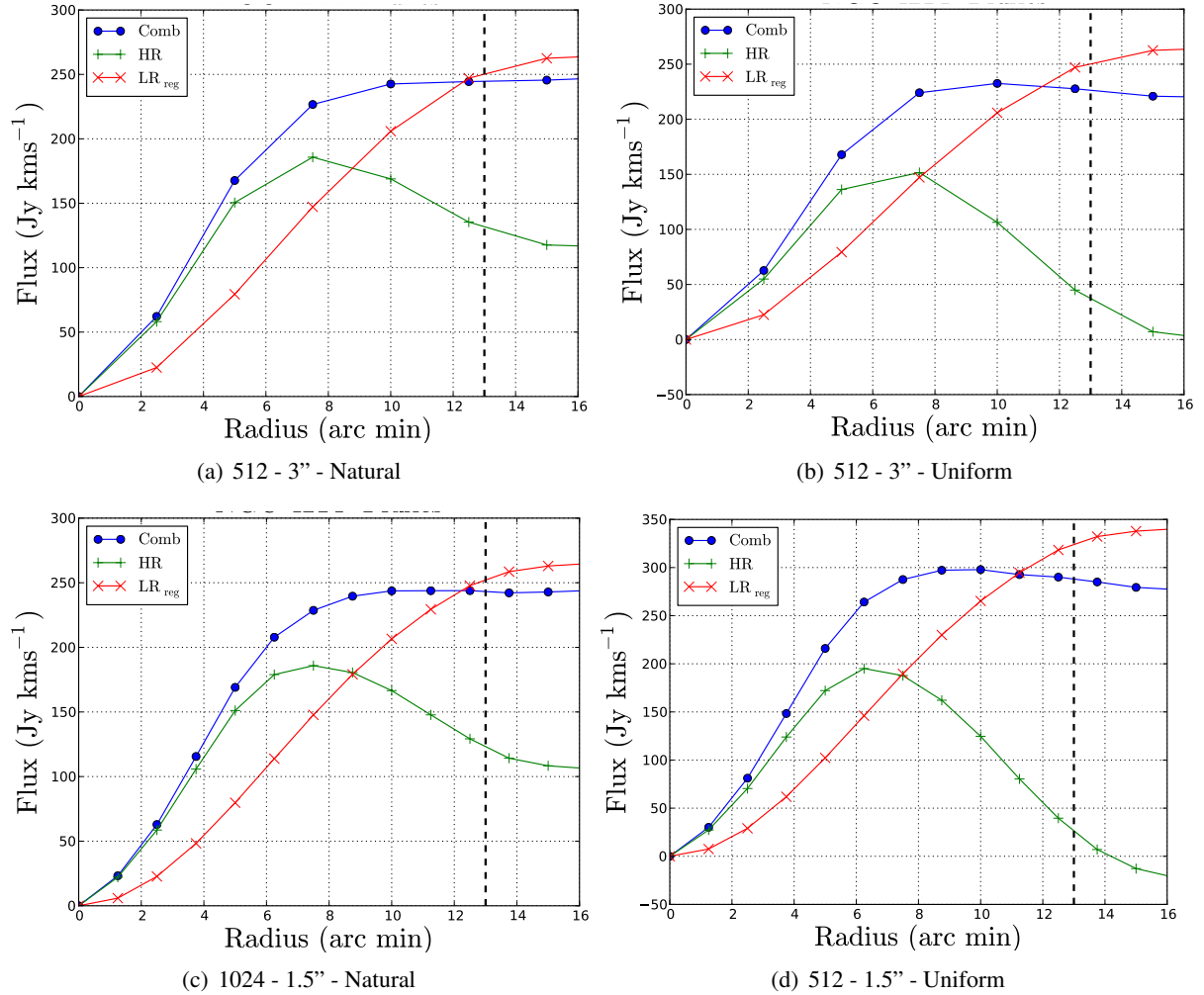(c) 1024 - 1.5" - Natural

(d) 512 - 1.5" - Uniform

Figure 4.13: Measured cumulative flux for various NGC 4214 data sets. All the panels show the measured cumulative flux for the regridded single-dish (red line), interferometric (green line), and combined (blue line) data cube. The size of the data cubes are different with 1.5" and 3", however, they also differ in the number of pixels along both spatial axes. All the presented data sets have the same FoV. LR stands for low resolution (Effelsberg), comb for combination, and HR for High resolution (VLA). For all the panels, the single dish measures a higher flux as it is expected. The measured total flux for different radii varies strongly for the interferometric maps (see the discussion in Sec. 4.3.4). For all the presented data sets, the effect of the negative bowls can be compensated through SSC. The level of compensation however, varies strongly depending on the interferometric data sets.
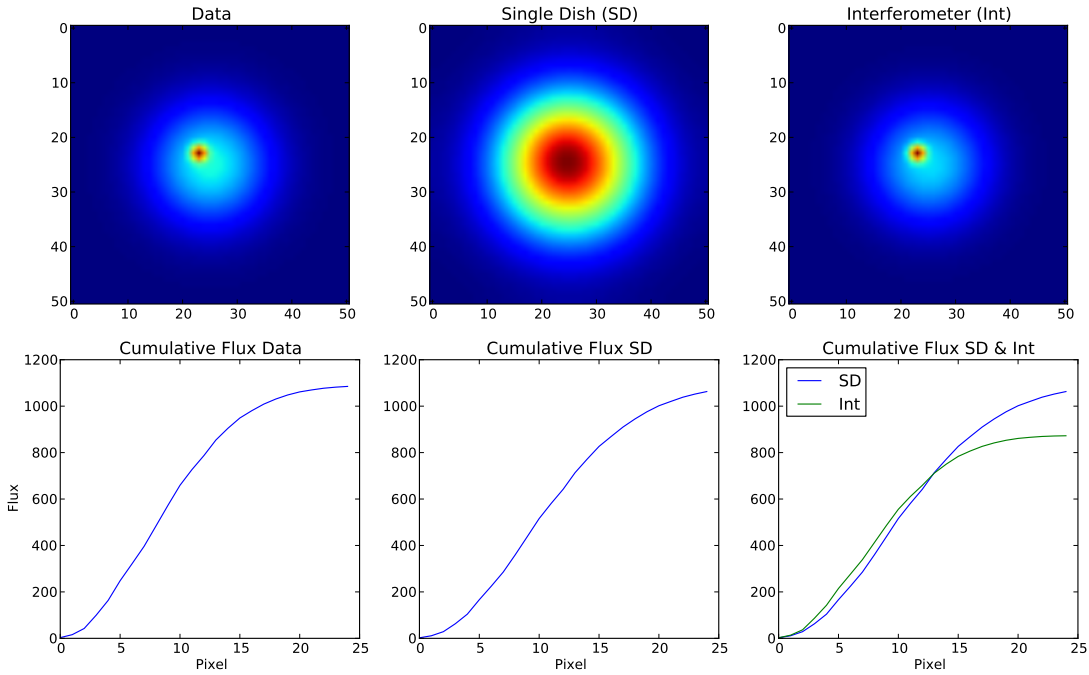
Figure 4.14: Simple simulations of a source, the corresponding single-dish, and interferometric observations of the source. Top panels from left to right show the simulated source, the single-dish, and the interferometric observations of the source. The bottom panels from left to right show the measured cumulative flux for different radii from the center of the maps. It is apparent that the measured total flux in the inner radii is higher for the interferometric data sets, however, the latter values are higher at larger radii in the single-dish data set.

case of NGC 5055, a major portion of the single-dish emission is cut off at the edges of the map, since the interferometric map only covers the galaxy partially. Through the combination, part of the cut-off emission is brought back, which can result in higher flux value in the combined data cube.

4.5 The effect of the interferometric array on the SSC data

So far, the effects of imaging parameters on the result of the synthesized image and the SSC data have been discussed. However, there are other parameters, which can affect the result of the synthesized image. The variations in the latter image are of great importance, since these have strong impacts on the result of SSC. Part of these impacts have been discussed in the previous section (Sec. 4.4). In the current section, the effect of array's configuration on the result of synthesized image will be discussed. On this account, the interferometric data sets obtained with two different interferometric arrays: the Westerbork Synthesis Radio Telescope (WSRT) and the VLA will be analyzed. Thus far, various interferometric data sets for the VLA observation of NGC 5055 (THINGS) have been discussed. The galaxy has also been observed with the WSRT as part of the HALOGAS ensemble.

WSRT and SSC data

Table 4.6 summarizes the important observational parameters of single-dish, interferometric, and combined data cubes of NGC 5055. The single-dish data cube has been observed using the basket-weaving approach (Winkel et al. 2012a) as described in Sec. 4.3.3. The combination has been performed for

(a) NGC 5055: VLA - PBC

(b) NGC 5055: Effelsberg_reg
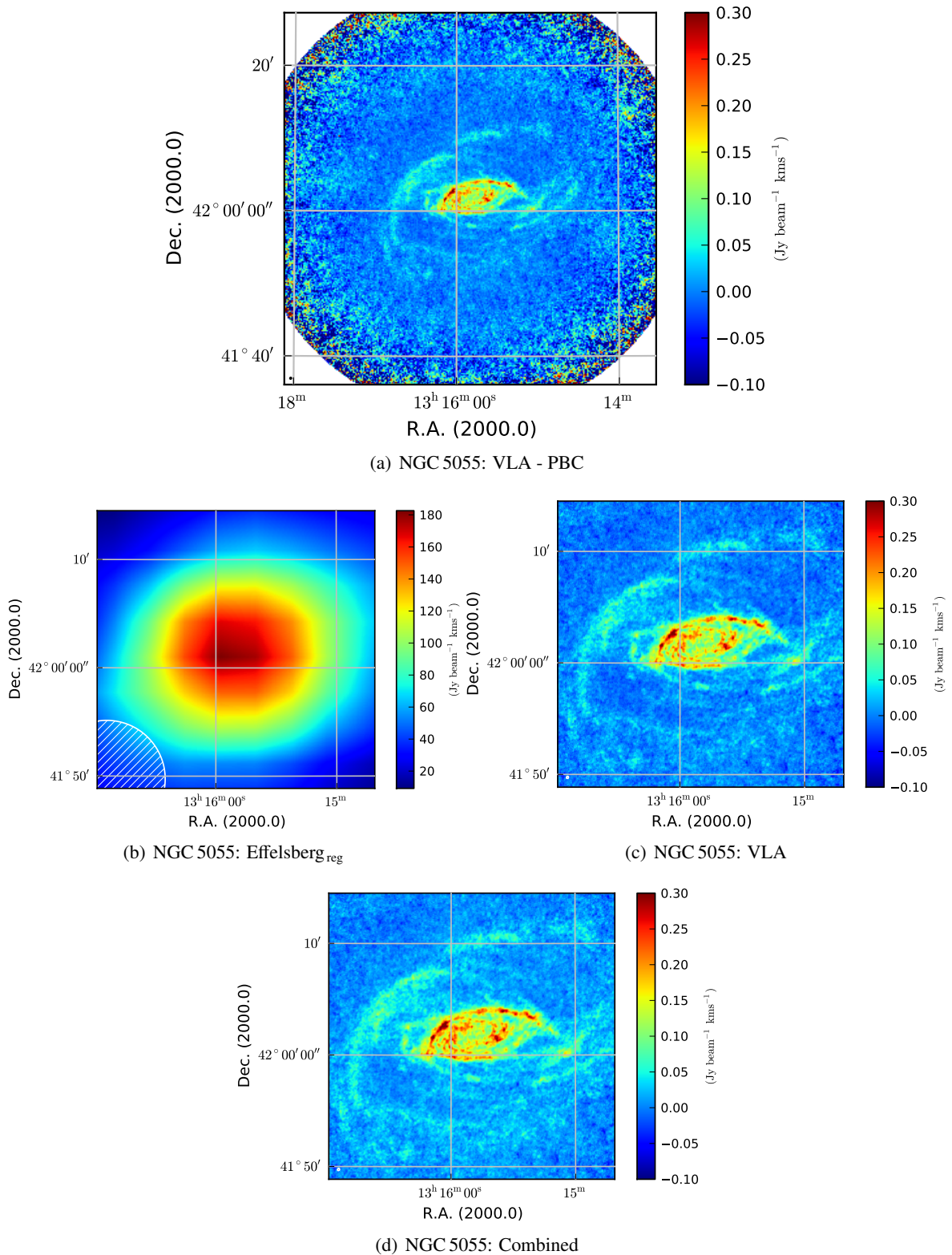

(c) NGC 5055: VLA

(d) NGC 5055: Combined

Figure 4.15: Velocity-integrated maps of NGC 5055. Panel (a) shows interferometric map after the PBC, where the higher noise level at the edges of the map is the result of PBC. Panel (b) shows the regridded single-dish data cube, panel (c) the interferometric data cube, and panel (d) the result of their combination. For both interferometric and combined data sets the dynamic range of the color maps is identical. Note that panels (b) to (d) show only the inner part of the map without the high-level noise at the edges.

(a) 512 - 3" - Natural

(b) 512 - 3" Uniform

(c) 1024 - 1.5" - Natural

(d) 512 - 1.5" - Uniform
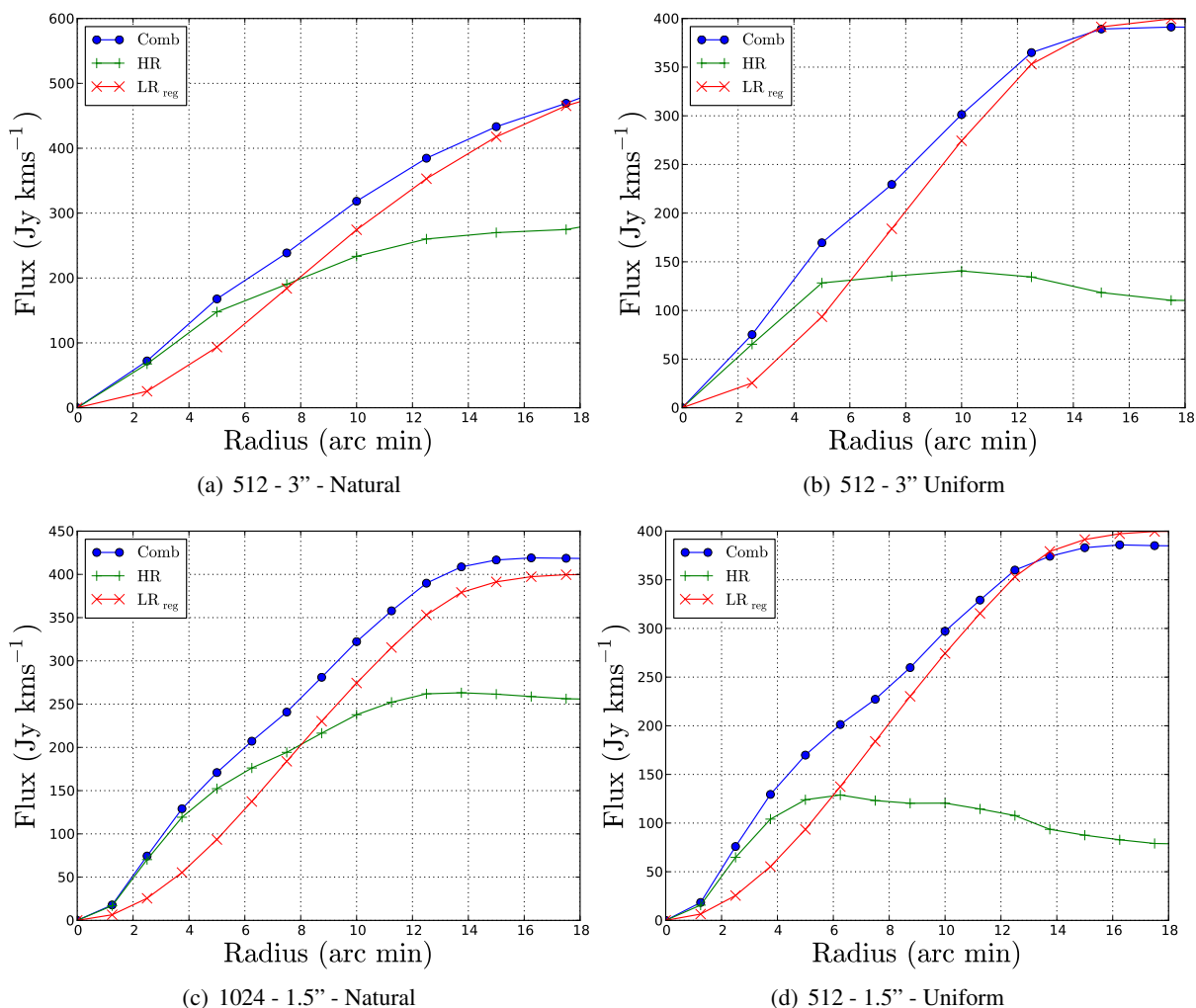
Figure 4.16: Measured cumulative flux for various NGC 5055 data sets. All the panels show the measured cumulative flux for regridded single-dish (red line), interferometric (green line), and combined (blue line) data cube. The size of the data cubes are different with 1.5" and 3", however, they also differ in the number of pixels in both spatial axes, such that all the presented data sets have the same FoV. HR stands for high resolution (VLA), LR for low resolution (Effelsberg), and comb for combination. The measured total flux for different radii varies strongly for the interferometric maps. For all the presented data sets, the effect of the negative bowls can be compensated through SSC. The level of compensation, however, varies strongly depending on the interferometric data sets.

Characteristic	SD_{reg}	Int	Comb	Unit
Spectral resolution		4.1		$[\text{km s}^{-1}]$
Angular size of a pixel		7.9"		
Radial velocity range		$154 \leq V_{sys} \leq 846$		$[\text{km s}^{-1}]$
Beam area	7478.3	20.1	20.1	
Angular resolution	10.8'	34"	34"	

Table 4.6: The observational parameters of the HALOGAS observation of NGC 5055. Note that spectral resolution, angular size of a pixel, and radial velocity range are identical for all three data sets.

the HALOGAS data cube without PBC as well as for the primary-beam-corrected data cube. The primary beam correction has been performed using the MIRIAD task `LINMOS`. Appendix D.1 presents the function, which describes the attenuation of the WSRT beam.

Figure 4.17 shows the WSRT observation of the NGC 5055 before (*left panel*) and after the PBC (*right panel*), where PBC results in high noise level at the edges of the map.

In the following, the result of the combination for the interferometric data cube prior and former to the PBC are presented. Figure 4.18 shows the total flux density maps. Panel (a) presents the regridded single-dish data, panel (b) the interferometric data (without PBC), and panel (c) shows the results of their combination. Panel (d) presents the measured cumulative flux for different radii from the center of both interferometric and combined maps. The largest radius is about 16". This is roughly the largest radius before the noise rises significantly in the primary-beam-corrected data sets. The blue line shows the measured total flux in the PBC combined data, the green line in the combined data without the PBC, the red line in the PBC interferometric data, and the black line in the interferometric data cube with the PBC. The difference between the red and black line results from the PBC (see Sec. 2.1.4). Through the division of the interferometric map by the primary beam of a single antenna of WSRT the flux values rise form the central regions towards the outer regions of the maps. For the larger radii the difference becomes more significant. Not that the PBC also affects the negative bowls such that they get even more negative. However, the result of the combination shows small variations between the data sets with or without the PBC. A very interesting property of the NGC 5055 is that the difference between the interferometric and combined maps is not very large. It suggests strongly that despite its extended neutral atomic hydrogen (H I) disk (Patterson et al. 2012) the galaxy does not contain a significant amount of diffuse gas.

As a last step, the VLA and WSRT interferometric data cubes are compared. The approach to be introduced is a very simple way to study the effect of the array configuration on the result of the synthesized image. However, the results from this study should be considered with care. This approach attempts to reveal the resulting differences in both data sets. However, it should be mentioned in advance that one cannot rule out the fact that also a different *clean* philosophy plays a significant role on the final result of the synthesized image. This is in particular can be relevant for the presented data sets in this section since both surveys: HALOGAS and THINGS follow different clean approaches. In the case of HALOGAS the clean level is about $1\sigma_{rms}$ or in some cases even slightly below this threshold (G. Heald 2012, priv. comm.), whereas for the data sets of the THINGS ensemble the clean level is in the range of $2 - 2.5\sigma_{rms}$ (Walter et al. 2008). The duration of the observation is another important factor, which can result in sever differences in various observations of an object.

By design, the east-west interferometer has a denser coverage in the central parts of the (u, v) plane. Therefore, the latter instruments are more sensitive towards the large angular scale structures in an
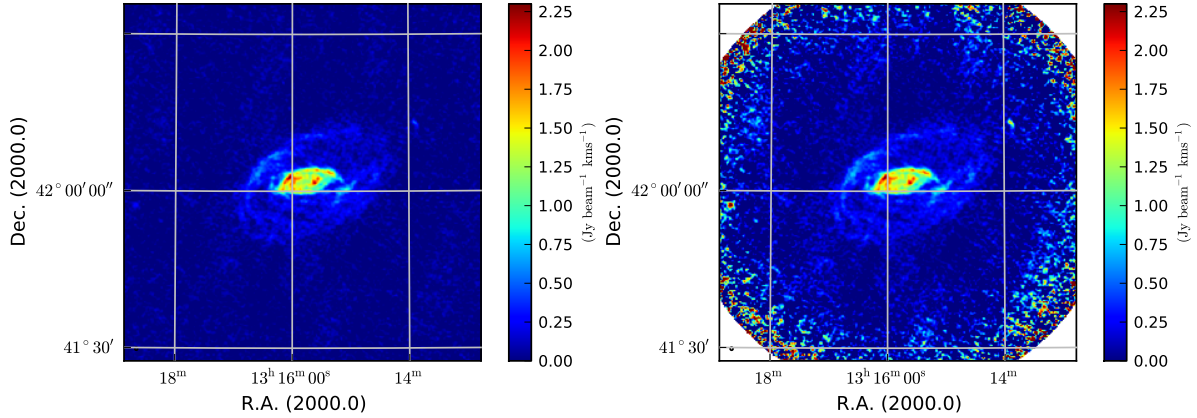
Figure 4.17: *The left panel* shows the HALOGAS observation of NGC 5055 before the PBC, *the right panel* the same data after the PBC. The dynamic range of the color maps for both data cubes is identical.

Characteristic	WSRT	VLA	Unit
Angular resolution	34"	11"	
Spectral resolution	4.1	5.1	[km s^{-1}]
Pixel size	7.9"	3"	

Table 4.7: Different characteristics of the VLA and WSRT observations of NGC 5055

object. In fact, this is the case for the WSRT, whereas the VLA achieves a better instantaneous (u, v) coverage. For this purpose both WSRT and VLA observations of NGC 5055 have been analyzed. The VLA observation is a single pointing, whereas the WSRT observation is an interferometric mosaic consists of 6 pointings. Therefore, the FoV of both data sets are different. Additionally, both data sets have different angular and spectral resolution. Both data sets also differ in their pixel size. However, the applied weighting scheme for both data sets is identical, namely natural. The VLA data cube reveals the largest measured total flux among the analyzed VLA data cubes (Table 4.5). Both data sets are in units of Jy beam^{-1}. Table 4.7 summarizes the observational parameters of both data sets.

For the comparison, it is required that both data sets have the same projection and geometry. Therefore, both data sets have been regridded using the IMREGRID task of Common Astronomy Software Applications (CASA, McMullin et al. 2007). The regridded WSRT data cube has now the same projection and spectral resolution as that of the VLA observation. These data sets only differ in their angular resolution, which is higher in the VLA data cube. A Gaussian convolution with an appropriate kernel is required to smooth down the resolution of the VLA data to that of the WSRT. Figure 4.19 shows the result of the latter approach. Panel (a) shows the regridded data cube for the WSRT, panel (b) the convolved data cube for the VLA. Both data cubes have the same projection, angular, and spectral resolution. Furthermore, PSD profiles have been computed for both maps (panel c). The blue line corresponds to the measured profile for the WSRT data, the green line for the VLA. Note the clear difference between the two lines. While for the inner radii, up to 50 pixels corresponding to an extent of about 7' by a given pixel size of approx. 8", where the small angular scales are more dominant both data sets reveal almost the same behavior. For the larger radii (up to 100 pixels $\hat{=}$ 13"), corresponding to the outer regions of the map, the WSRT data measures a distinctly higher power. For regions beyond the 100 pixel radius the difference between the blue and green line seems to be constant and the PSD profile is
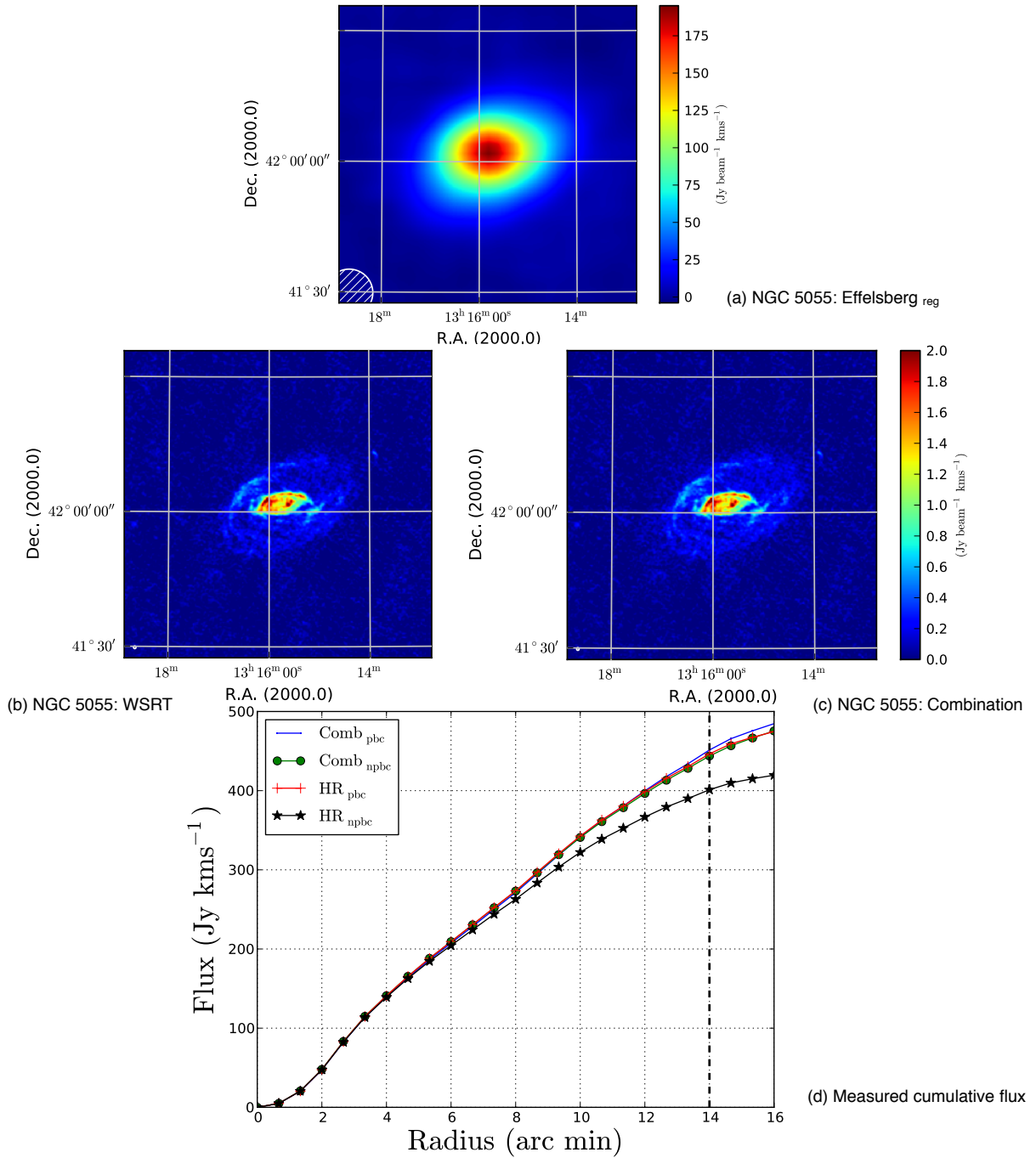
Figure 4.18: Total flux density maps of NGC 5055. Panel (a) shows the regridded Effelsberg data, panel (b) the WSRT data, and panel (c) the result of their combination. Panel (d) shows the measured cumulative fluxes for the WSRT data cubes before and after the PBC and their corresponding combined maps. The values have been compared in all the data sets up to a radius of about 16". Comparison of the measured flux values at larger radii is difficult due to the high-level noise at the borders of the PBC maps. For the smaller radii the difference is negligible and it increases for larger radii. The measured total flux in combined map compared to the corresponding value in the interferometric map suggests strongly that the galaxy does not contain large portion of diffuse, warm gas.

flat. These are the regions of the noise around the galaxy. The shape of the curves suggest that the amplitude of the noise in the WSRT data cube is higher (smaller angular scale) than in the VLA data cube. However, regarding the latter finding other parameters such as different clean approach or philosophy can also contribute significantly to such behavior. Nevertheless, it is expected that the WSRT is more sensitive towards the large angular scale structures because of its setup. Panel (d) presents the result of the cumulative flux density for the aforementioned data sets. The latter findings confirm the results of the PSD profiles. In the velocity-integrated map of the WSRT the measured total flux is 4.5 Jy kms^{-1}, whereas the corresponding value in the VLA data cube is only 2.6 Jy kms^{-1}.

4.6 Conclusions

The current chapter is devoted to the systematics regarding interferometric observations and imaging parameters. The latter affect the results of the synthesized image and the SSC data, subsequently. Different objects and different synthesized imaging strategies have been considered in the current chapter:

- The result of the SSC for a sample of three nearby galaxies: NGC 2403, NGC 4214, and NGC 5055 from the THINGS ensemble, is presented.

- For low Galactic latitudes, the single-dish observation of the galaxy is embedded with the strong Galactic emission. This is significant if the object is located close to the plane of the Milky Way (Verschuur & Kellermann 1988). The effect of the contamination with the Milky Way emission is analyzed in the case of NGC 2403. For this study, the single-dish and interferometric data is combined.

- It is shown that for NGC 2403 the Milky Way emission present in the single-dish data propagates into the SSC. The Milky Way emission cannot be characterized by a simple Gaussian (den Heijer, Ph.D thesis, in prep.). As a result of this, the first-moment map of the combined data is strongly biased by the strong Galactic emission and the derived kinematical properties are not accurate.

- The difference between the interferometer and the combined data of NGC 2403 apparent in their spectra reveals the dominance of the Galactic emission in regions around 0 km s^{-1}. It decreases with higher radial velocities. However it is not possible to determine the amount of Galactic emission, which is added to channels further away for 0 km s^{-1}due to SSC.

- Additionally, the effect of two imaging parameters: pixel size and weighting schemes is discussed. The results reveal that the effect of different pixel sizes on the result of the interferometric image is minor, whereas the choice of weighting schemes changes the properties of the dirty and cleaned image dramatically.

- For the studied extragalactic objects, all the results are in favor of more natural weighted data at cost of losing resolution, if SSC is of interest for measuring of total flux or studying of extended structures. For the study of the most components the uniform weighting is the more appropriate choice.

The most significant result from the current study is that not every interferometric data set is appropriate for the combination. The result of the combination suffers, beyond doubt from the effects present in the cleaned interferometric image such as negative bowls. Depending on the case study, the synthesized data needs to be prepared for the combination.

(a) NGC 5055 - VLA

(b) NGC 5055 - WSRT
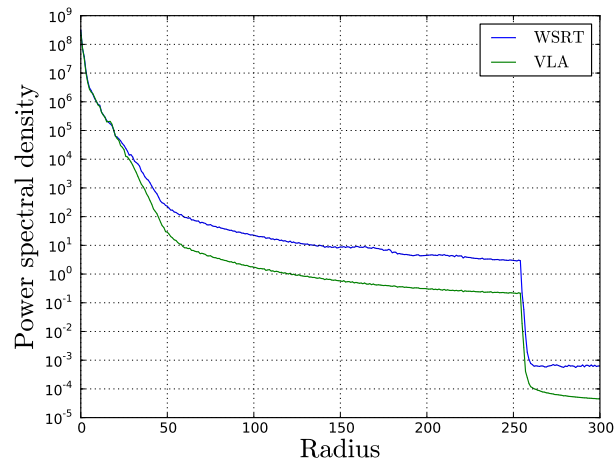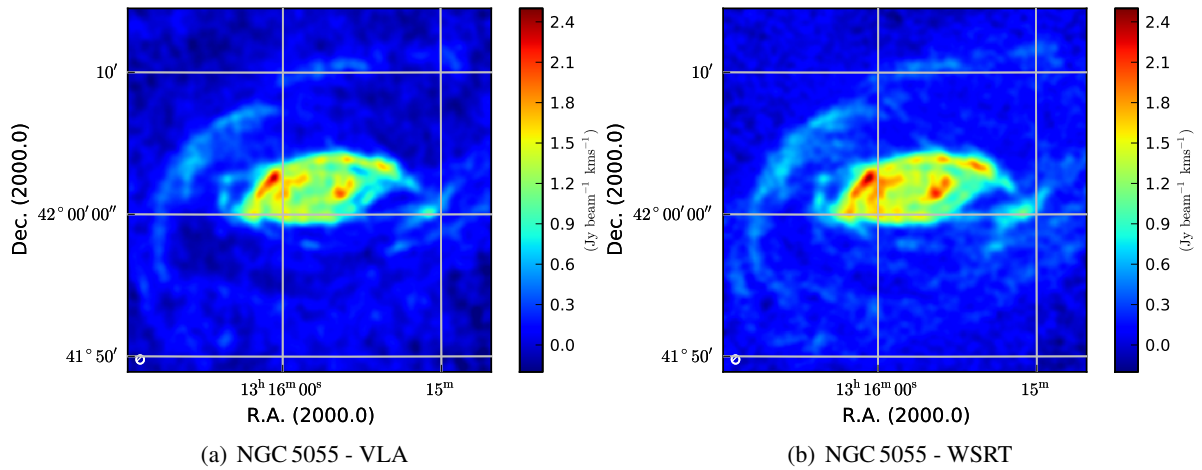
(c) VLA & WSRT - power spectral density
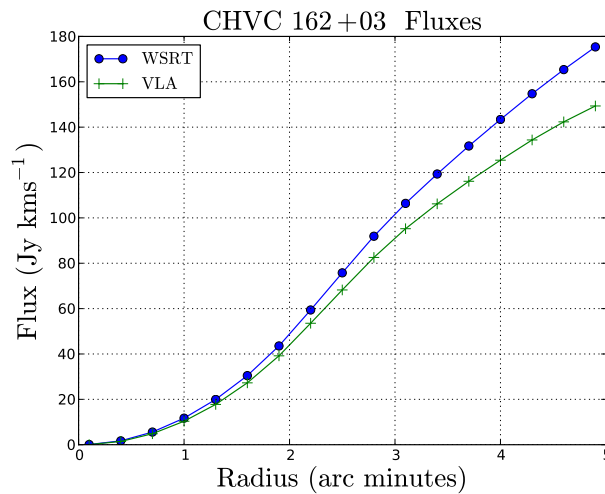
(d) VLA & WSRT - Cumulative flux

Figure 4.19: Panel (a) shows the convolved VLA map of NGC 5055 such that the corresponding angular resolution is identical to that of the WSRT. Panel (b) presents the regridded WSRT map. Both maps presented in panels (a) and (b) have the same projection, angular, and spectral resolution. Furthermore, PSD profiles have been computed for both maps. The blue line presents the PSD profile of the WSRT observation and the green line of the VLA.

Additionally, the results suggest that for the nearby galaxies natural weighting is the more appropriate scheme, whereas the impact of pixel size is rather insignificant. However, smaller pixel size increases the computational cost. It can matter if the data cubes are significantly large (disk space).

An additional factor, which has been studied is the choice of the interferometric array. A comparison between observations of tow different interferometric arrays: VLA and WSRT as well as the result of the SSC for these data sets are presented. This study shows that for the NGC 5055 observations, the amount of measured total flux does not vary strongly for both VLA and WSRT. This is despite the fact that both arrays are very different. Moreover, the data reduction philosophies vary significantly for these two data sets. Nevertheless, the amount of measured total flux in the interferometric data cube does not differ significantly from the corresponding value in the single-dish data cube. This result suggests strongly that NGC 5055 does not contain considerable amount of diffuse gas.

The next step is to study the effect of different deconvolution approaches for different observations. This study is complementary to that in the present work. This is especially so because the choice of deconvolution approach, as well as the way it is conducted, have significant impacts on the form of the final cleaned interferometric map. Deconvolution directly influences the result of the SSC. However, such a study requires elaborate investigation which is beyond the scope of the presented thesis.

Compact high-velocity clouds around the Milky Way

Abstract

We present deep neutral atomic hydrogen (H I) observations of three compact high-velocity clouds (CHVCs). The main goal is to study their diffuse warm gas and compact cold cores. We use both low- and high-resolution data obtained with the 100 m Effelsberg telescope and the Westerbork Synthesis Radio Telescope (WSRT). The combination is essential in order to study the morphological properties of the clouds, since the single-dish telescope lacks a sufficient angular resolution, while the interferometer misses a large portion of the diffuse gas. Here single-dish and interferometer data are combined in the image domain with a new combination pipeline. The combination makes it possible to examine interactions between the clouds and their surrounding environment in great detail. The apparent difference between single-dish and radio interferometer total flux densities shows that the CHVCs contain a considerable amount of diffuse gas with low brightness temperatures. A Gaussian decomposition indicates that the clouds consist predominantly of warm gas.

---

[1] Note that in the presented chapter some minor changes have been undertaken compared to the submitted version by (*A&A*). Additionally, Sec. 5.2 and Sec. 5.3 have been extended. Figures 5.1 and 5.3 are not available in the publication. They have been added subsequently.

5.1 Introduction

high-velocity clouds (HVCs) are H I clouds with radial velocities incompatible with simple Galactic rotation models (Wakker & van Woerden 1997). After their initial discovery by Muller et al. (1963), they have been observed all around the Milky Way. Blitz et al. (1999) suggested that the HVCs are distributed throughout the Local Group, but this theory has been disproven several times by searching for HVCs around other galaxies. All these observations have either failed to find any HVCs (Pisano et al. 2004, 2007) or located them very close to their host galaxies (Thilker et al. 2004). HVCs are found either as compact and isolated objects or as part of large complexes (Wakker & van Woerden 1997).

Recent studies propose three main hypotheses for the origin of HVCs (Bregman 2004). First, HVCs consist of primordial gas that is accreting onto galaxies. It can be primordial gas flows from the filaments or have its origin in gaseous dark matter haloes. Second, HVCs originate from the tidal and ram-pressure interaction of the Milky Way Galaxy with dwarf galaxies. Third, HVCs have been formed as the result of a galactic fountain, i.e., by gas flows driven by supernovae. Still the most serious problem is the limited information on the HVCs distances (van Woerden et al. 2000; van Woerden & Wakker 2004; Kalberla et al. 2005; Barentine et al. 2008).
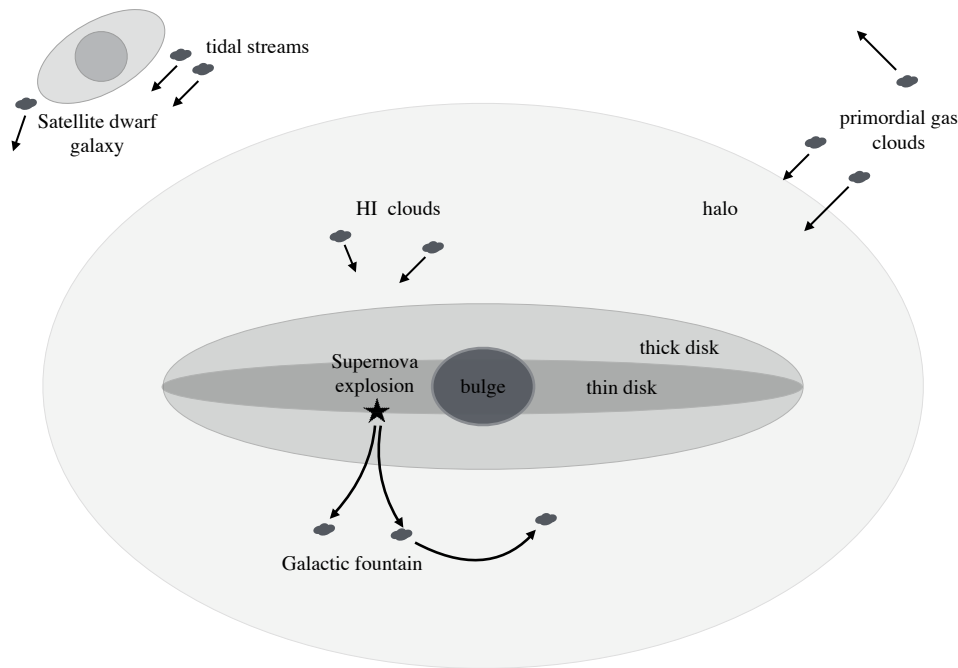

Figure 5.1: Large-scale flows in the halo. Schematic view of three main hypotheses for the origin of HVCs; 1. primordial gas accreting onto galaxy. 2. clouds originate from tidal interaction of the host galaxy with dwarf galaxies. 3. galactic fountains. The sketch is not to scale. Recreated after image presented by Westmeier (2007). Note that the figure is not available in the *A&A* publication and it has been added subsequently for illustrative purposes.

Investigations of the physical conditions of HVCs indicate that some show signs of interaction with the Galactic halo gas (Brüns et al. 2000, 2001; Westmeier et al. 2005b; Putman et al. 2011; Venzmer

et al. 2012).

The aim of this study is to investigate the morphological properties of CHVCs as well as their radial velocity and linewidth. In the past, the existence of two different gradients either in density (Putman et al. 2011) or velocity (Brüns et al. 2000) were required within the cloud for the designation head-tail (HT). The objects studied here appear to conform to both these criteria. The appearance of the HT structure is interpreted as follows. As the cloud moves through the hot and ionized halo, part of the cloud is compressed. This higher density area constitutes the head of the cloud. Part of the gas is stripped off the cloud to form a less dense and thin tail structure that follows the head with velocities lower than those of the cloud bulk motion (Konz et al. 2002; Heitsch & Putman 2009).

The cloud HVC 125+41-207 is prototypical for interacting HVC denoted accordingly as HT-HVC. Braun & Burton (2000) used the WSRT to study the small-scale structure of the CHVC. They found out that HVC 125+41-207 was characterized by an extremely narrow H I line unresolved by their spectral resolution of 2.47 $km\,s^{-1}$. The peak brightness temperature of this line is exceptionally high with T_B = 75 K indicating the existence of a cold and dense cold neutral medium (CNM) core. Their maps reveal a highly structured H I CNM distribution. Brüns et al. (2000) used Effelsberg observations of HVC 125+41-207 to deduce that this dense core is embedded within a warm neutral medium (WNM) envelope. Moreover, they found evidence that the WNM shows signs of deceleration not only towards the cloud's tail but also along the rims. Proportional to this deceleration of the radial velocity component, the WNM gets warmer (see their Fig. 2). Only the combined analysis of the WSRT and Effelsberg data allow the deduction of such a homogenous view of HVC 125+41–207 as an interacting CHVC.

To investigate the gaseous structures of HVCs and their dynamics accurately, the combination of radio interferometric and single-dish data is essential. Radio interferometers are insensitive to structures on the scale of tens of arc minutes and beyond but the single-dish WNM observations are unable to resolve the small-scale structure of the CNM. The combination of H I single-dish and interferometric observations provides the possibility of studying HVCs in the necessary detail.

In this chapter high-resolution H I observations of three CHVCs are presented, using the 100 m Effelsberg telescope and the WSRT. Section 5.2 presents the details of the data, and the H I observations are introduced. The combination method is discussed circumstantially in Chap.3, while the result of combination of two data sets is presented in Sec. 5.3.1 through Sec. 5.3.3. Section 5.3 discusses the physical and morphological properties of the clouds and the results of the Gaussian decomposition of the integrated spectral lines. Section 5.5 summarizes our findings and gives an outlook on future work.

5.2 Observations and data

All three CHVCs have non-symmetric shape, and specifically non-spherical shapes (see Fig. 5.2). The complex morphology of their appearance as seen with a single-dish telescope is elongated in their H I distribution; this has been interpreted as clear sign of a distortion by ram pressure of an ambient medium.

The single-dish observations of the three CHVCs were carried out in January 2000 with the 100 m Effelsberg telescope. The half power beam width (HPBW) of the Effelsberg data is ≈ 9′ (see Table 5.1 for observational details). Figure 5.2 shows the Effelsberg integrated flux maps of the clouds. All CHVCs exhibit a HT morphology with a pronounced core. To resolve these cores, radio interferometric observations were performed with the WSRT. Furthermore, the selected clouds have declinations of about +40° allowing for a complete 12-hour coverage with the WSRT. The combination of both low- and high-resolution data makes it possible to investigate the warm diffuse gas as well as the compact and cold structures in detail.

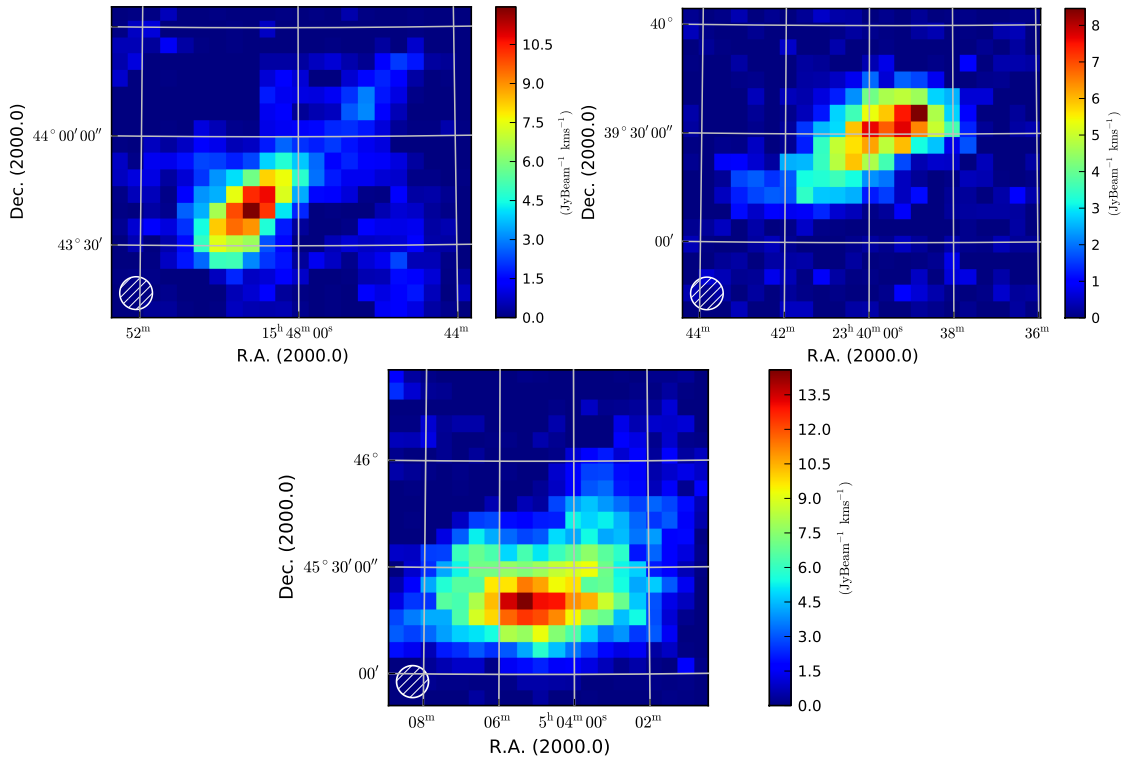The interferometric observations of the three CHVCs were carried out in November 2004 and May

Figure 5.2: CHVCs flux-density maps as observed with the Effelsberg 100 m telescope. Figure (a) presents CHVC 070+51-150, (b) CHVC 108-21-390, and (c) CHVC 162+03-186.

2005 in the maxi-short configuration with the WSRT. This setup provides good sensitivity on the short baselines as well as on a long baseline of 2.7 km. Each CHVC was integrated for 12 h in a single pointing on the sky centered on the maximum integrated intensity from the single-dish data. For each of the two polarizations the correlator provided a total of 1024 spectral channels across a bandwidth of 2.5 MHz, resulting in an intrinsic velocity resolution of about $0.5\,\mathrm{km\,s^{-1}}$ (Westmeier 2013, priv. comm.).

The data were reduced using the Astronomical Image Processing System (AIPS, Greisen 1990). The data reduction has been performed by T. Westmeier. A detailed description of process is presented by Faridani et al. (2014). The final noise levels towards the pointing centers are of the order of 1.5 mJy beam^{-1} of approximately 2×2 arcmin full width at half maximum (FWHM). The final velocity resolution of the data cubes is $5.2\,\mathrm{km\,s^{-1}}$ by averaging over 10 spectral channels, and the final channel width is $2.6\,\mathrm{km\,s^{-1}}$ by choosing an increment of 5 channels (Westmeier 2013, priv. comm.).

In radio interferometry, the final image is the representation of the sky as it is seen by the array convolved by the primary beam response of a single antenna. The response of the antenna can be modeled as a Gaussian, then divided out of the image (Sec. 2.1.4). This correction accounts for the lower sensitivity towards the edges of the primary beam. It should always be the last stage of the imaging process after the best-quality image is produced. Performing the correction at early stages leads to incorrect results (Fomalont 1989). After the primary beam correction (PBC) one finds enhanced noise at the edges of the image. However, the correction is indispensable for the estimation of the H I total flux density and H I mass. Figure 5.3 shows the interferometric and combined cube of CHVC 162+03-186 before and after the PBC. It emphasizes the need for an extended H I mosaic in order to obtain the complete census of the gas distribution in and around Galactic HVCs. A simple comparison reveals that the primary-beam corrected interferometric image of CHVC 162+03-186 (panel c) is only able to

(a) CHVC 162+03-186 Interferometer (npbc)

(b) CHVC 162+03-186 Combined (npbc)

(c) CHVC 162+03-186 Interferometer (pbc)
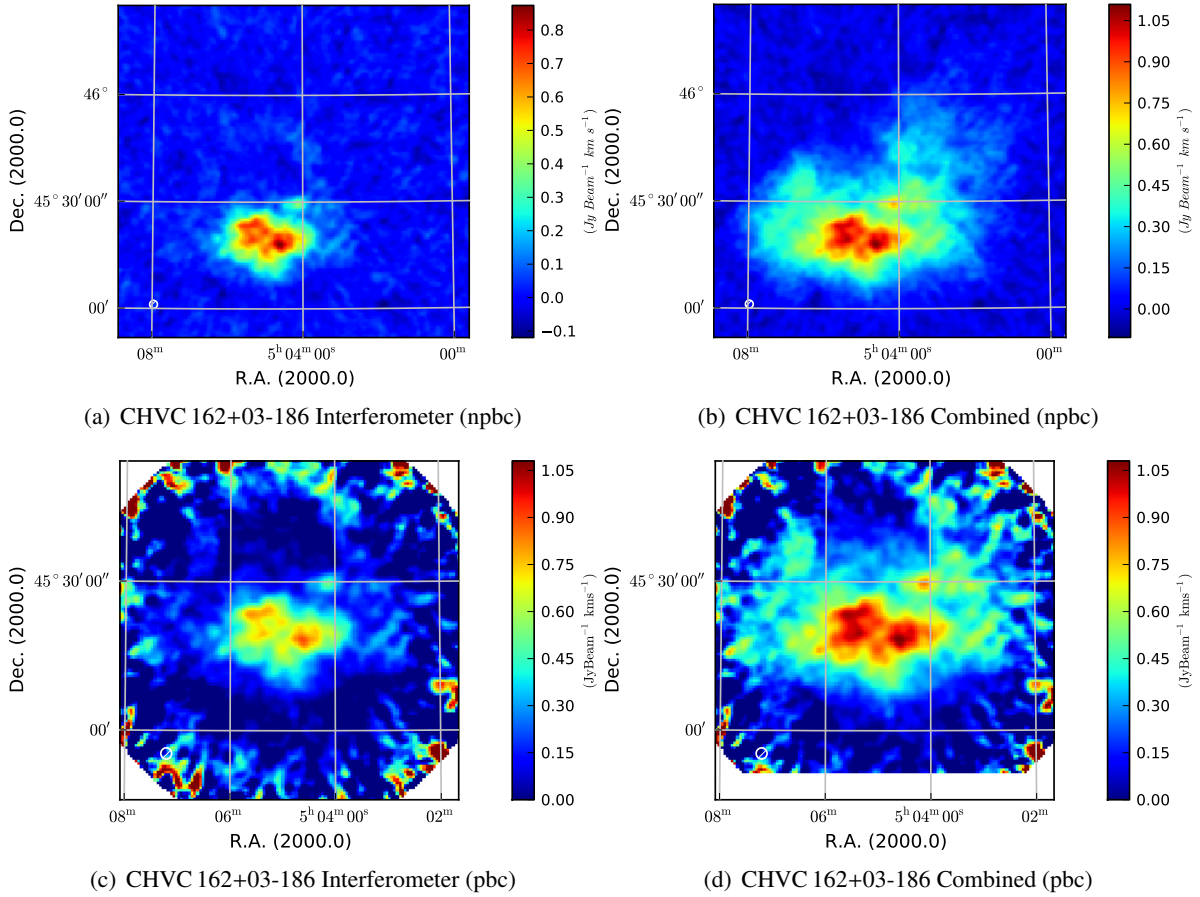
(d) CHVC 162+03-186 Combined (pbc)

Figure 5.3: Panels (a) and (b) show the interferometric and combined images of CHVC 162+03-186 before the PBC. Panels (c) and (d) show the same images after the PBC. The enhanced noise at the edges of the images is the result of PBC. A simple comparison reveals that a single pointing is only able to capture the central part of the cloud. Note that the figure is not available in the *A&A* publication. It has been added subsequently.

capture the inner part of the cloud, however the structure is much more extended and more pointings are required. For the following three CHVCs the PBC was performed using the Multichannel Image Reconstruction, Image Analysis And Display (MIRIAD, Sault et al. 1995) task `Linmos`.

Although the beam size of the single-dish Effelsberg data is constant at 9 arcmin, the WSRT synthesized beam varies in size according to the different source declinations. Hourangle coverage and visibility weighting schemes can also cause variation in the beam size (Chap. 4). In the case of the presented CHVCs the applied weighting scheme is the same, although there are variations in the hourangle coverage. Prior to the combination of both data sets, it is essential that they are reprojected onto the same grid. Regridding was performed within MIRIAD with the help of the `regrid` task. The regridded single-dish and the interferometric data cube are the inputs of the combination pipeline as introduced in Chap. 3.

For the three CHVCs both high-resolution (interferometer) and low-resolution (single-dish) data have been merged. The cleaned, primary beam corrected radio interferometric images and the single-dish data were combined in the image domain. The results of their combination are presented in Sec. 5.3.1 through Sec. 5.3.2. The combination allows us to recover both the complete flux (single-dish flux) and

Name	α (J2000)	δ (J2000)	V_{LSR}	Δv Eff/WSRT/comb.
(CHVC $l \pm b$)	[hh:mm:ss]	[dd:mm:ss]	[km s^{-1}]	[km s^{-1}]
CHVC 070+51	15:49:13	43:39:30	-150	5.15/2.57/2.57
CHVC 108-21	23:38:50	39:35:28	-390	2.57/2.57/2.57
CHVC 162+03	05:05:20	45:20:29	-186	2.57/2.57/2.57

Table 5.1: Observational details on the CHVCs. α is the right ascension, δ the declination, V_{LSR} the local standard of rest (LSR) velocity, and Δv is the spectral channel resolution of Effelsberg, WSRT and combined data.

the highest angular resolution (interferometer).

5.3 Compact high-velocity clouds

The term CHVC was defined by Braun & Burton (2000). The designation CHVC or HVC is an indication of the characteristics of the clouds. HVCs are associated with more extended complexes, whereas CHVCs are small compact objects, well separated from the complexes. CHVCs usually have angular sizes smaller than 2°, although different isolation criteria also exist. In any case, the velocity of the cloud is a strong argument in favor of its being part of a structure rather than being isolated (Putman et al. 2011).

All three of the CHVCs observed have a rather complex and irregular morphology. Figure 5.2 shows the Effelsberg observations of the CHVCs, where it can be seen that CHVC 070+51-150 and CHVC 108-21-390 both exhibit a pronounced HT structure. CHVC 162+03-186 is a so-called bow-shock shaped CHVC (Westmeier et al. 2005b). The asymmetric appearance of the three CHVCs suggests a possible interaction with the ambient medium. All radial velocities of the three clouds are negative in LSR (see Table 5.1). Negative radial velocities mean that the clouds are receding.

In Fig. 5.4 the positions of the three clouds are marked in the global HVC map generated from the Leiden/Argentine/Bonn Galactic H I Survey (LAB, Kalberla et al. 2005). Additionally, the velocity distribution map of the high-velocity sky is presented for a comparison of the clouds' velocities with their surrounding structures. The arrows present an estimate of the projected direction of motion on the sky based on the ratio of brightness temperature T_{B} over kinetic temperature T_{kin}.

CHVC 070+51-150 is located between complexes C and K. Complex C is located at a distance $\geq$ 6 kpc (Thom et al. 2008; Wakker 2004; Kalberla & Haud 2006). Kalberla & Haud (2006) present some evidence of the possible existence of multi-component structures. CHVC 070+51-150 seems to be an isolated CHVC. Its radial velocity agrees with the presented radial velocities for complex C and K ($V_{\mathrm{LSR}} \approx$ -150 km s^{-1}). CHVC 162+03-186 is located in the direction of the anti-center shell (ACS, Kulkarni & Mathieu 1986). It is not fully isolated and is probably associated with the ACS. The measured radial velocity of the cloud agrees with the presented velocities in this region. The measured radial velocity of -186 km s^{-1} is in agreement with the velocity ranges of the anti-center very high-velocity clouds (ACVHVC) reported by Kalberla & Haud (2006). For this complex both distances and metallicities are unknown.

CHVC 108-21-390 is located at the position of the EN complex. In fact, the cloud is listed and shown by Braun & Thilker (2004). It sits right on top of the Magellanic stream and has the same velocity as the surrounding stream clouds. The notation EN population is derived from the extremely negative (EN) radial velocities measured at this region. According to Wakker (2004) the EN population is located at a

distance of ≈ 50 kpc. The aforementioned distances are useful to derive further physical properties of the three HVCs. In particular, the distance is essential for the estimation of their H I masses.

In Figs. 5.5 - 5.8, different data sets for each cloud as well as the combined data and a intensity weighted velocity map are shown. It is important to note that the top-left panel in each figure presents the regridded and reprojected Effelsberg data cropped to the same field of view (FoV) as in the interferometric and combined maps. It is clear that WSRT single-pointing observations only cover the clouds partially, whereas the Effelsberg observations in Fig.5.2 show the entire extended structure of the clouds down to the observational detection limit. Therefore, the single-dish data cubes are used for the determination of the velocity distribution.

To derive the projected motion of the clouds in the sky, the method of Venzmer et al. (2012) has been applied. The ratio of brightness temperature T_B over kinetic temperature T_{kin} has been calculated. CNM structures will show up with high T_B and correspondingly large ratios, while WNM gas is characterized by high T_{kin} values and low ratio values on the map. It is important to mention that the value of T_{kin} is derived from the H I linewidth. In this case, the derived value is not the actual kinetic temperature, but only an upper limit, since additional turbulence broadening will have contributed to the linewidth. Hence, the values of T_B/T_{kin} are to be considered lower limits. In the gradient map, the pixel with highest value represents the center of density.

Additionally, the intensity maximum has been determined in the gradient map. An arrow connects the brightness temperature maximum (arrow head) and the centre of the projected intensity distribution. Its direction indicates the projected motion on the sky based on the ratio of T_B over T_{kin} (Fig. 5.4, top panel).

In the case of CHVC 070+51-150 the arrow's head and its end point are not significantly separated and in fact it is narrower than the synthesized beam (Fig. 5.5, panel e). However for both CHVC 108-21-390 and CHVC 164+03-186 the difference between both locations is substantially more extended than the beam size (Figs. 5.7 and 5.8, panel e). In any case, for all three clouds, the arrow points in the direction of the disk (Fig. 5.4). Additionally, a comparison between Figs. 5.2 and 5.4 shows that the arrows lie in the direction of the HT Structure.

5.3.1 CHVC 070+51-150

Figure 5.5 comprises different representations of CHVC 070+51-150 data. Panel (a) shows the regridded Effelsberg H I 21 cm flux-density map, panel (b) the corresponding WSRT map, panel (c) the flux-density map of the combination, and panel (d) the color-coded first-moment map. The presented intensity weighted (radial) velocity distribution allows the study of overall velocity distribution across the cloud. For CHVC 070+51-150 the estimated velocity gradient is about 15 km s^{-1} with a spectral resolution of 5.15 km s^{-1} (see Table 5.1)

The WSRT data offers a synthesized beam of $\approx 2' \times 2'$. The combined data cube has the same high angular and spectral resolution as the interferometric data set. The root mean square (RMS)[2] in the WSRT cube is 1.4 mJy beam^{-1}, which is slightly lower than in the combined data (1.6 mJy beam^{-1}, see also table 5.2).

CHVC 070+51-150 exhibits a distinct HT structure. A remarkable feature of this cloud is the enveloping faint H I emission, obvious in particular along the major axis of the cloud, which can be seen clearly in the single-dish image (Fig. 5.2, top panel).

The measured velocity gradient of about 15 km s^{-1} (the tail region is slightly slower) present in the first-moment map supports an interaction scenario. The small structures around the cloud and particu-

---

[2] The RMS values are measured in the data cubes, which are not primary beam corrected.
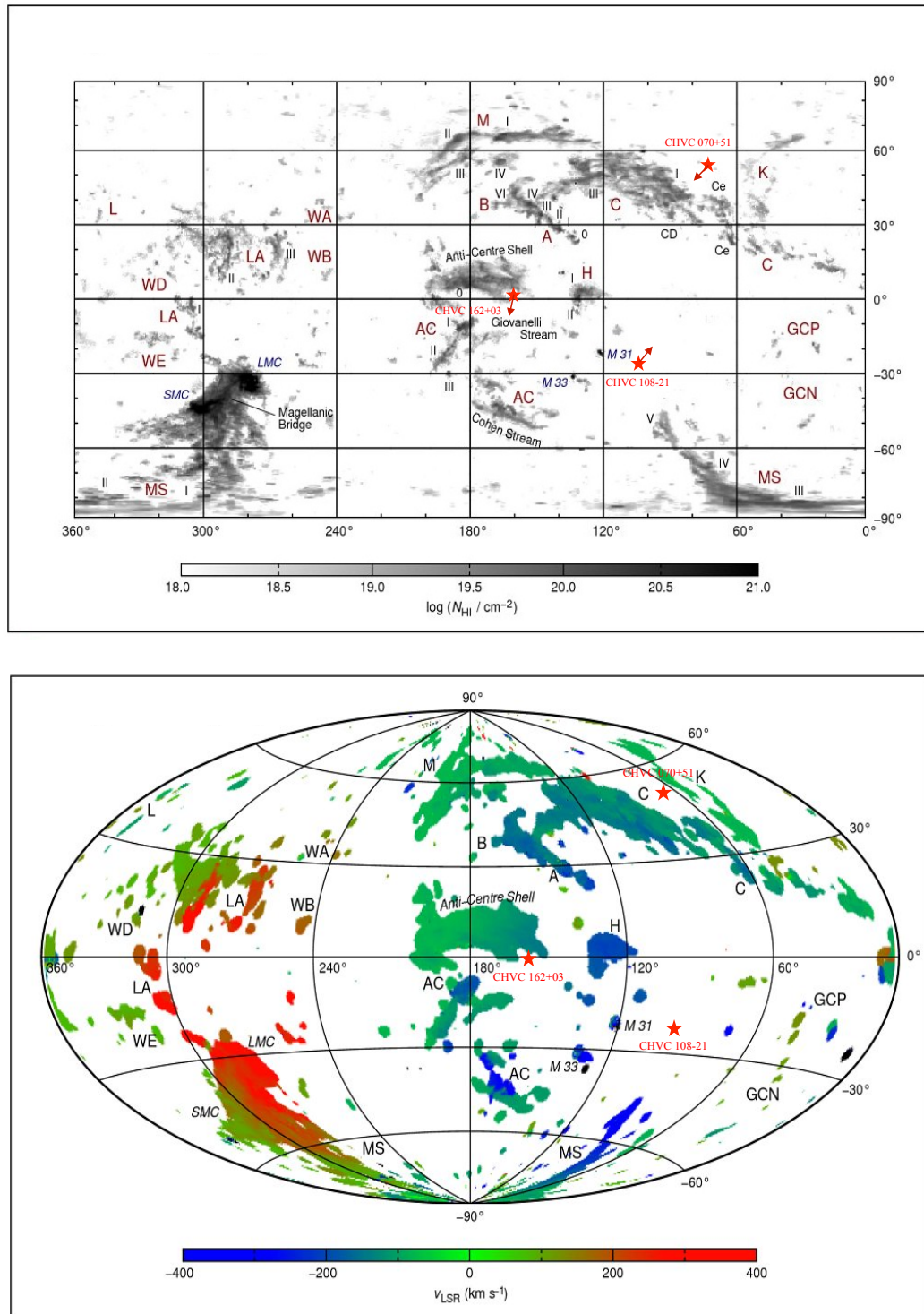
Figure 5.4: The high-velocity sky based on the LAB survey. The figure at the top shows the location of the three CHVCs. The arrows indicate the projected motion direction on the sky based the ratio of brightness temperature T_B over kinetic temperature T_{kin}. The bottom figure shows the velocity distributions of the surrounding structures. Background picture credit: Tobias Westmeier.
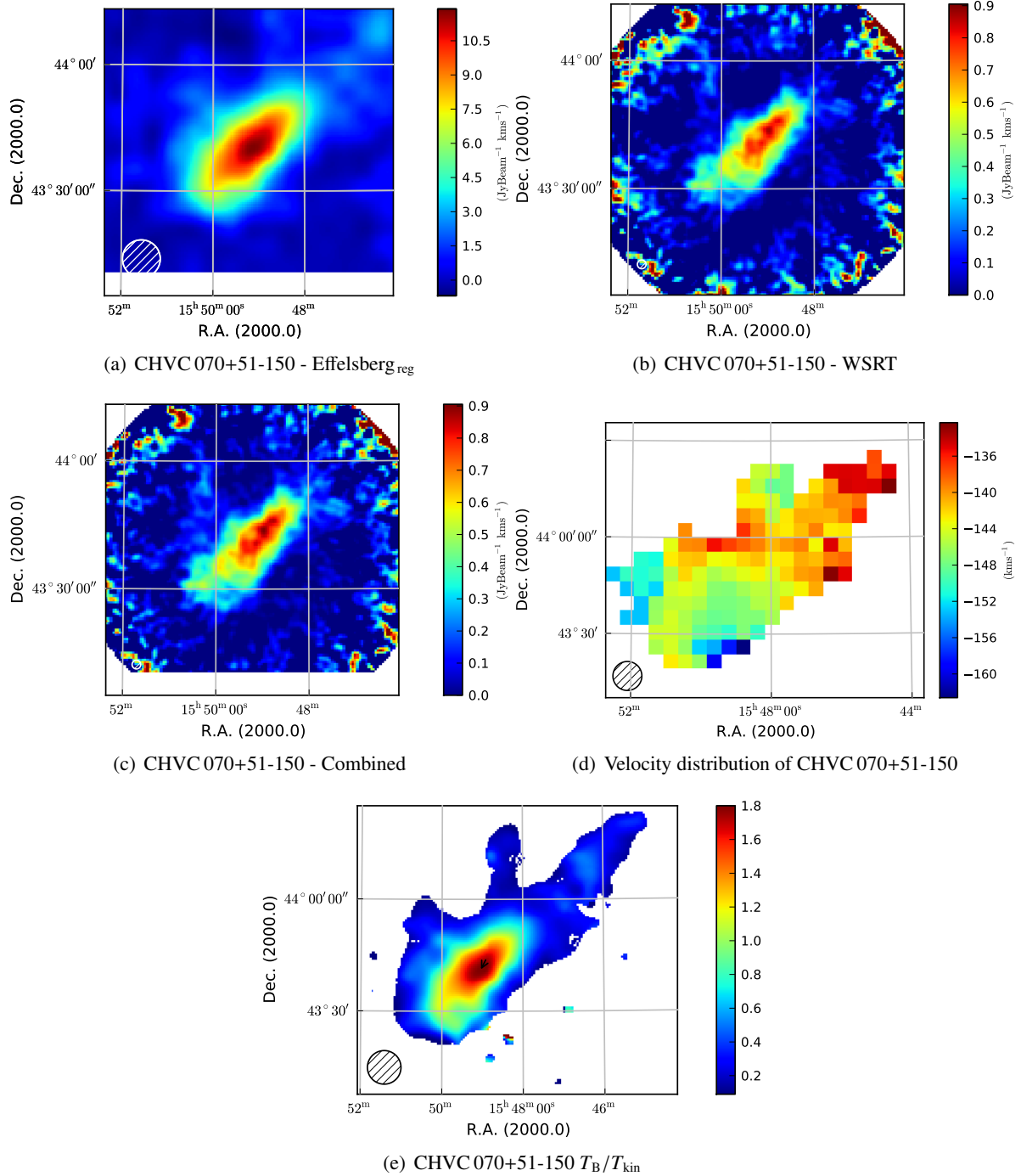
(a) CHVC 070+51-150 - Effelsberg$_\mathrm{reg}$

(b) CHVC 070+51-150 - WSRT

(c) CHVC 070+51-150 - Combined

(d) Velocity distribution of CHVC 070+51-150

(e) CHVC 070+51-150 $T_\mathrm{B}/T_\mathrm{kin}$

Figure 5.5: Maps of CHVC 070+51-150. (a) regridded flux density map of the Effelsberg data, (b) flux-density map of the WSRT data, (c) the combined flux density map, and (d) velocity distribution of CHVC 070+51-150. The measured velocity gradient in the Effelsberg data cube is about 15 km s^{-1} with a spectral resolution of 5.15 km s^{-1}. (e) presents the ratio of peak brightness temperature T_B over the kinetic temperature T_kin. The arrow connects the brightness temperature maximum (arrow head) and the center of the projected mass distribution.

larly in the northwest region of the cloud have radial velocities slightly lower than the cloud bulk motion, suggesting the cloud structure results from ram pressure interaction.

Table 5.1 summarizes the observational results for CHVC 070+51-150, while Table 5.2 lists the physical properties of the cloud. In the case of primary beam corrected interferometer data, there exists a limited FoV, which does not cover the whole cloud. This is necessarily also the case for the combined data. For a strictly fair comparison of the interferometer with the single dish, only the region of overlap is considered, since the single-dish map is considerably larger than the interferometric map. The flux determination and comparison should also be handled with care. In order not to choose any artificial cutoffs, the flux is measured from the center of the pointings in ever larger radii (see Fig. 5.6). The dashed line marks the HPBW of the WSRT. The results reveal that in the outer regions dominated by diffuse gas, the interferometer misses flux, and its curve flattens out before it is dominated by noise. This shows that for the presented objects the interferometer observations hardly measure flux in the regions dominated by low temperature emission.

Figure 5.6 (top left) shows the result of CHVC 070+51-150, where the blue line gives the values for the combination, the green line represents the WSRT values, and the red line the Effelsberg values. The dashed vertical line at 18.5 arcmin marks the boundary of the primary beam of the WSRT (effective beam size is $\approx 37'$).

The course of the curves can be explained as follows: the high density clumps are concentrated mainly in the central part of the cloud. Accordingly, the radio interferometric map exhibits higher brightness temperatures than the single dish. For larger radial distances from the pointing center there is more diffuse gas and therefore, the values in the single-dish and combined cubes are higher. The total flux in the combined map is quantitatively consistent with the total flux measured with the Effelsberg telescope. The dashed line marks the HPBW of the WSRT. About 20% more flux has been detected by the single-dish telescope than by the radio interferometer. This result indicates that a significant fraction of the cloud consists of diffuse extended H I missed by the interferometer as a result of its insensitivity at the lowest spatial frequencies.

5.3.2 CHVC 108-21-390

Figure 5.7 presents the corresponding flux density and first-moment map of CHVC 108-21-390. Table 5.1 summarizes the basic parameters of the data set while Table 5.2 compiles the derived cloud properties. The WSRT synthesized beam is about $2.9' \times 1.9'$ in size. This is also the angular resolution of the combined H I data.

The velocity distribution of CHVC 108-21-390 indicates bulk velocities of about -400 km s^{-1}, which approaches the upper limits of the velocities measured for HVCs (Wakker 2004; van Woerden et al. 2004). The head of the cloud is located at the northwest and the lower flux density tail is located at the southeast (Fig. 5.7, panels a and c). The faint diffuse gas at the southeast edge is visible indistinctly in the interferometer map (Fig. 5.7, panel b), yet it can be seen clearly in both single-dish (panel a) and combined data (panel c). The major axis of the cloud is approximately 1°, while the minor axis is about 0.3° (see table 5.2). The velocity distribution indicates a velocity gradient of about 10 km s^{-1}, where the gas in the tail area is slower (see Fig. 5.7 with the slower gas located in the tail). After the combination, a difference of $\approx 40\%$ with respect to the total fluxes in the interferometric and combined data has been measured (Fig. 5.6, middle panel). The difference of the total flux in single-dish and radio interferometer reveals that almost half the cloud largely consists of diffuse extended H I emission, which is missed by the WSRT.
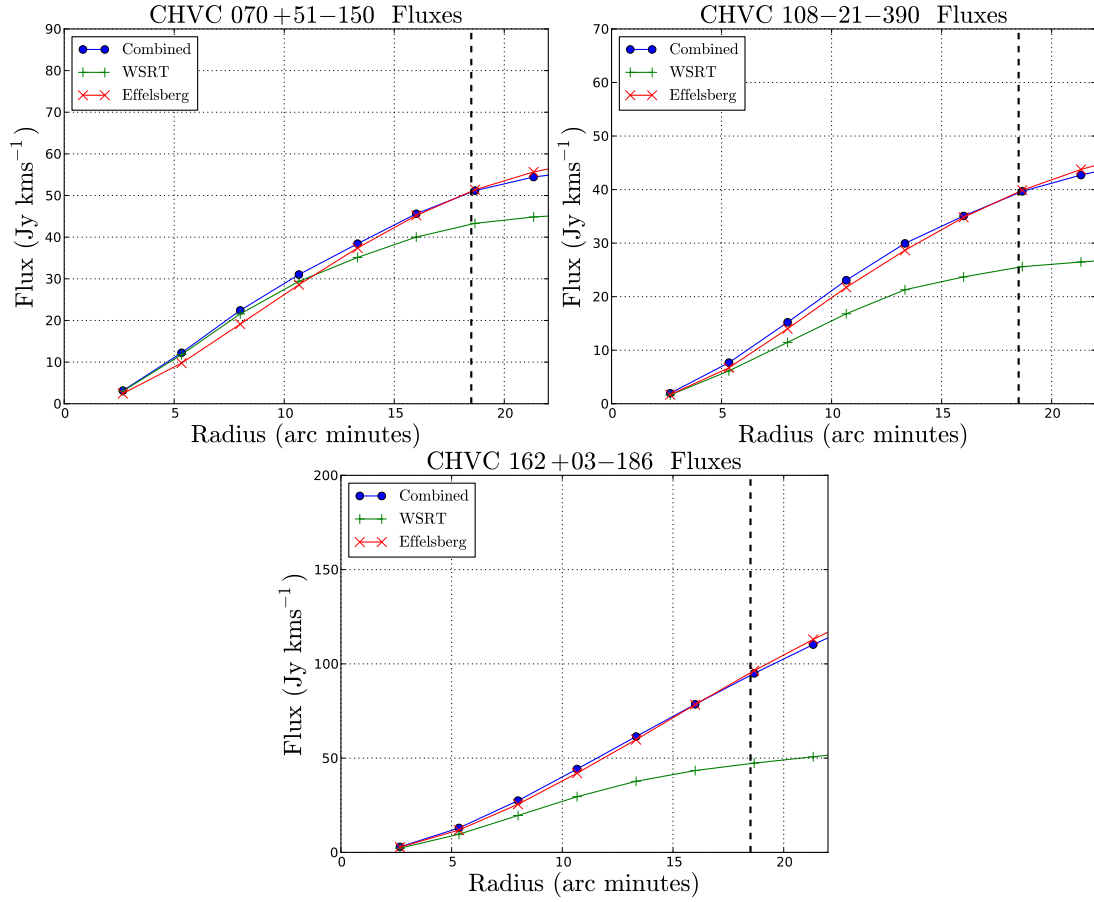
Figure 5.6: Measured cumulative fluxes as a function of radial separation from the centre of the maps. *The top-left panel* presents the results of radial profiles for CHVC 070+51-150, *the top-right panel* for CHVC 108-21-390, and *the bottom panel* for CHVC 162+03-186. The blue line represents the measured fluxes for the combination, the green line the values for the WSRT, and the red line for the Effelsberg data. The dashed line marks the HPBW of the WSRT. In all three cases the measured flux after the combination is in good agreement with the measured value from the single-dish data. In the case of CHVC 070+51-150, about 20% more flux has been detected by the single-dish than by the radio interferometer. The difference between the combined and interferometric data is ≈ 40% for CHVC 108-21-390. For CHVC 162+03-186, the ratio of interferometric/combination accounts for almost 50%. This is the largest measured ratio for the three CHVCs. It also reveals that a large portion of the cloud consists of WNM, which is traced best by the single-dish. The results demonstrate that the combination achieves the expectations.

(a) CHVC 108-21-390 Effelsberg$_{\text{reg}}$

(b) CHVC 108-21 WSRT

(c) CHVC 108-21 Combined

(d) Velocity distribution of CHVC 108-21-390

(e) CHVC 108-21 T_B/T_{kin}
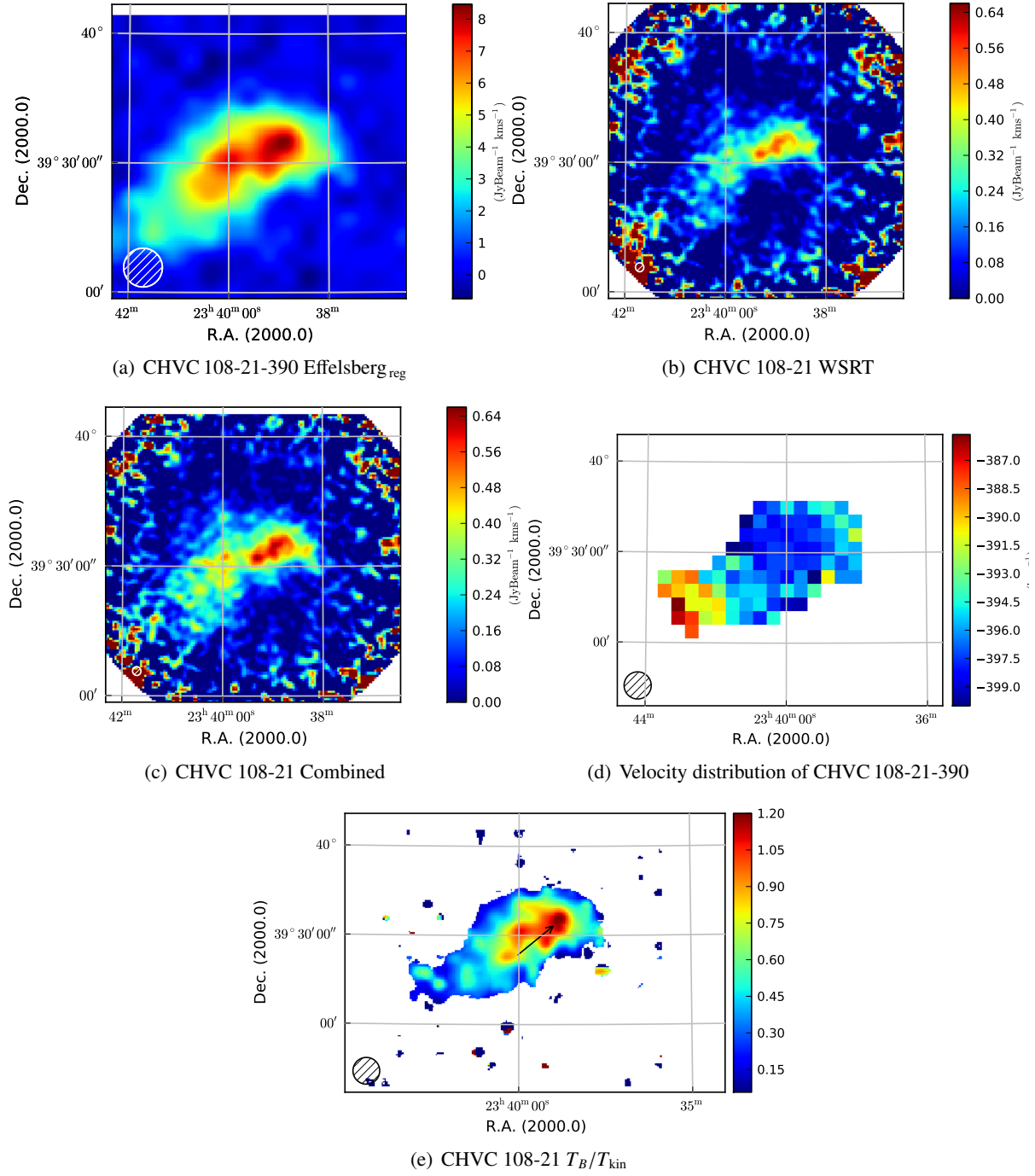
Figure 5.7: Maps of CHVC 108-21-390. (a) is the map of the regridded Effelsberg data, (b) the WSRT data, (c) the combined data, and (d) the velocity distribution of CHVC-108-21. The measured velocity gradient within the cloud is ≈ 10 km s^{-1} with a spectral channel width of 2.57 km s^{-1}. (e) presents the ratio map of T_B over T_{kin}. The arrow connects the brightness temperature maximum (arrow head) and the center of the projected mass distribution. This is thought to represent an estimate of the projected direction of motion on the sky.

5.3.3 CHVC 162+03-186

Figure 5.8 presents the H I maps of CHVC 162+03-186 and is arranged as the previous figures. Table 5.2 compiles the observational parameters, while Table 5.1 summarizes the derived physical properties. Westmeier et al. (2005b) found that CHVC 162+03-186 has a bow-shock shape. The bow-shock might be the result of interactions between the cloud and the gaseous halo. For the WSRT data the synthesized beam is $2.2' \times 2.1'$. The combined map has the same angular and spectral resolution as the WSRT data. Panel (d) of Fig. 5.8 displays the velocity distribution of CHVC 162+03-186. It shows velocities of ≈ -180 km s^{-1}. The slower gas is located mostly at the eastern edge of the cloud. There are two distinct regions, separated spatially, that have higher velocities of about -190 km s^{-1}.

Figure 5.6 shows the cumulative fluxes of the three data sets against the concentric rings from the center of the map. Again the dashed line indicates the primary beam of the WSRT. A comparison between measured total flux reveals a $\approx 50\%$ higher total flux density in the combined data than in the interferometric data. This large difference suggests the existence of a substantial amount of broadly distributed diffuse gas in CHVC 162+03-186.

Name	Peak T_B	Peak $N_{H I}$	minor x major ext. comb.	WNM Eff/WSRT/comb.
	[K]	[10^{19} cm^{-2}]	[°]	[km s^{-1}]
CHVC 070+51-150	1.1	4.5	0.2 x 3.3	22.8/19.2/19.6
CHVC 108-21-390	0.7	3.2	0.3 x 1.0	21.4/17.4/17.2
CHVC 164+03-186	1.4	5.5	0.6 x 1.6	22.5/19.2/18.6

Table 5.2: Physical properties of the CHVCs. Peak T_B is the peak brightness temperature; peak $N_{H I}$ denotes the maximum column density; major and minor are the angular extent of the clouds; and WNM is the FWHM of the gaseous components in the combined data. The quantities are given separately for the Effelsberg, WSRT, and combined data.

5.3.4 Gaussian decomposition

HT clouds often show a two-phase medium (Brüns et al. 2000; Westmeier et al. 2005a; Ben Bekhti et al. 2006). In the case of the CHVCs under consideration, the small-scale structure detected by the radio interferometer might also trace denser and probably cooler gas. A two-component Gaussian decomposition of the H I data is a useful approach to separate quantitatively these two gas components, where the narrow linewidth corresponds to the CNM with high volume densities and the broad linewidth to the low density WNM regions.

To evaluate the relative amount of H I in the warm and cold gas phase, average profiles for each CHVC have been created. Because of the intrinsic velocity gradient, a simple sum over all spectra would yield an artificially broadened H I line spectrum. To account for this, a technique similar to the recently introduced super profiles by Ianjamasimanana et al. (2012) has been used. Each line of sight that has at least six channels above the 3-σ level is fitted with a Gauss-Hermite polynomial to robustly determine the radial velocity of the peak of the H I profile. The individual profiles are then shifted to a common radial velocity and summed. The resulting super profile is then fitted with a two-component Gaussian to estimate the relative abundance of the cold and warm phase, i.e. the ratio of the areas of the two Gaussian components.

Table 5.2 summarizes the results of the Gaussian decomposition for all three CHVCs. The results of the Gaussian decomposition are also presented in Fig. 5.9. The solid green line close to the data points

(a) CHVC 162+03-186 Effelsberg$_{\text{reg}}$

(b) CHVC 162+03 interferometer

(c) CHVC 162+03 combined

(d) Velocity distribution of CHVC 162+03-186
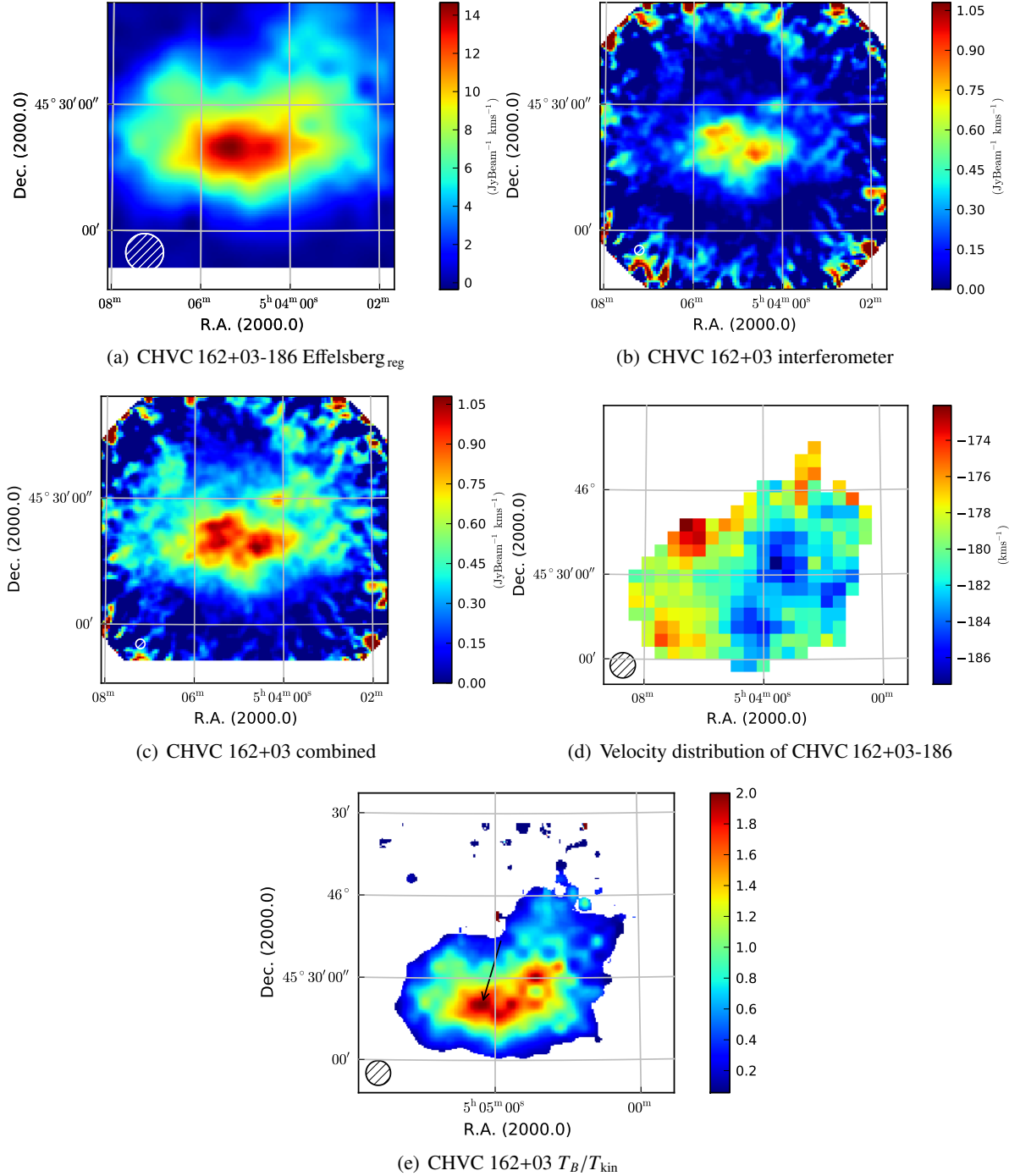
(e) CHVC 162+03 T_B/T_{kin}

Figure 5.8: Maps of CHVC 162+03-186, (a) the regridded Effelsberg data, (b) flux-density map of the WSRT data, (c) the combined flux-density map, and (d) is the flux-weighted velocity distribution with a gradient of ≈ -180 km s^{-1} and a spectral channel width of 2.57 km s^{-1}. (e) displays the ratio of T_{B} over T_{kin}. The arrow connects the brightness temperature maximum (arrow head) and the center of the projected mass distribution. This is thought to represent an estimate of the projected direction of motion on the sky.

(filled circles) traces the WNM, while the small Gaussian in solid red represents the CNM. The super profile H I spectra have been renormalized. The x-axis presents the relative radial velocities in km s^{-1} in the super profile while the mean velocity is shifted to zero. The left panels present the results of the Gaussian decomposition for the combined data sets. The middle panels and the right panels present the same values for the WSRT data and Effelsberg data, respectively.

For all three CHVCs, only warm gas without any evidence of a CNM has been found (see Fig. 5.9). Kalberla & Haud (2006) detect rather broad lines for the ACVHVC, which agrees with the results. Only in the case of CHVC 108-21-390 there is marginal evidence of a second, cold gas component; yet it is intriguing to find no evidence for a CNM in any of the clouds. One possible interpretation could be that for these three clouds the interaction is not particularly strong owing to a combination of low velocity of the clouds relative to their environment and/or a low density of the ambient medium. In this case, the density within the core might not rise high enough to allow sufficient self-shielding and cooling of the gas. Some support for this could come from the morphology of the clouds: both CHVC 070+51-150 and CHVC 162+03-186 have their core relatively close to the center of the bulk of the H I emission, rather than near the leading edge as one would expect for a strongly interacting cloud. The only exception is CHVC 108-21-390. Its core is clearly shifted towards the presumed leading edge, and interestingly this is the only cloud that does indeed show some evidence of cold gas according to the Gaussian fits.

In addition to the weak evidence of a CNM, CHVC 108-21-390 has the narrowest lines of the three clouds. According to Wolfire et al. (1995b), a single component gas implies an upper limit for the density of $\approx 0.3\,\text{cm}^{-3}$. The single warm gas component derived from the analyses of the H I super profiles implies Doppler temperatures of about $T_\text{D} = \frac{m_H\,(\Delta v)^2}{8\,k\ln 2} \simeq 21.8 \times (22\,\text{km s}^{-1})^2 \simeq 10.000\,\text{K}$. Using the derived Doppler temperature, an upper limit for the pressure of about $\approx 3300\,\text{K cm}^{-3}$ has been calculated, which is in agreement with the upper limit for a single-phase medium given by Wolfire et al. (1995b, panel (e) of their Fig.1). The parameter distance in the corresponding position in the phase diagram is completely degenerated, i.e., a cloud with the above parameters is always a simple, warm medium, regardless of distance. The physical parameters are also consistent with the ones from a cloud in thermal equilibrium with the ambient (halo) gas. This would support the proposal that the ram pressure interaction may play only a minor role because of the relatively slow movement of the cloud, as suggested before.

5.4 HVCs in their environment

The location of HVCs in the Galactic halo as well as their interaction with their ambient environment have a strong impact on their morphology and appearance (Putman et al. 2012; Kalberla & Kerp 2009). Depending on the distance from the Galactic disk, different mechanisms dominate the evolution of the clouds (Wolfire et al. 1995a,b).

A detailed study of the incidence of hot and cold components was done by Wolfire et al. (1995a,b). Kalberla & Haud (2006) also did a comprehensive study of two-component gas, showing that the presence of cold gas components varies between different HVC complexes. Furthermore, Wolfire et al. (1995a) investigated the stability of H I gas in the Galactic halo as well as the effect of dust-to-gas ratio and metallicity. They argue that the two-component gas can be used as an indicator to constrain the origin and possibly the distance to the clouds.

It was originally proposed by Field et al. (1969) that cosmic rays (CR) are the dominant heating process; however, successive analyses, (e.g., Wolfire et al. 1995a) have revealed that photoelectric (PE) heating is much more efficient than heating by X-ray (XR) and CR. The latter authors discuss the amount of energy transported in the form of heating and cooling processes as a function of density n. According

(a) CHVC 070+51-150 combined   (b) CHVC 070+51-150 WSRT   (c) CHVC 070+51-150 Effelsberg$_{reg}$

(d) CHVC 108-21-390 combined   (e) CHVC 108-21-390 WSRT   (f) CHVC 108-21-390 Effelsberg$_{reg}$

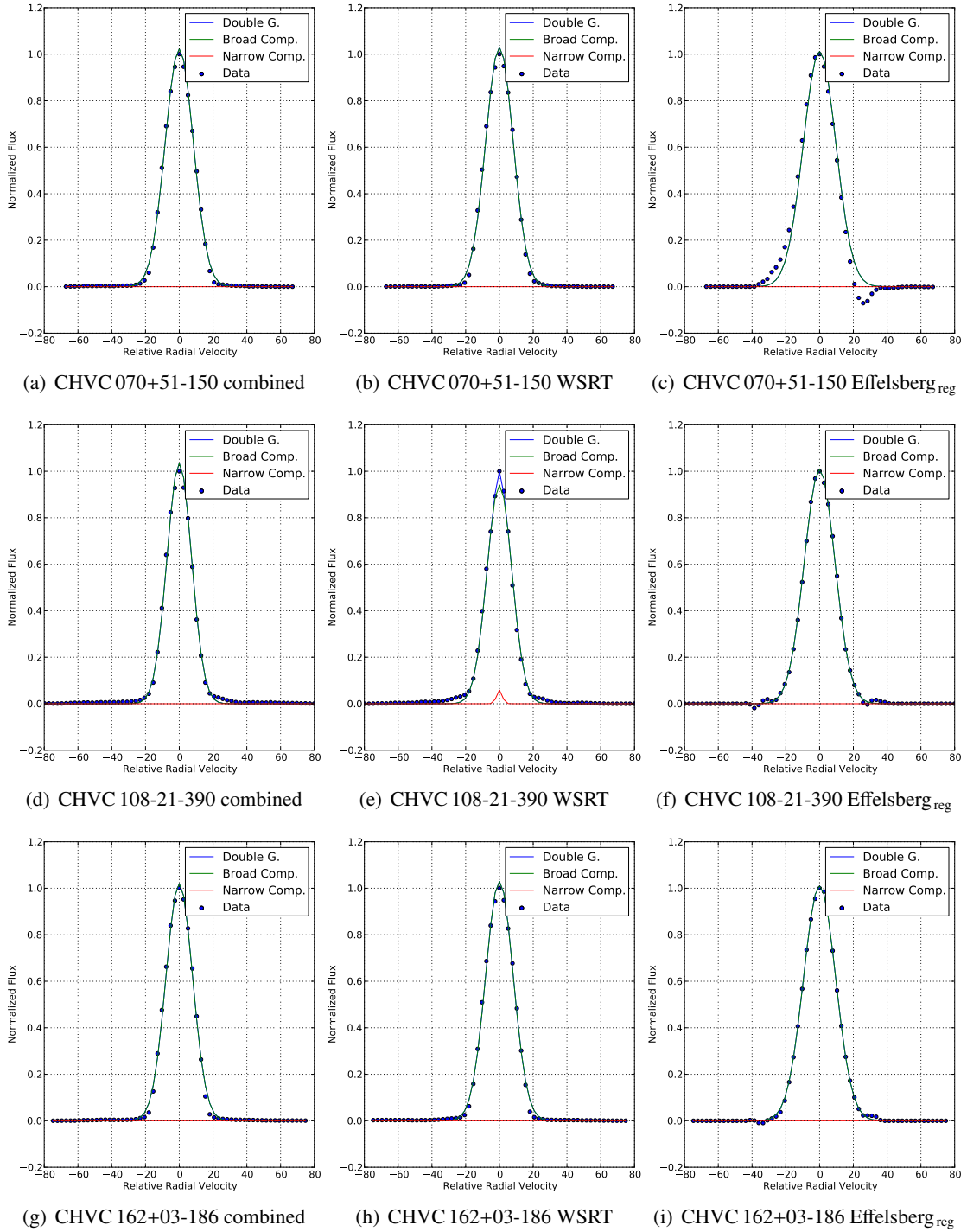(g) CHVC 162+03-186 combined   (h) CHVC 162+03-186 WSRT   (i) CHVC 162+03-186 Effelsberg$_{reg}$

Figure 5.9: Super profiles of the three CHVCs. The first row presents the results of CHVC 070+51-150. The middle row shows the results of CHVC 108-21-390 and the bottom row of CHVC 162+03-186. The left panel displays the result of the Gaussian decomposition for the combined data. The middle and right panels present the results for the WSRT and Effelsberg data respectively. The green line corresponds to the broad component (WNM) and the red line to the narrow component (CNM).

to their Fig. 3 (panel b), PE is the most efficient heating factor, regardless of n. Although for lower energy levels CR and XR are more dominant, electron recombination onto small grains and Lyα are more dominant cooling processes at densities $\leq 0.1\,\mathrm{cm}^{-3}$. Regarding the cooling, CII fine-structure cooling gains more importance at higher densities of $n \geq 1\,\mathrm{cm}^{-3}$, while OI fine-structure cooling drops rapidly for $n \geq 1\,\mathrm{cm}^{-3}$. At higher densities ($n \geq 2\,\mathrm{cm}^{-3}$) both fine-structure transitions of CI (CI* and CI** at 307 and 609 μm) are the dominant cooling processes. However, the given density ranges for these processes are far beyond the expected densities of the HVCs. Hence, these two fine-structure transitions are irrelevant in the cooling process of HVCs.

For the HVCs the amount of H I in the clouds rises for higher distances to the galaxy, either as warm or as cold components or even as a mixed form. The reason for this is that the amount of XR and CR decreases with the distance to the galaxy. These are the main heating sources for the CHVCs, since PE does not play a major role in the heating process of them as a result of the lack of dust in the clouds (Wakker & Boulanger 1986).

Gas cools quicker, when it is sufficiently shielded from external radiation and efficient cooling mechanisms are provided. The cooling efficiency depends on the temperature and density of the gas (Eq. 5.2). In general, H I can only be efficiently cooled down at low temperatures of $T \leq 300$ K (Wolfire et al. 2003). The physical state of the gas, e.g., its temperature and degree of ionization depends on the heating and cooling efficiencies. Wolfire et al. (1995b) discuss the effect of gas density on cooling processes circumstantially. It is necessary to note that Wolfire et al. (1995a) treated the neutral gas phase of the interstellar medium (ISM) of the Milky Way. One should be cautious in transferring this to HVCs, since the conditions in the disk of the Milky Way with respect to density, radiation field, metallicity, etc. differ from those of the HVCs (Westmeier 2014, priv. comm.).

It is very important to mention that the model used in these publications assumes that the clouds are spherical. This is not always a valid assumption since the appearance of the cloud varies strongly as a result of ram pressure and turbulence. However, the results of their study provide a general idea of the ongoing processes, which affect the gas in and around the clouds. Their Figure 1 shows pressure and density conditions under which warm or cold gas is formed as a function of metallicity, dust-to-gas ratio, and distance from the Galactic disk .

Furthermore, Wolfire et al. (1995a) show that a two-phase gas can only be observed at higher densities ($n \geq 1\,\mathrm{cm}^{-3}$), while at lower densities only a WNM exists (panel (d) of their Fig. 3). According to the same figure, the amount of ionized gas as a function of hydrogen density n drops strongly from lower to higher densities. Furthermore, it is proposed that at least 1 particle/cm^{-3} is required in order to have the transition from warm to cold medium, which is not always the case in HVCs.

With respect to the strength of the external radiation field, the further away a HVC is from the disk of the galaxy, the weaker is the radiation field of the galaxy, so that the gas is heated less allowing for efficient cooling even at lower density. According to Draine (2011), the dominating heating process in the Milky Way is the emission of photoelectrons by dust grains, where photoelectric heating power as a function of volume is proportional to the dust density (for further information see Eq. (30.6) presented by Draine 2011).

Regarding gas density, the denser the gas is, the better is the protection from UV radiation from the Milky Way and external galaxies. The density is determined by the ambient density in the Galactic halo, if one assumes pressure equilibrium between HVC gas and halo gas. Finally, the metallicity plays a major role in the efficiency of cooling processes.

Overall, H I emission does not contribute significantly to the cooling. The main cooling processes are various fine-structure transitions of carbon and oxygen. Their efficiency, in turn, depends on the temperature and the density of the medium. Consequently, high-metallicity gas cools more efficiently than low-metallicity gas.

Kalberla & Haud (2006) present the following equilibrium equation for cooling and heating:

$$\Gamma_{pe} + \Gamma_{X-ray} = \Lambda_{e,CII} + \Lambda_{H,CI} + \Lambda_{Ly\alpha} \tag{5.1}$$

Γ_{pe} denotes the photoelectric heating by dust grains; Γ_{X-ray} describes the heating by soft X-rays; $\Lambda_{e,CII}+\Lambda_{H,CI}$ is cooling by collision between electrons and ionized carbon and between neutral hydrogen and neutral carbon atoms, respectively. Furthermore, they argue that the cooling efficiency depends on environmental conditions and the ratio of carbon to dust grains. They estimate a cooling timescale for both gas phases, CNM and WNM, as a function of volume density described through:

$$t_{cool} \approx 460 \, yr \, \frac{T \, [K]}{n \, [cm^{-3}]} \tag{5.2}$$

where n is the volume density of all existing hydrogen atoms and ions and T denotes the temperature of the gaseous phase. Table 5.3 summarizes the observational parameters for both phases of atomic H I; CNM and WNM (Lequeux 2005). According to Table 5.3 for CNM, $t_{CNM} \approx 1.4 \cdot 10^5$ yr, and for WNM one gets $t_{WNM} \approx 4.6 \cdot 10^7$ yr (Kalberla & Haud 2006).

Phase		Density [cm^{-3}]	Temperature [K]	Total mass [10^9 M$_\odot$]
Atomic (H I)	Cold	≈ 25	≈ 100	1.5
	Warm	≈ 0.25	≈ 8000	1.5

Table 5.3: The observational parameters of two phases of H I as suggested by Lequeux (2005).

Another important factor about the HVCs is their appearance and morphology. For the HVCs, it is common to observe WNM. However, some clouds show evidence of both the diffuse warm envelope and the cold compact clumps. The gas can be compressed by interaction with the surrounding medium, whereby the density increases and the cooling becomes more efficient. This effect is responsible for the cold cores in interacting HVCs (Heitsch & Putman 2009). Therefore, different observed gas components yield conclusions about the environment in which the cloud resides and which of the aforementioned processes come into effect.

Yet, the fundamental barrier is estimating the distance, as it is very difficult to find suitable background sources for indirect distance constraint, hence, the mass and environment of the high-velocity clouds are mainly unexplored. Various numerical and hydrodynamical simulations (Santillán et al. 1999; Quilis & Moore 2001; Konz et al. 2002; Heitsch & Putman 2009; Diaz & Bekki 2012; Plöckinger & Hensler 2012) have been attempted in order to understand these circumstances as well as their impacts on the shape of the clouds. However, they face a major problem, namely the variety of phenomena involved in such an evolution. Choosing the proper start parameters for the HVCs as well as their environmental conditions is also very challenging because of the distance uncertainties.

Quilis & Moore (2001) show evidence of tails of compression fronts in HVCs, which can be the result of stripping of the cloud as it condenses and falls onto the disk. Furthermore, they suggest mass limits of 10 to 100 M$_\odot$ for clouds located at distances between 1 to 10 kpc under the assumption that the extension of the cloud is about 1°. Quilis & Moore (2001) also conclude that the cloud must be in pressure equilibrium with the warm ionized medium located in and above the disk. In their simulations they consider two different scenarios: dark-matter dominated HVCs further away from the Galactic

disk and pure gas HVCs. In both cases, they find the HT features as long a halo density $\geq 10^{-4}\,\mathrm{cm}^{-3}$ is available. Furthermore, Plöckinger & Hensler (2012) investigate the cometary shape of the clouds. They demonstrate that purely baryonic, low-mass HVCs are torn by ram pressure, while the more massive ones survive and show a HT structure (their Fig. 5).

Konz et al. (2002) address the question of the dynamical and thermal stabilization of cold dense clumps in a hot, thin ambient environment. The main motivation of their study is to investigate the impacts of magnetic fields on the stability of the clouds using magnetohydrodynamics (MHD) simulations. Konz et al. (2002) study objects in the gaseous arms of the Magellanic system. With the help of a 2D-simulation they investigate the interaction of a cold neutral cloud with its hot and ionized surrounding. They find that the Galactic magnetic field wraps the clouds locally and partially shields the fast traveling cloud from its hot surrounding. The magnetic field prevents the diffusion of hot plasma into the cloud and therefore stabilizes the clouds. Furthermore, they argued that even the weak magnetic fields in the halo are sufficient for the shielding effect.

5.5 Summary and outlook

In the current chapter, deep integrated observations of the WNM for three CHVCs, using the 100 m Effelsberg telescope and high-resolution observations of the more compact regions from the WSRT, as well as the results of their combination are presented. The results of the introduced approach show that the combination in the image domain meets the expectations. The critical step in the algorithm is the regridding, where a flux inconsistency can occur as a result of interpolation inaccuracies (Chap. 3).

The combination results demonstrate the importance of the short-spacing correction (SSC) regarding the determination of the physical and morphological properties of the objects. Here in particular the WNM is of major interest. HVCs in higher ambient pressure environments might show complex spatial and spectral structures.

The results of the Gaussian decomposition suggest strongly that the three clouds mostly consist of WNM. The analysis of Winkel et al. (2011) also confirms the lack of cold components in HVCs in the complex known as Galactic centre negative (GCN). However, high Doppler temperatures above 10^4 K are an indication of the existence of turbulence within the clouds. The results demonstrate that the gas gets warmer or more turbulent in the tail region and at the edges of the clouds. This also suggests that the warm gas is floating away to the direction of the tail, which is an indication of existing ram pressure. Another remarkable aspect is the decreasing velocity gradient at the regions with lower column densities. The relatively slow movement of the cloud reveals the lack of cold cores in the clouds, and the measured high Doppler temperatures demonstrate that the clouds are not in equilibrium.

The linear approach used in the image domain is easy to implement and is not very CPU-intensive. It could be very helpful for computation of huge amounts of data coming from telescopes like Australia's Square Kilometer Array Pathfinder (ASKAP, Duffy et al. 2012) and WSRT/Apertif.

Conclusions and Outlook

6.1 Summary

Interferometric arrays are insensitive towards large angular scale structures of an object. This is because of the incompleteness of the central region of their spatial frequency domain, the missing-spacing problem (MSP). For Galactic objects as well as a number of nearby galaxies, interferometric arrays are not able to resolve the warm and diffuse components of the objects. Single-dish instruments, however, are sensitive towards large angular scale structures. Therefore, these are able to provide the missing-spacing information, which can be added to the interferometric data, i.e., short-spacing correction (SSC).

The new era in radio astronomy will be charactrized with modern interferometers (Garrett et al. 2010; Duffy et al. 2012; Dickey et al. 2013). However, for these instruments the MSP will still be an issue. The new instruments provide large amounts of data (Alexander et al. 2009), which makes the long term storage of raw data impractical. This study presented a new pipeline to perform the SSC. The approach considers the features of the new instruments. It operates on the cleaned interferometric data and does not require any raw data.

Chapter 2 discussed both observational approaches for single-dish telescopes and interferometric arrays, which are very different. A thorough understanding of both imaging techniques is of significant importance for SSC. Furthermore, different single-dish and interferometric H I surveys have been introduced. The data from these surveys have been used in this study.

Chapter 3 introduced the MSP. An overview of a number of existing approaches has been provided to perform the SSC. The latter chapter addresses two major questions: first, whether it is possible which perform the SSC in the image domain, using only the cleaned interferometric data. Second, whether the approach fulfills the expectations regarding measured total flux and angular resolution of the combined data. Furthermore, the physical principle of the new implemented pipeline is discussed. The pipeline has been evaluated with Small Magellanic Cloud (SMC) observations (Stanimirović et al. 1999). Finally, a comparison with the other existing methods is provided. In the following, the results of this chapter are presented.

- A new and fully automated pipeline performs the SSC in the image domain. The introduced approach does not require any additional information such as visibilities or the exact knowledge of the beams. The only inputs of the pipeline are single-dish (low-resolution) and interferometric (high-resolution) data sets.

- For evaluation, the single-dish and interferometric observations of the SMC from the 64 m Parkes telescope and the Australia Telescope Compact Array (ATCA) have been combined. The analysis of the SSC data reveals that the combination fulfills the expectations such that the measured total flux in the combined data cube is in a very good agreement with the corresponding value from the single-dish data cube, while the angular resolution of the interferometric data is preserved after the combination.

- Furthermore, the result of the combination for the SMC emphasizes the necessity of SSC for a detailed understanding of different gas components present in the interstellar medium (ISM) for Galactic objects, where a considerable amount of diffuse gas is present.

Chapter 4 introduced the result of SSC for three nearby galaxies: NGC 2403, NGC 4214, and NGC 5055. The single-dish observation of NGC 2403 contains strong Milky Way emission. NGC 2403 has been used to study the effect of the strong Galactic emission on the combined data. Additionally, the impacts of two imaging parameters: weighting scheme and pixel size have been studied for NGC 4214 and NGC 5055. Finally, observations of NGC 5055 with the Very Large Array (VLA) and the Westerbork Synthesis Radio Telescope (WSRT) have been compared. The results of the latter chapter can be summarized as follows:

- The strong Galactic emission present in the single-dish observation of NGC 2403 propagates in to the combined data. The strong emission results in an overestimation of the measured total flux in the SSC data. Furthermore, it affects the velocity fields in the combined data. Therefore, the analysis of velocity fields based on the combined data will not produce any reliable results.

- The analysis of two imaging parameters for NGC 4214 and NGC 5055 yields that both pixel size and weighting scheme affect the result of interferometric map. However, the variations due to different weighting schemes are much stronger than due to different pixel sizes.

- Two weighting schemes: natural and uniform have been studied. The results strongly suggest that the natural weighting is the appropriate scheme for the purpose of the combination especially for the nearby extragalactic objects. The reason for this is that the effect of the negative bowls is less significant.

Chapter 5 [1] presented sensitive observations of three compact high-velocity clouds (CHVCs) in the halo of the Milky Way based on single-dish observations with the 100 m Effelsberg telescope and interferometric observations with the WSRT. These observations as well as the result of their combination have been used to study the physical and morphological properties of these CHVCs. In the following, the results of this chapter are presented.

- All three clouds reveal a head-tail (HT) structure in their H I observations.

- The difference between the measured total fluxes in the single-dish and interferometric data cube suggests that all three CHVCs contain a considerable amount of diffuse gas.

- The combination has been performed for CHVCs. The results reveal that also in the case of CHVCs the combination pipeline fulfills the expectations.

---

[1] Based on a publication by Astronomy & Astrophysics (A& A) journal entitled: neutral atomic hydrogen (H I) observations of three compact high-velocity clouds around the Milky Way.

- The clouds have been investigated for two component gas: warm neutral medium (WNM) and cold neutral medium (CNM). The investigation showed that all the three clouds only consist of WNM. This result is in agreement with the findings of Wolfire et al. (1995b) regarding single-phase medium. Furthermore, Winkel et al. (2011) could not also find any evidence for CNM in high-velocity clouds (HVCs) in the complex Galactic centre negative (GCN).

6.2 Future work

In the following, different related projects as well as follow-up approaches are introduced. These approaches are supplementary to the introduced research in this thesis.

As the next step, it is planed to perform the SSC for all the The H I Nearby Galaxy Survey (THINGS, Walter et al. 2008) galaxies, which are not blended with the strong Milky Way emission. For the best possible result, it is desirable to carry out deep H I observations of the target galaxy with the 100 m Effelsberg telescope in order to achieve root mean square (RMS) noise levels comparable with the measured values in the shortest baselines of the THINGS data sets. In the framework of this study, it is possible to analyze the impacts of SSC prior to the deconvolution. Kurono et al. (2009) performed a theoretical study on this subject.

One of the first objects, which has been investigated for the aim of this research was NGC 5236 (M83, Huchtmeier & Bohnenstengel 1981; Bigiel et al. 2010; Silva-Villa & Larsen 2012). Originally, the SSC has been performed for the THINGS single-pointing and the Effelsberg single-dish observations. However, the extent of the galaxy in the single-dish observation emphasizes the need for a wide-field interferometric mosaic. For this purpose, a VLA observational proposal has been submitted, which has been accepted. The interferometric observations are currently being carried out with the VLA. It is planned to perform the SSC with the introduced algorithm in this thesis. Only with the combined data, it is possible to study the H I content of the galaxy as well as star formation regions comprehensively.

Another important topic is the impact of the missing spacings as a function of distance. It is well understood that SSC is irrelevant for objects located at high redshifts. Quite on the contrary, it has been shown that it is not negligible for Galactic objects as well as some of the nearby galaxies. In order to perform a systematical study of the impacts of the missing spacings as a function of distance, simulations based on original observations (e.g., Whiting & Humphreys 2012; Wootten & Thompson 2009) of different types of objects are required. An interesting approach is estimating a possible upper distance limit, under which missing spacings are still relevant, where high-resolution interferometric observations lack the information. For this, single-dish and corresponding interferometric simulations of different objects with different physical properties located in different distances are required. For the interferometric simulations, the spatial and spectral variations as a function of distance are a major consideration, since interferometric arrays can resolve different structures depending on the distance to the source. Using the simulations, it is possible to study the impact of the SSC as a function of distance.

Data cubes and moment maps

neutral atomic hydrogen (H I) data cubes are three dimensional position-position-frequency (PPF) or position-position-velocity (PPV) arrays. Each position map corresponding to a certain frequency or channel is referred to as a plane. The separation between two adjacent channels is commonly referred to as channel width. For each source either the flux density S in units of $\mathrm{Jy\,beam^{-1}}$ or brightness temperature T_B in units of Kelvin is measured. The former quantity is widely used for extragalactic sources, whereas the latter quantity is more commonly used for Galactic observations. The conversion of flux density into brightness temperature is done by the following equation. It should be noted that the introduced equations and the corresponding constants are explicitly for the H I observation and the constants change for other spectral line observations.

$$T_B = \frac{\lambda^2 S}{2 K_B \Omega}, \tag{A.1}$$

where λ is the wavelength, S the flux density, K_B the Boltzmann constant, and Ω the beam solid angle. For 21 cm line observations the above mentioned equation can be simplified:

$$T_B = \frac{606 S}{a \times b}. \tag{A.2}$$

The measured T_B is given in Kelvin, S in mJy, and a and b are beam major and minor axis in arcseconds. For an optically thin gas ($\tau \leq 1$) the integrated flux over a spectral line can be converted into the corresponding H I column density $N_{H I}$ with the help of

$$N_{H I} = 1.823 \, 10^{18} \int T_B \, dv, \tag{A.3}$$

where $N_{H I}$ is in atoms $\mathrm{cm^{-2}}$, T_B in Kelvin, and v in $\mathrm{km\,s^{-1}}$. For an optically thin gas, the H I mass can be computed using the integrated H I flux if the distance to the structure is known.

$$\frac{M_{H I}}{M} = 2.36 \, 10^5 \, d^2 \int S_v \, dv. \tag{A.4}$$

S_v is in units of $Jy\,km\,s^{-1}$ and d in Mpc (Rohlfs & Wilson 2004).

Furthermore, the data cubes can be used to create the so-called moment maps. In the following, the most commonly used moment maps are described.

- The zeroth moment is the integrated intensity over all velocity channels.

$$M_0 = \Delta v \sum I_i. \tag{A.5}$$

  Δv is the channel width and I_i is the intensity per plane. The units of a velocity-integrated map are $Jy\,km\,s^{-1}$. The velocity-integrated maps can be converted to column density maps using equation A.3.

- The first moment is used for analyzing the velocity fields. It describes the intensity-weighted velocity of the spectral line and is described by the following equation:

$$M_1 = \frac{\sum I_i v_i}{M_0}, \tag{A.6}$$

  where I_i is the intensity in the i-th plane, v_i the corresponding velocity, and M_0 is the zeroth moment of the data cube. The velocity distribution is expressed in units of $km\,s^{-1}$.

- The second moment describes the velocity dispersion along the line of sight in $km\,s^{-1}$, which describes typically the measured linewidth.

$$M_2 = \sigma_v = \sqrt{\frac{\sum I_i (v_i - M_1)^2}{M_0}}. \tag{A.7}$$

The common astronomical software packages such as Astronomical Image Processing System (AIPS, Greisen 1990), Multichannel Image Reconstruction, Image Analysis And Display (MIRIAD, Sault et al. 1995), and Common Astronomy Software Applications (CASA, McMullin et al. 2007) provide ready-to-use tasks to compute moments from a data cube. The tasks *immoments*[1] in CASA or *moment*[2] in MIRIAD can be used to compute different moment maps for a given image.

The moment maps are used to compute a number of important quantities such as total flux, column density (Eq. A.3), total H I mass (Eq. A.4), and rotation curve (Eq. A.6).

Observed frequency and radial velocity

For the spectroscopic H I observations the radial velocity, i.e, the measured velocity along the line of sight, is of great importance. The observed frequency f of a celestial object provides kinematical information. The part of the emission which approaches the observer reveals higher frequencies (blueshift) than the portion of emission which is moving away (redshift) due to the Doppler effect. The same phenomenon has a significant contribution to the broadening of the line (Boltzmann distribution). The following equation describes the relationship between the observed frequency f in Hz and its corresponding velocity V in $km\,s^{-1}$. The latter unit is more commonly used unit for expressing the line width.

---

[1] http://casa.nrao.edu/docs/CasaRef/image.moments.html
[2] http://www.atnf.csiro.au/computing/software/miriad/doc/moment.html

$$V = c \, \frac{f_0^2 - f^2}{f_0^2 + f^2},$$

where c is the speed of light, f_0 the rest frequency of the observed line, and V in units of $\mathrm{km\,s^{-1}}$. There exist two approximations of the aforementioned equation, i.e., the radio and optical definition given by the following equations:

$$V_{\mathrm{opt}} = c \, \frac{f_0 - f}{f_0},$$

is the so-called radio definition, whereas the optical definition is defined as:

$$V_{\mathrm{rad}} = c \, \frac{f_0 - f}{f}.$$

It should be noted that for higher redshifts the divergence between the radio and optical velocity is significant. All the data sets presented in this thesis the radio velocity definition has been applied. In some cases, e.g., a comparison of radio and optical surveys the optical definition is more feasible.

Rest frames

Depending on the location of the observed objects, different rest frames must be taken into account in order to obtain the correct radial velocity. The origins of the coordinate systems for each rest frame are different. These rest frames account for different effects such as the rotation and the motion of the Earth, the motion of the Sun around the Galactic center, and the motion of the Milky Way within the Local Group (Westmeier 2014). The rest frames differ in the defined origin of each coordinate system. In the following, the most frequently used rest frames as well as their relationships are defined.

The barycentric standard-of-rest (BSR) is the appropriate reference frame for objects in the solar neighborhood. However, most of the radio observations are in the heliocentric standard-of-rest (HSR). The former rest frame has its reference point at the position of the solar system barycenter, whereas the latter one uses the Sun as the reference point. For the majority of observations the difference between BSR and HSR is negligible (Westmeier 2014).

For Galactic objects located at distances beyond the Sun the local standard of rest (LSR) is the commonly used rest frame. It accounts for the peculiar motion of the Sun ($\approx 16.55\,\mathrm{km\,s^{-1}}$) with respect to the regular motion of the Galaxy. The LSR-velocities can be derived from the BSR-velocities using the following equation:

$$V_{\mathrm{LSR}} = V_{\mathrm{BSR}} + 9 \, \cos(l)\cos(b) + 12 \, \sin(l)\sin(b) + 7 \, \sin(b).$$

l and b are the Galactic longitude and latitude of the observed object. For circumgalactic objects, one can also correct for the rotation of the Milky Way ($\approx 220\,\mathrm{km\,s^{-1}}$). The corresponding reference frame is the so-called Galactic standard-of-rest (GSR).

$$V_{\mathrm{GSR}} = V_{\mathrm{LSR}} + 220 \, \sin(l)\cos(b).$$

It should be noted that the variation between LSR and GSR radial velocities can be significant (up to $220\,\mathrm{km\,s^{-1}}$). The Local Group standard-of-rest (LGSR) considers the motion of the Milky Way with respect to the barycentric point in the Local Group ($\approx 80\,\mathrm{km\,s^{-1}}$). The corresponding reference frame in this case is derived from the GSR-velocities via the following equation:

$$V_{\mathrm{LGSR}} = V_{\mathrm{GSR}} - 62\,\cos(l)\cos(b) + 40\,\sin(l)\cos(b) - 35\,\sin(b).$$

System temperature and sensitivity

The system temperature

Fluctuations of the amplitude and phase of a received signal cause noise and decrease the sensitivity of the instrument. There exist different sources, which increase the noise level of a radio telescope, e.g., ground radiation and standing waves. For a radio telescope the system temperature T_{sys} consists of the following contributions:

$$T_{sys} \propto G \cdot (T_G + T_A + T_S + T_{SW} + T_R), \qquad (B.1)$$

where G is the gain factor, T_G the ground temperature, T_A the atmospheric temperature, T_S the source temperature, T_{SW} the measured value for the standing waves, and T_R is the measured value at the receiver (Rohlfs & Wilson 2004). For the 100 m Effelsberg telescope, T_R is of the order of 20 to 23 Kelvin, whereas T_G is $\approx$ 20 Kelvin. The measured T_{sys} at 1.42 GHz is $\approx 40 - 50$ Kelvin. The noise in the measurements is caused mainly by T_G, T_R, and T_S.

For the radio telescopes, the surface around the telescope acts as a blackbody. A telescope receiver is sensitive in all directions and collects the power of different waves from all directions. The radiation from the ground reaches the surface of the telescope towards its edges, i.e., spillover. As a rule of thumb, the measured power due to spillover increases with decreasing elevation. In order to minimize the spillover, the receivers are tapered outwards, i.e., the sensitivity of the receiver decreases towards its edges. Tapering minimizes the effect of the spillover, however it also decreases the angular resolution of the instrument. The atmosphere also can increase the noise level, however, for H I observations it is negligible.

An additional phenomenon which plagues the spectroscopic observations are the standing waves (SW, Popping & Braun 2008), which are periodic fluctuations (Briggs et al. 1997). SW describes the characteristic of the waves reflected between different parts of a radio telescope, in particular between the primary focus and the apex of the telescope. The approximate wavelength measured for SW as a function of focal distance f is described by Popping & Braun (2008). The latter authors showed that SW cause variations in the primary beam as a function of frequency.

For the 100 m Effelsberg telescope the distance between the primary focus and the apex is about 30 m. Measurements have shown that the frequency of the standing waves between these two points is about 5 MHz (Flöer 2014, priv. comm.). However, this is only the dominant standing wave mode. The

Effelsberg telescope is a complex instrument with a seven-feed-array receiver and 4 supporting legs, where reflections between all these parts produce SW in all directions. Antenna side lobes can pick up the signal originated from the stray radiation and cause a significant overestimation of received signal (Kalberla et al. 1980). The impacts of stray radiation is critical for objects at high latitudes with low emission (Kalberla 2014, priv. comm.). A number of existing H I surveys such as the Leiden/Argentine/Bonn Galactic H I Survey (LAB, Kalberla et al. 2005) and the Galactic All-Sky Survey (GASS, McClure-Griffiths et al. 2009; Kalberla et al. 2010) have been corrected for SW (Kalberla et al. 2010). The Galactic part of the Effelsberg-Bonn H I Survey (EBHIS, Kerp et al. 2011) will also be corrected for the standing wave effects (Kalberla et al, in prep.).

Single-dish and interferometer sensitivity

Single-dish and interferometric data sets suffer from a number of uncertainties caused by, e.g., radio-frequency interference (RFI) and calibration uncertainties. RFIs are man-made signals generated locally or off-site. A comprehensive study of the RFI situation at the 100 m Effelsberg telescope as well as an algorithm for automated RFI detection for EBHIS data sets has been presented by Flöer et al. (2010). Winkel et al. (2012b) address a number of errors in the calibration of spectral line data and their impacts on the scientific data sets. Ekers (1999) pointed out the importance of error treatment and discussed possible errors which can occur during the imaging process for interferometric data sets. The nature as well as the magnitude of the uncertainties differ for single-dish and interferometric systems. In the following, one of the most important properties of both data sets, i.e., sensitivity is discussed in detail.

Root mean square (RMS) is a term to specify the sensitivity of a radio-interferometric measurement, i.e., the fluctuation added to the true brightness temperature of the source. Different parameters influence the magnitude of these fluctuations. The radiometer equation determines the corresponding value:

$$\Delta T_{\text{SD}} \quad = \quad \frac{M \cdot T_{\text{sys}}}{\sqrt{\tau \cdot \Delta v}}, \tag{B.2}$$

where M accounts for the loss in sensitivity produced by the analog to digital conversion (Rohlfs & Wilson 2004). For modern FFT spectrometers this value is one. T_{sys} is the system temperature as described in Sec. B. For H I observations the contribution of T_{A} is negligible. Δv describes the receiver's bandwidth. τ is the integration time. The above-mentioned equation describes the RMS value for a single dish. For an interferometer the equation differs only slightly.

$$\Delta T_{\text{Int}} \quad = \quad \frac{M \cdot T_{\text{sys}}}{\sqrt{2 \cdot N \cdot \tau \cdot \Delta v}}. \tag{B.3}$$

$N = \frac{n(n-1)}{2}$ is the number of baselines. τ is the observation time and Δv the receiver's bandwidth. Donho & Johnstone (1994) show that the median absolute deviation (MAD) is a robust estimator for the RMS noise level (σ) in the data set. The MAD has a breakdown point of 50%, since it considers the median. If the mean value is an outlier, MAD is no longer reliable. Furthermore, the breakdown point applies only in the limit of an infinite number of data points. MAD is defined as follows:

$$\text{MAD} = \text{median}(\text{abs}(\text{data} - \text{median}(\text{data})))/0.6745. \tag{B.4}$$

The signal-to-noise (S/N) ratio is given by $T_A/\Delta T$. S/N gives the detection limit of an instrument for a source with a specific flux density. T_A is the antenna temperature and ΔT the RMS noise value. Consequently, S/N is proportional to effective aperture A_{eff}, Δv, and τ and is inversely proportional to T_{sys}.

Technical details of the SSC pipeline

The section presents a brief overview of the used tasks and tools as well the constitution of the short-spacing correction (SSC) pipeline (Chap. 3). The presented information is predominantly of interest for modification purposes. For more detailed information regarding the CASA tasks and tools refer to the CASA cookbook (Ott & Kern 2014). Some information has been adopted from the CASA cookbook.

Choice of the Framework

The pipeline is a fully automated script written in Python which makes use of a number of existing tools and tasks implemented in CASA. A list of CASA architectural components is presented by McMullin et al. (2007). The framework uses measurement sets (MS) as the overall data structure. A MS consists of a table for visibilities (data from the telescope) and some additional sub-tables (auxiliaries). In addition to data access and display tools[1], the framework provides both low- and high-level utilities, i.e., tools and tasks, for handling the data sets (McMullin et al. 2007). Tasks are built upon tools. They provide higher level accessibility for more commonly used applications. Tools are lower level utilities with an object-oriented interface. Additionally, CASA offers a default command line interface with scripting ability implemented in Python (Ott & Kern 2014). The framework also provides the necessary tools and tasks for single-dish and interferometric simulations, which are very helpful for testing and evaluation purposes.

The astronomical principle of the algorithm has been described in Chap. 3. In the following, more technical aspects of the introduced pipeline are presented.

Internal constitution and technical specification

The introduced algorithm can be easily migrated into CASA as an embedded task. CASA offers the possibility for including new tasks, which requires a task interface description Extensible Markup Language (XML) file[2]. The XML file consists of attributes, subelements, inputs, outputs, constrains, and

---

[1] The framework provides an embedded viewer for displaying both measurement sets and images.

[2] XML is a markup language. It is commonly used for defining set of rules for encoding documents in a specific format, so that both human and machine are able to read and comprehend them.

return values[3].

Additionally, it is possible to implement the pipeline in any other astronomical framework such as MIRIAD or AIPS. It can also be implemented using one of the common programming languages. However, the major step is implementing a reliable regridding routine outside of CASA that is able to preform the regridding along three axes.

In the following, different components of the pipeline as well as their functionality are described.

Execution and input

The script can be executed in the IPython shell of CASA via `execfile('[Name]')` (Ott & Kern 2014). In general this can be used for executing any Python script in the IPython shell. The inputs of the pipeline are as follows: source, single-dish telescope, interferometric array, single-dish FITS[4] file, and interferometric FITS file. Source is a string given by user. This string concatenated with the name of interferometric array is used as the prefix for all the intermediate results and the combined data set.

Preliminary preparations

Different routines determine the current date and path and create a target directory in the current path for saving the MSs. An additional routine checks if the target directory already exists from a previous run.

Prior to the combination, a number of useful variables are defined. For single-dish images the LR designation has been used, which stands for low resolution. For interferometric data sets HR is used to designate high resolution, respectively. In the following the list of all CASA images as well as their functionality is presented:

- LR.im: imported single-dish data cube

- HR.im: imported interferometric data cube

- LR_ reg.im: regridded single-dish image

- HR_ conv.im: convolved interferometric image

- sub.im: diference between LR_ reg.im and HR_ conv.im

- sub_ bc.im: flux weighted by the ratio of the beam areas

- combined.im : short-spacing corrected image

- combined.fits: result of the pipeline exported as a common FITS file

There exits a `testMode` variable which has been added for testing purposes. The default value of `testMode` is false, which means that all the above mentioned CASA images are discarded once the combination is complete.

---

[3] User reference manual of CASA provides some help for migrating new tasks at `http://casa.nrao.edu/docs/userman/UserManse114.html`

[4] Flexible Image Transport System (FITS) is a standardized file format, which is commonly used for storing scientific data. Each file consists of a ASCII header with specific keywords that are easily readable for human and machine as well as of the scientific data.

Importing FITS files

CASA uses its own data format, the so-called CASA image, which is a MS. In order to be able to make use of CASA tasks and tools, the common FITS files need to be converted into CASA images[5]. This can be done using the `importfits` task. It is important to note that some of CASA tasks, e.g., `importfits`, offer an option to overwrite a pre-existing image (Ott & Kern 2014). The pipeline however, does not overwrite any existing image. Instead, prior to any new run the script cleans up all the available images from the previous runs in the source directory.

CASA also creates a number of additional files, e.g., `.last` and `.log` files. The `.last` file is written into the current path after a specific task has been successfully executed. It is meant for the re-execution of a task using the saved parameters. For complex tasks with a large number of parameters it is desirable to save the parameter prior to the execution. This can be done using the `saveinputs` command (Ott & Kern 2014).

The framework also stores the command line history automatically in a log file, `ipython.log` in the local directory, which can be edited or executed, if necessary (Ott & Kern 2014). Furthermore, the framework creates a `casapy-YYYYMMDD-HHMMSS.log` storing the output from CASA commands in the local directory, where YYYYMMDD-HHMMSS are the Universal Time (UT) date and time of the CASA's start up [6]. For each fresh run of the script all the existing last and log files get discarded.

Regridding of low- and high-resolution data

The single-dish and interferometric data sets have different coordinate projections. The pixel size and beam sizes are also different. The single-dish beam is commonly circular and is not declined, whereas the interferometric beam is more elliptical with a certain position angle. In order to be able to compute the difference between the single-dish and interferometric data cubes, both data sets should have the same projection, channel width, field of view (FoV), and pixel size.

It is highly recommended to discard the degenerate Stokes axis prior to regridding. This can be done within CASA using `image.subimage` or before the data is imported to CASA. For regridding the data sets, CASA provides a task (`imregrid`) as well as a tool (`regrid`). The former task is used to regrid an image to a new coordinate system. The latter tool is a function from the `image` module in CASA. It provides more flexibility for regridding. The script makes use of the `image.regrid` function. In order to perform the regridding correctly, a proper coordinate system must be given as an argument for the function. This can be done with the help of `Coordsys` tools in CASA (Ott & Kern 2014). The output image has the same shape as the input image. The regridding parameters are determined with the help of a given coordinate system. The function also provides the possibility of regridding along one or two axes. For the purpose of the combination however, it is required to regrid along two position and one velocity(frequency) axes. The input of a number of header items, e.g., rest frequency, reference pixel, reference value, increment values, and type of the data sets is required. It is of great importance to check if the required items are available in the header of both data sets before one starts with the processing. Additionally, the `image.coordsys` tools also provide the opportunity for adding the required items prior to the regridding, if necessary (Ott & Kern 2014). The function provides three embedded interpolation schemes; linear, nearest, and cubic. The default interpolation scheme is linear. Linear interpolation is the choice of interpolation scheme for the presented data sets in the introduced algorithm. This scheme is flux consistent, i.e., it preserves the total flux of the image within the regridded

---

[5] Some of CASA tasks and tools are able to process the original FITS files as well, however, it is highly recommended to convert them to CASA images.

[6] For more detailed information see `http://casa.nrao.edu/casa_cookbook.pdf`

region. This is essential for the purpose of the combination, since the ultimate goal of the pipeline is to preserve the original single-dish flux as good as possible. Furthermore, the Cubic interpolation is slower than the linear scheme while the improvement is only moderate.

Additional inputs are the names of the single-dish and interferometric observatories. In some cases, the telescope position is required for a proper conversion of the reference code. The `regrid` routine sets the instrument with the `settelescope` function. The telescope position is part of the `Coordinate System` class and should be set correctly for a proper regridding. A list of all of known observatories to CASA can be found with the help of `obslist` function (Ott & Kern 2014). If the instrument is not available within the listed observatories in CASA, one needs to add the instrument manually.

The output of the the `regrid` function has the designation LR_{reg} for regridded low-resolution data set. This data cube has the same number of axes, coordinate system, projection on the celestial sky, size of the field of view, and pixel size as those of the interferometric data set.

Convolving the interferometric image and determination of the missing flux

As it has been mentioned before, the interferometric and single-dish data sets reveal different angular resolution (Chap. 2). Therefore, both instruments are sensitive to different spatial scales of the same object. The difference between the regridded single-dish (LR_{reg}) and convolved interferometric image (HR_{conv}) reveals the missing flux, which is only detectable with the single-dish telescope.

The `imsmooth` task has been used to convolve the interferometric image with a two dimensional Gaussian function with FWHMs equal to the beam major and minor axes of the single-dish instrument, where both beam major and minor axes are in units of arcseconds. A subroutine obtains the values of beam major and minor axis from the header of the single-dish image including their unit. The stored values in the header are often in degrees. Prior to the convolution, the subroutine converts the values from degree to arcseconds if necessary.

Adding the missing-spacing flux

`immath` performs mathematical operations on one or more given images. The expressions can be specified directly or a pre-defined expression used for specific calculations (Ott & Kern 2014). For this purpose the argument `mode` should be set to `evalexpr`, such that the task evaluates the expression defined in `expr`.

In order to fill the information gap in the very low-spatial frequencies the missing flux should be added to the original interferometric image. The script uses `immath` to compute the difference between LR_{reg} and HR_{conv} images. The result is a new CASA image with the designation `sub.im`. Before this new image can be added to the original interferometric image, a subroutine computes the weighting factor α, which is the ratio of both single-dish (Ω_{sd}) and interferometer beam areas (Ω_{int}) as described in Sec. 3.3.

The result of the multiplication of `sub.im` with α is a new CASA image, called sub_{bc}.im. This data cube contains the weighted missing information. The final step of the algorithm is adding sub_{bc} to the original interferometric image, `HR.im`. This is also done with the help of `immath` task. The output is the short-spacing corrected interferometric image with the designation `combined.im`. The final step of the pipeline is exporting the `combined.im` to a common FITS file. All the partial result (CASA images) are moved to the target directory and get discarded; if `testMod` is set to be false. Furthermore, all the existing `.log` and `.last` files are deleted.

Synthesized imaging

D.1 Theoretical primary beams

The function $\cos(c \cdot n \cdot r)^6$ describes the attenuation of the Westerbork Synthesis Radio Telescope (WSRT) primary beam (Popping & Braun 2008). r is the distance from the pointing center in units of degrees, n the observing frequency in GHz. For all the H I observations presented in this thesis the value is 1.42 GHz and $c = 68$ is constant over the H I frequency [1].
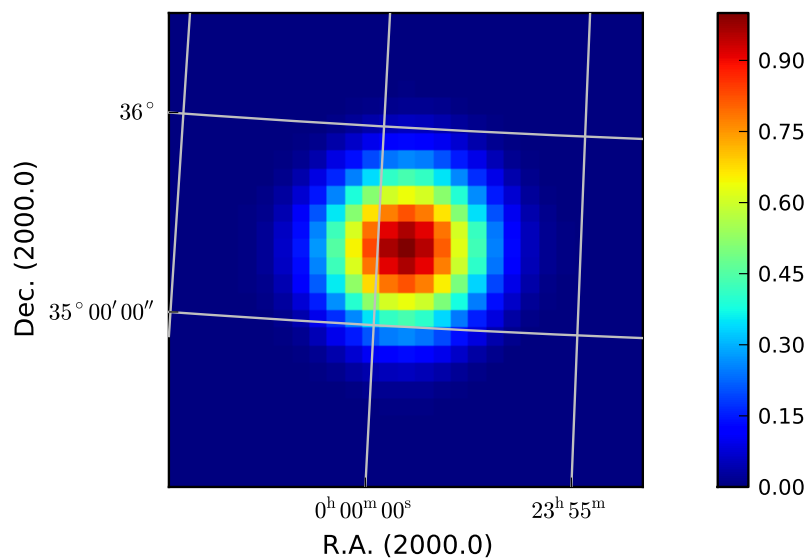
Figure D.1: Attenuation of the primary beam of the Westerbork synthesis radio telescope (WSRT) described by the function $\cos(c \cdot n \cdot r)^6$.

The attenuation of the Very Large Array (VLA) primary beam can be modeled with the help of the following 4th-order polynomial:

---

[1] Source:http://www.astron.nl/radio-observatory/astronomers/wsrt-guide-observations/wsrt-guide-observations

$$1.0 \quad + \quad X^1 \cdot \text{PBPARM3}/(10^3)$$
$$+ \quad X^2 \cdot \text{PBPARM4}/(10^7)$$
$$+ \quad X^3 \cdot \text{PBPARM5}/(10^{10})$$

with $X = (r \cdot n)^2$, where r is distance from the center of phase in arcminutes and n the frequency in GHz. The primary beam parameters for the VLA for 1.465 GHz are as follows: PBPARM3=-1.343, PBPARM4=6.579 and PBPARM5=-1.186 [2].

D.2 Flux residual rescaling

Residual rescaling is a delicate operation in the process of imaging. As a matter of fact, it is necessary for obtaining true flux values for interferometric data cubes. The current section deals with the theoretical consideration of the approach and how it can be realized.

Equation 3.1 describes the relation between the total flux S and total intensity I measured for an interferometric map:

$$S_{\text{tot}} = \int\limits_{\text{source}} I \, d\Omega.$$

S is in [Jy] and I in [Jy/beam]. $d\Omega$ is the beam solid angle. The solid angle for a Gaussian elliptical beam is defined by:

$$\Omega_{\text{beam}} = \frac{\pi \, \Theta_{\text{maj}} \Theta_{\text{min}}}{4 \ln 2}, \tag{D.1}$$

where Θ_{maj} and Θ_{min} are the full width at half maximum (FWHM) of the beam major and minor axes.

In order to measure the flux value in units of Jy within a cube or a region, one needs to consider the beam area on an specific pixel grid. Therefore, the Eq. D.1 needs to be modified. In this case, the measured flux is the sum of all pixel values within the desired area divided by the beam area as described in Eq. D.2.

$$\Omega_{\text{beam}} = \frac{\pi \, \Theta_{\text{maj}} \Theta_{\text{min}}}{4 \ln 2 \, (\text{pixel size})^2}. \tag{D.2}$$

Θ_{maj} and Θ_{min}, and pixel size are all in units of arcsecond.

Jorsater & van Moorsel (1995) pointed out an important property of the interferometric data: there exists no interferometric map which only consists of clean components. Cleaning per se can be considered as a denoising algorithm if one only considers the clean components. However, for the final image the residual maps are added to the clean components. These are the regions that have not been cleaned and therefore, consist mainly of noise or faint emission.

Additionally, the dirty beam is described by a Gaussian with additional side lobes. The effective resolution of the interferometric images is described by the FWHM of an elliptical Gaussian fitted to the main lobe of the dirty beam, the *clean beam*. This means that the clean beam and the dirty beam are not identical and the clean beam is usually smaller than the dirty beam (Jorsater & van Moorsel 1995).

---

[2] source:http://www.aips.nrao.edu/cgi-bin/ZXHLP2.PL?PBPARM

For the true flux in a cleaned image one should account for the resolution attenuations in different parts of the map. Jorsater & van Moorsel (1995) showed that the contribution of the residual flux can be strongly dependent on the cleaning depth and properties of the structure. In this case the common assumption to consider the clean beam for the entire map is unsatisfactory. The authors proposed an alternative approach to equalize the flux differences. They introduce a weighting factor ϵ defined as clean and dirty beam areas' ratio. Subsequently, the total flux is the sum of cleaned flux and weighted residual flux (Jorsater & van Moorsel 1995, their first two equations in appendix 2).

List of abbreviations

ACS anti-center shell. 90

AIPS Astronomical Image Processing System. 36, 63, 88, 110, 118

ASKAP Australia's Square Kilometer Array Pathfinder. 7, 12, 30, 103

ATCA Australia Telescope Compact Array. 24, 27, 30, 34, 36–39, 43, 48, 49, 106

BSR barycentric standard-of-rest. 111

CASA Common Astronomy Software Applications. 33, 79, 110, 117–119

CHVC compact high-velocity cloud. 13, 24, 85, 87–90, 92, 95, 97, 99–101, 103, 106

CNM cold neutral medium. 87, 91, 97, 99, 100, 102, 107

CR cosmic rays. 99, 101

DSS Digitized Sky Survey. 54, 55, 61

EBHIS Effelsberg-Bonn H I Survey. 11, 12, 17, 23–25, 54, 62, 71, 114

EN extremely negative. 90

FFT Fast Fourier Transformation. 19, 61, 69

FITS Flexible Image Transport System. 31, 33, 118, 119

FoV field of view. 18, 33, 34, 46, 50, 63, 79, 91, 94, 119

FPGA Field Programmable Gate Array. 24

FWHM full width at half maximum. 17, 33, 36, 66, 88, 97, 122

GASKAP Galactic Australian Square Kilometer Array Pathfinder. 12

GASS Galactic All-Sky Survey. 11, 23–25, 35, 114

GCN Galactic centre negative. 103, 107

GSR Galactic standard-of-rest. 111, 112

H I neutral atomic hydrogen. 7, 11–13, 15, 23–25, 31, 34, 37, 46, 49, 51, 52, 78, 85–88, 91, 97, 99, 101, 102, 106, 109, 110, 113, 114, 121, 137

HALOGAS Hydrogen Accretion in LOcal GAlaxieS. 12, 24, 25, 29, 61, 62, 75, 78

HIPASS hi Parkes All-Sky Survey. 11, 24

HPBW half power beam width. 87, 94, 95

HSR heliocentric standard-of-rest. 111

HT head-tail. 87, 90, 91, 97, 103, 106

HVC high-velocity cloud. 25, 86–88, 90, 91, 99, 101–103, 107

ISM interstellar medium. 7, 11, 12, 29, 34, 37, 52, 101, 106

LAB Leiden/Argentine/Bonn Galactic H I Survey. 34, 35, 90, 92, 114

LGSR Local Group standard-of-rest. 112

LMC Large Magellanic Cloud. 34–37

LSR local standard of rest. 24, 90, 111, 112

MAD median absolute deviation. 49, 50, 55, 63, 66, 114

MEM Maximum Entropy Deconvolution Method. 21, 36, 48

MHD magnetohydrodynamics. 103

MIRIAD Multichannel Image Reconstruction, Image Analysis And Display. 89, 110, 118

MRC Multi-Resolution Clean. 21

MS measurement sets. 117–119

MSC Multi-Scale Clean. 21

MSP missing-spacing problem. 12, 27–29, 105

NCP north celestial projection. 36

OTF on-the-fly. 17, 24

PBC primary beam correction. 22, 25, 73, 76, 78–80, 88, 89

PE photoelectric. 99, 101

PPF position-position-frequency. 109

PPV position-position-velocity. 109

PSD power spectral density. 69–71, 81

RFI radio-frequency interference. 17, 24, 114

RMS root mean square. 23–25, 30, 36, 47, 49, 50, 55, 60–63, 66, 91, 107, 114, 115

SKA Square Kilometer Array. 30

SMC Small Magellanic Cloud. 13, 27, 34–39, 41, 43, 45–51, 105, 106

SSC short-spacing correction. 7, 12, 13, 23, 27, 29–31, 33, 34, 36, 48, 50, 52–54, 57, 60, 62, 66, 72, 73, 75, 81, 83, 103, 105–107, 117

SSP short-spacing problem. 27, 29

SW standing waves. 113, 114

THINGS The H I Nearby Galaxy Survey. 12, 13, 24, 25, 53, 54, 61, 63, 75, 78, 81, 107

UT Universal Time. 119

VLA Very Large Array. 22, 24, 54, 55, 61, 63, 75, 78, 79, 81, 83, 106, 107, 121, 122

WNM warm neutral medium. 87, 91, 97, 99–103, 107

WSRT Westerbork Synthesis Radio Telescope. 22, 24, 25, 75, 78–81, 83, 85, 87–91, 93–98, 100, 103, 106, 121

XML Extensible Markup Language. 117

XR X-ray. 99, 101

ZSC zero-spacing correction. 27

Bibliography

Alexander, P., Bregman, J. A., & Faulkner, A. J. 2009, in Wide Field Astronomy Technology for the Square Kilometre Array

Andrews, J. E., Calzetti, D., Chandar, R., et al. 2013, ApJ, 767, 51

Bajaja, E. & Loiseau, N. 1982, A&AS, 48, 71

Bajaja, E. & van Albada, G. D. 1979, A&A, 75, 251

Barentine, J. C., Wakker, B. P., York, D. G., et al. 2008, in Astronomical Society of the Pacific Conference Series, Vol. 393, New Horizons in Astronomy, ed. A. Frebel, J. R. Maund, J. Shen, & M. H. Siegel, 179

Barnes, D. G., Staveley-Smith, L., de Blok, W. J. G., et al. 2001, MNRAS, 322, 486

Battaglia, G., Fraternali, F., Oosterloo, T., & Sancisi, R. 2006, A&A, 447, 49

Ben Bekhti, N., Brüns, C., Kerp, J., & Westmeier, T. 2006, A&A, 457, 917

Bigiel, F., Leroy, A., Seibert, M., et al. 2010, ApJ, 720, L31

Blitz, L., Spergel, D. N., Teuben, P. J., Hartmann, D., & Burton, W. B. 1999, ApJ, 514, 818

Braun, R. & Burton, W. B. 2000, A&A, 354, 853

Braun, R. & Thilker, D. A. 2004, A&A, 417, 421

Braun, R. & Walterbos, R. A. M. 1985, A&A, 143, 307

Bregman, J. N. 2004, in Astrophysics and Space Science Library, Vol. 312, High Velocity Clouds, ed. H. van Woerden, B. P. Wakker, U. J. Schwarz, & K. S. de Boer, 341

Briggs, D. S. 1995, PhD thesis, The New Mexico Institute of Mining and Technology

Briggs, F. H., Sorar, E., Kraan-Korteweg, R. C., & van Driel, W. 1997, PASA, 14, 37

Brüns, C., Kerp, J., Kalberla, P. M. W., & Mebold, U. 2000, A&A, 357, 120

Brüns, C., Kerp, J., & Pagels, A. 2001, A&A, 370, L26

Brüns, C., Kerp, J., Staveley-Smith, L., et al. 2005, A&A, 432, 45

Chemin, L., Carignan, C., & Foster, T. 2009, ApJ, 705, 1395

Clark, B. G. 1980, A&A, 89, 377

Cornwell, T. J. 1983, A&A, 121, 281

Cornwell, T. J. 2008, IEEE Journal of Selected Topics in Signal Processing, 2, 793

de Blok, E., Booth, R., & Frank, B. 2009, in Panoramic Radio Astronomy: Wide-field 1-2 GHz Research on Galaxy Evolution

Diaz, J. D. & Bekki, K. 2012, ApJ, 750, 36

Dickey, J. M., McClure-Griffiths, N., Gibson, S. J., et al. 2013, PASA, 30, 3

Donho, D. L. & Johnstone, I. M. 1994, Biometrika

Draine, B. T. 2011, Physics of The Interstellar and Intergalactic Medium (Princeton Series in Astrophysics)

Duffy, A. R., Meyer, M. J., Staveley-Smith, L., et al. 2012, MNRAS, 426, 3385

Ekers, R. D. 1999, in Astronomical Society of the Pacific Conference Series, Vol. 180, Synthesis Imaging in Radio Astronomy II, ed. G. B. Taylor, C. L. Carilli, & R. A. Perley, 321

Emerson, D. 2002, in Astronomical Society of the Pacific Conference Series, Vol. 278, Single-Dish Radio Astronomy: Techniques and Applications, ed. S. Stanimirovic, D. Altschuler, P. Goldsmith, & C. Salter, 27–43

Ewen, H. I. & Purcell, E. M. 1951, Nature, 168, 356

Faridani, S., Flöer, L., Kerp, J., & Westmeier, T. 2014, A&A, 563, A99

Field, G. B., Goldsmith, D. W., & Habing, H. J. 1969, ApJ, 155, L149

Flöer, L. 2010, PhD thesis, Rheinische Friedrich-Wilhelms Universitaet Bonn

Flöer, L., Winkel, B., & Kerp, J. 2010, in RFI Mitigation Workshop

Fomalont, E. B. 1989, in Astronomical Society of the Pacific Conference Series, Vol. 6, Synthesis Imaging in Radio Astronomy, ed. R. A. Perley, F. R. Schwab, & A. H. Bridle, 213

Fomalont, E. B. 1999, in Astronomical Society of the Pacific Conference Series, Vol. 180, Synthesis Imaging in Radio Astronomy II, ed. G. B. Taylor, C. L. Carilli, & R. A. Perley, 301

Fraternali, F., Oosterloo, T., & Sancisi, R. 2004, A&A, 424, 485

Fraternali, F., van Moorsel, G., Sancisi, R., & Oosterloo, T. 2002, AJ, 123, 3124

Garrett, M. A., Cordes, J. M., Deboer, D. R., et al. 2010, ArXiv e-prints

Gentile, G., Józsa, G. I. G., Serra, P., et al. 2013, A&A, 554, A125

Gibbs, J. W. 1899, Nature, 59, 606

Giovanelli, R. & Haynes, M. P. 1988, Extragalactic neutral hydrogen, ed. K. I. Kellermann & G. L. Verschuur, 522–562

Graczyk, D., Pietrzyński, G., Thompson, I. B., et al. 2014, ApJ, 780, 59

Greisen, E. W. 1990, in Acquisition, Processing and Archiving of Astronomical Images, ed. G. Longo & G. Sedmak, 125–142

Heald, G., Józsa, G., Serra, P., et al. 2011, A&A, 526, A118

Heitsch, F. & Putman, M. E. 2009, ApJ, 698, 1485

Hermelo, I., Lisenfeld, U., Relaño, M., et al. 2012, in IAU Symposium, Vol. 284, IAU Symposium, ed. R. J. Tuffs & C. C. Popescu, 156–158

Hogbom, J. A. & Brouw, W. N. 1974, A&A, 33, 289

Holdaway, M. A. 1999, in Astronomical Society of the Pacific Conference Series, Vol. 180, Synthesis Imaging in Radio Astronomy II, ed. G. B. Taylor, C. L. Carilli, & R. A. Perley, 401

Huchtmeier, W. K. & Bohnenstengel, H.-D. 1981, A&A, 100, 72

Ianjamasimanana, R., de Blok, W. J. G., Walter, F., & Heald, G. H. 2012, AJ, 144, 96

Johnston, S., Feain, I. J., & Gupta, N. 2009, in Astronomical Society of the Pacific Conference Series, Vol. 407, The Low-Frequency Radio Universe, ed. D. J. Saikia, D. A. Green, Y. Gupta, & T. Venturi, 446

Jorsater, S. & van Moorsel, G. A. 1995, AJ, 110, 2037

Kalberla, P. M. W., Burton, W. B., Hartmann, D., et al. 2005, A&A, 440, 775

Kalberla, P. M. W. & Dedes, L. 2008, A&A, 487, 951

Kalberla, P. M. W. & Haud, U. 2006, A&A, 455, 481

Kalberla, P. M. W. & Kerp, J. 2009, ARA&A, 47, 27

Kalberla, P. M. W., McClure-Griffiths, N. M., Pisano, D. J., et al. 2010, A&A, 521, A17

Kalberla, P. M. W., Mebold, U., & Reich, W. 1980, A&A, 82, 275

Kerp, J., Winkel, B., Ben Bekhti, N., Flöer, L., & Kalberla, P. M. W. 2011, Astronomische Nachrichten, 332, 637

Kerr, F. J. & Hindman, J. V. 1953, AJ, 58, 218

Konz, C., Brüns, C., & Birk, G. T. 2002, A&A, 391, 713

Kulkarni, S. R. & Mathieu, R. 1986, Ap&SS, 118, 531

Kurono, Y., Morita, K.-I., & Kamazaki, T. 2009, PASJ, 61, 873

Lequeux, J. 2005, The Interstellar Medium (Springer)

Mangum, J. G., Emerson, D. T., & Greisen, E. W. 2007, A&A, 474, 679

McClure-Griffiths, N. M., Pisano, D. J., Calabretta, M. R., et al. 2009, ApJS, 181, 398

McIntyre, V. J. 1998, PASA, 15, 157

McMullin, J. P., Waters, B., Schiebel, D., Young, W., & Golap, K. 2007, in Astronomical Society of the Pacific Conference Series, Vol. 376, Astronomical Data Analysis Software and Systems XVI, ed. R. A. Shaw, F. Hill, & D. J. Bell, 127

Muller, C. A. & Oort, J. H. 1951, Nature, 168, 357

Muller, C. A., Oort, J. H., & Raimond, E. 1963, Academie des Sciences Paris Comptes Rendus, 257, 1661

Narayan, R. & Nityananda, R. 1986, ARA&A, 24, 127

Nidever, D. L., Majewski, S. R., & Burton, W. B. 2008, 679, 432

Oosterloo, T., Fraternali, F., & Sancisi, R. 2007, AJ, 134, 1019

Oosterloo, T., Verheijen, M., & van Cappellen, W. 2010, in ISKAF2010 Science Meeting

Oosterloo, T., Verheijen, M. A. W., van Cappellen, W., et al. 2009, in Wide Field Astronomy Technology for the Square Kilometre Array

Ott, J. & Kern, J. 2014, CASA User Reference & Cookbook, The National Radio Astronomy Observatory

Patterson, M., Walterbos, R., Heald, G., et al. 2012, in American Astronomical Society Meeting Abstracts, Vol. 219, American Astronomical Society Meeting Abstracts #219

Perley, R. A. 1999, in Astronomical Society of the Pacific Conference Series, Vol. 180, Synthesis Imaging in Radio Astronomy II, ed. G. B. Taylor, C. L. Carilli, & R. A. Perley, 275

Pisano, D. J., Barnes, D. G., Gibson, B. K., et al. 2004, ApJ, 610, L17

Pisano, D. J., Barnes, D. G., Gibson, B. K., et al. 2007, ApJ, 662, 959

Planck Collaboration, Abergel, A., Ade, P. A. R., et al. 2013, ArXiv e-prints

Plöckinger, S. & Hensler, G. 2012, A&A, 547, A43

Popping, A. & Braun, R. 2008, A&A, 479, 903

Putman, M. E., Peek, J. E. G., & Joung, M. R. 2012, ARA&A, 50, 491

Putman, M. E., Saul, D. R., & Mets, E. 2011, MNRAS, 418, 1575

Putman, M. E., Staveley-Smith, L., Freeman, K. C., Gibson, B. K., & Barnes, D. G. 2003, ApJ, 586, 170

Quilis, V. & Moore, B. 2001, ApJ, 555, L95

Rich, J. W., de Blok, W. J. G., Cornwell, T. J., et al. 2008, AJ, 136, 2897

Rohlfs, K. & Wilson, T. L. 2004, Tools of Radio Astronomy, Vol. Fourth revised and enlarged edition (springer)

Santillán, A., Franco, J., Martos, M., & Kim, J. 1999, ApJ, 515, 657

Sault, R. J., Staveley-Smith, L., & Brouw, W. N. 1996, A&AS, 120, 375

Sault, R. J., Teuben, P. J., & Wright, M. C. H. 1995, in Astronomical Society of the Pacific Conference Series, Vol. 77, Astronomical Data Analysis Software and Systems IV, ed. R. A. Shaw, H. E. Payne, & J. J. E. Hayes, 433

Schmidt, P., Józsa, G. I. G., Gentile, G., et al. 2014, A&A, 561, A28

Schwarz, U. J. & Wakker, B. P. 1991, in Astronomical Society of the Pacific Conference Series, Vol. 19, IAU Colloq. 131: Radio Interferometry. Theory, Techniques, and Applications, ed. T. J. Cornwell & R. A. Perley, 188–191

Shannon, C. E. & Weaver, W. 1949, The mathematical theory of communication

Silva-Villa, E. & Larsen, S. S. 2012, A&A, 537, A145

Sollima, A., Gratton, R. G., Carretta, E., Bragaglia, A., & Lucatello, S. 2013, MNRAS, 433, 1276

Stanimirović, S. 1999, PhD thesis, University of Western Sydney Nepean

Stanimirović, S. 2002, in Astronomical Society of the Pacific Conference Series, Vol. 278, Single-Dish Radio Astronomy: Techniques and Applications, ed. S. Stanimirovic, D. Altschuler, P. Goldsmith, & C. Salter, 375–396

Stanimirović, S., Staveley-Smith, L., Dickey, J. M., Sault, R. J., & Snowden, S. L. 1999, MNRAS, 302, 417

Staveley-Smith, L., Sault, R. J., Hatzidimitriou, D., Kesteven, M. J., & McConnell, D. 1997, MNRAS, 289, 225

Stewart, I. M., Fenech, D. M., & Muxlow, T. W. B. 2011, A&A, 535, A81

Sutter, P. M., Wandelt, B. D., McEwen, J. D., et al. 2013, arXiv:1309.1469v2

Teuben, P. 2012

Thilker, D. A., Braun, R., Walterbos, R. A. M., et al. 2004, ApJ, 601, L39

Thom, C., Peek, J. E. G., Putman, M. E., et al. 2008, ApJ, 684, 364

Thompson, A. R. 1999, in Astronomical Society of the Pacific Conference Series, Vol. 180, Synthesis Imaging in Radio Astronomy II, ed. G. B. Taylor, C. L. Carilli, & R. A. Perley, 11

van Woerden, H. & Strom, R. G. 2006, Journal of Astronomical History and Heritage, 9, 3

van Woerden, H. & Wakker, B. P. 2004, in Astrophysics and Space Science Library, Vol. 312, High Velocity Clouds, ed. H. van Woerden, B. P. Wakker, U. J. Schwarz, & K. S. de Boer, 195

van Woerden, H., Wakker, B. P., Peletier, R. F., & Schwarz, U. J. 2000, in Astronomical Society of the Pacific Conference Series, Vol. 218, Mapping the Hidden Universe: The Universe behind the Mily Way - The Universe in HI, ed. R. C. Kraan-Korteweg, P. A. Henning, & H. Andernach, 407

van Woerden, H., Wakker, B. P., Schwarz, U. J., & de Boer, K. S. 2004, The High-Velocity Clouds (Kluwer Academic Publishers)

Venzmer, M. S., Kerp, J., & Kalberla, P. M. W. 2012, A&A, 547, A12

Verschuur, G. L. & Kellermann, K. . I. 1988, Galactic and Extragalactic Radio Astronomy, 2nd edn., ed. E. Bouton (Springer-Verlag)

Vogel, S. N., Wright, M. C. H., Plambeck, R. L., & Welch, W. J. 1984, ApJ, 283, 655

Wakker, B. P. 2004, in Astrophysics and Space Science Library, Vol. 312, High Velocity Clouds, ed. H. van Woerden, B. P. Wakker, U. J. Schwarz, & K. S. de Boer, 25

Wakker, B. P. & Boulanger, F. 1986, A&A, 170, 84

Wakker, B. P. & Schwarz, U. J. 1988, A&A, 200, 312

Wakker, B. P. & van Woerden, H. 1997, ARA&A, 35, 217

Walter, F., Brinks, E., de Blok, W. J. G., et al. 2008, AJ, 136, 2563

Weiß, A., Neininger, N., Hüttemeister, S., & Klein, U. 2001, A&A, 365, 571

Westmeier, T. 2007, PhD thesis, Universität Bonn

Westmeier, T. 2014, Homepage of Tobias Westmeier

Westmeier, T., Brüns, C., & Kerp, J. 2005a, in Astronomical Society of the Pacific Conference Series, Vol. 331, Extra-Planar Gas, ed. R. Braun, 105

Westmeier, T., Brüns, C., & Kerp, J. 2005b, A&A, 432, 937

Westmeier, T., Koribalski, B. S., & Braun, R. 2013, MNRAS, 434, 3511

Whiting, M. & Humphreys, B. 2012, PASA, 29, 371

Winkel, B., Ben Bekhti, N., Darmstädter, V., et al. 2011, A&A, 533, A105

Winkel, B., Flöer, L., & Kraus, A. 2012a, A&A, 547, A119

Winkel, B., Kalberla, P. M. W., Kerp, J., & Flöer, L. 2010, ApJS, 188, 488

Winkel, B., Kraus, A., & Bach, U. 2012b, A&A, 540, A140

Wolfire, M. G., Hollenbach, D., McKee, C. F., Tielens, A. G. G. M., & Bakes, E. L. O. 1995a, ApJ, 443, 152

Wolfire, M. G., McKee, C. F., Hollenbach, D., & Tielens, A. G. G. M. 1995b, ApJ, 453, 673

Wolfire, M. G., McKee, C. F., Hollenbach, D., & Tielens, A. G. G. M. 2003, ApJ, 587, 278

Wootten, A. & Thompson, A. R. 2009, IEEE Proceedings, 97, 1463

Ye, T., Turtle, A. J., & Kennicutt, Jr., R. C. 1991, MNRAS, 249, 722

List of Figures

List of Tables

Acknowledgements

passion for education affected my life significantly and helped me excel at my studies. I am blessed with their life-long support in any aspect of my life. Therefore, I am always indebted to them.

The last but not the least, I would like to offer my deepest and most heartfelt thanks to my girl friend, Sarah Ghasemi, for her love and kindness. Her understanding and encouragement has been a great support during my thesis.